Title
Application of two dimensional and high surface area materials in energy conversion and storage devices

Author
Ergen, Onur

Publication Date
2017

Peer reviewed|Thesis/dissertation

Application of two dimensional and high surface area materials in energy conversion and storage devices

By

Onur Ergen

A dissertation submitted in partial satisfaction of the

requirements for the degree of

Doctor of Philosophy

in

Physics

in the

Graduate Division

of the

University of California, Berkeley

Committee in Charge:

Professor Alex Zettl, Chair
Professor Feng Wang
Professor Lydia Sohn

Summer 2017

Application of two dimensional and high surface area materials in energy conversion and storage devices

by

Onur Ergen

Abstract

Application of two dimensional and high surface area materials in energy conversion and storage devices

By

Onur Ergen

Doctor of Philosophy in Physics

University of California at Berkeley

Professor. Alex Zettl, Chair

The work presented in this thesis aims to emphasize the power of two dimensional (2D) and high surface area material integration into energy harvesting and storage devices by introducing new techniques and devices. The techniques and device architectures are unique and encourage new ways of thinking in experimental condensed matter physics, material growth, and synthesis, while providing new perspectives to science and engineering.

This thesis consists of three parts: Part I introduces two dimensional and high surface area materials. Part II focuses on energy harvesting devices and the demonstration of different solar cell architectures with integration of graphene, hexagonal boron nitride (h-BN), and graphene aerogel (GA). In Part III, various energy storage device architectures are introduced for lithium ion batteries (LIBs) and lithium air batteries (Li-air) by incorporating different high surface area materials: boron nitride aerogels (BNAG), boron nitride nanotubes (BNNTs), or graphene aerogels (GA). Additional measurements, supplementary figures, and detailed fabrication methods are discussed in the appendix.

Sevgili Aileme

Table of Contents

List of Figures

List of Tables

Acknowledgements

I wish to first thank Professor Alex Zettl, who has been an exceptional advisor. He was not only an advisor but an invaluable mentor, excellent teacher, strong supporter and a highly knowledgeable guide. I am very thankful to him for giving me the opportunity to work in his lab, to benefit from his wisdom, profound knowledge, and guidance throughout my graduate studies. I am also very grateful and indebted to him for his great patience with me. None of this work would have been possible without his counsel, inspiration, and persistence. He encouraged me to explore my own ideas and pushed me when necessary. I also appreciated the excellent facilities and research environment he built.

Secondly, I wish to thank Professors Feng Wang and Lydia Sohn for their assistance and willingness to be part of my thesis committee. I also want to express my gratitude to Professor Jeff Neaton for his involvement in my qualifying exam committee.

I am grateful to my colleagues for their outstanding friendship, encouragement, and moments of laughter. A sincere thanks to all who have helped me and spent time with me talking about a plethora of scientific pursuits.

I also would like to thank Anne Takizawa who has done such an amazing job running the Student Service Office. I am truly grateful for her patience and ingenuity while helping me to overcome many unusual academic obstacles. She provided fabulous support and encouragement throughout every obstacle I encountered.

Finally, I owe a tremendous debt to my family: my parents, my brothers, and my wife, who love and support me unconditionally and always believe in me.

“This is my quest, it is not what I wanted but it is who I was, but not the day after.”

“Kendime bir adim daha! Kıracağım, yıkacağım tüm duvarlara!”

PART I

Chapter 1

Introduction

Incorporating science in engineering is becoming more and more crucial every day. We have all the necessary scientific tools but are limited by insufficient technological progress and breakthroughs. We need new avenues, creative thinking, and interdisciplinary engagement to expand beyond. With that said, it is an art to utilize multidisciplinary knowledge and craft cutting-edge, high-impact innovations. Two-dimensional (2D) and high surface area (HSA) materials display a wide range of unique electrical, chemical, mechanical, and optical properties. Their multifunctional properties make them a game changer and create new avenues in science and technology. The creative application of these materials is vitally important to achieve major breakthroughs and initiate new avenues in scientific research and technology. Their proper utilization can significantly improve current device architectures, provide a platform to investigate fundamental physical phenomena, and help to explore unique and unconventional scientific designs while promising solutions to the most relevant technological challenges.
In this thesis, I discuss my work on the integration of two dimensional and high surface area materials in energy devices. I introduce several important device architectures, focusing mainly on solar cells and batteries. I use various nano-material combinations to construct these devices, primarily using graphene and hexagonal boron nitride (h-BN) as 2D materials and graphene aerogel, boron nitride nanotubes (BNNTs,) and boron nitride aerogels (BNAG) as highsurface area materials. I briefly explain electrical, mechanical, and optical properties of these nano-materials in Chapter 2

In Chapter 3, I focus on novel photovoltaics projects, first introducing perovskite based solar cells and explaining how organic-inorganic halide perovskite materials inspired the photovoltaic devices. Next, I introduce a solar cell design called “Graded band gap perovskite solar cells,” briefly covering the basics of graded band gap solar cells. Lastly, I cover an independent solar cell design based on metal insulator semiconductor architecture.

Chapter 4 is devoted to energy storage devices. I introduce two different battery architectures, lithium ion batteries (LIBs) and lithium air batteries (Li-air). All of these device architectures are mainly constructed by incorporating different high surface area materials, such as boron nitride aerogels(BNAG), boron nitride nanotubes(BNNTs), or graphene aerogels (GA).

Appendix-A, Appendix-B, and Appendix-C are designated to give the reader more detailed descriptions, tips, and tricks about the proposed projects.

Chapter 2

In this chapter, I briefly introduce the fundamental properties of 2D and high surface area (HSA) materials. First, focusing on graphene, then hexagonal boron nitride (h-BN), and lastly the high surface area materials: graphene aerogels, boron nitride nanotubes, and boron nitride aerogels. This chapter serves as a practical introduction to how these nanomaterials inspired the new device designs that are discussed in Chapters 3 and 4.

2.1 Two dimensional (2D) layered Materials:

Two dimensional materials are a class of nano-materials with a thickness typically from one to several atoms. In these materials, there can be unique electronic screening and a band gap structure that may be dramatically different than in bulk, 3D materials. Moreover, the electrons are restricted to a two-dimensional movement in the x-y plane [2-8].

The study of 2D materials has a long history. Various epitaxial semiconductor growth methods were tried at first, such as GaAs sandwiched between $Al_xGa_{1-x}As$ [9, 10]. However, epitaxial growth is a technically challenging and very expensive process. It also has distinctive growth requirements to manage lattice mismatch and thermal expansion coefficients between deposited layers. For this reason, researchers constantly searched for different materials with 2D properties, until the year 2004, when graphene, a one atomic layer thick carbon material, was obtained from exfoliating the pyrolytic-graphite by the Scotch-tape method [11-14].

From that moment, graphene attracted extensive attention through applied research and theory [15-19]. Its unique optical, electrical, and mechanical properties inspired researchers to investigate different 2D layered materials. Hexagonal boron nitride (h-BN) is one of the other appealing 2D materials that researchers discovered and it recently garnered attention due to its insulating properties, temperature stability, and mechanical strength similar to graphene [20-22]. Even though many more 2D layer materials such as transition metal chalcogenides (TDMs), transition metal dichalcogenides (TDCMs), and transition metal oxides (TMO) were discovered, this thesis centers mainly on the use of graphene and h-BN. Their properties are described at length in the following chapters.

2.1.1 Electronic and Optical Properties of Graphene

Graphene, a new class of two-dimensional, zero-gap semiconductors, is only one atom thick. Its unique structure and novel physical properties permit a wide range of application in electronics, optics, and other areas [11, 13-19, 23, 24]. Graphene has a hexagonal-honeycomb lattice structure with sp^2 hybridization of carbon atoms (Fig 2.1a). It also has a carbon-carbon bond length of 1.42Å, which connects two primitive cell atoms, A and B, in the unit cell. The electrons obey Dirac-like dynamics, behaving like massless Dirac Fermions due to their gapless linear energy spectrum at two Dirac points, K and K', at the Brillouin zone (Fig. 2.1c) [12, 23, 25, 26].

This dispersion relation, calculated by the tight binding model, leads to several phenomena from an anomalous quantum Hall effect to the absence of localization, etc. Moreover, the electrons can display near ballistic transport with very high mobility [12, 15, 23, 25-27].

The mobility for suspended graphene can exceed 200.000cm^2/Vs and 15.000cm^2/Vs on a substrate [12, 23, 28-30]. In addition to these superior electronic properties, graphene has broadband high transparency and superior mechanical strength [12, 26, 29, 31]. A monolayer of graphene absorbs approximately 2% of visible light and has a tensile strength of 130GPa with 1TPa Young's modulus [31, 32].

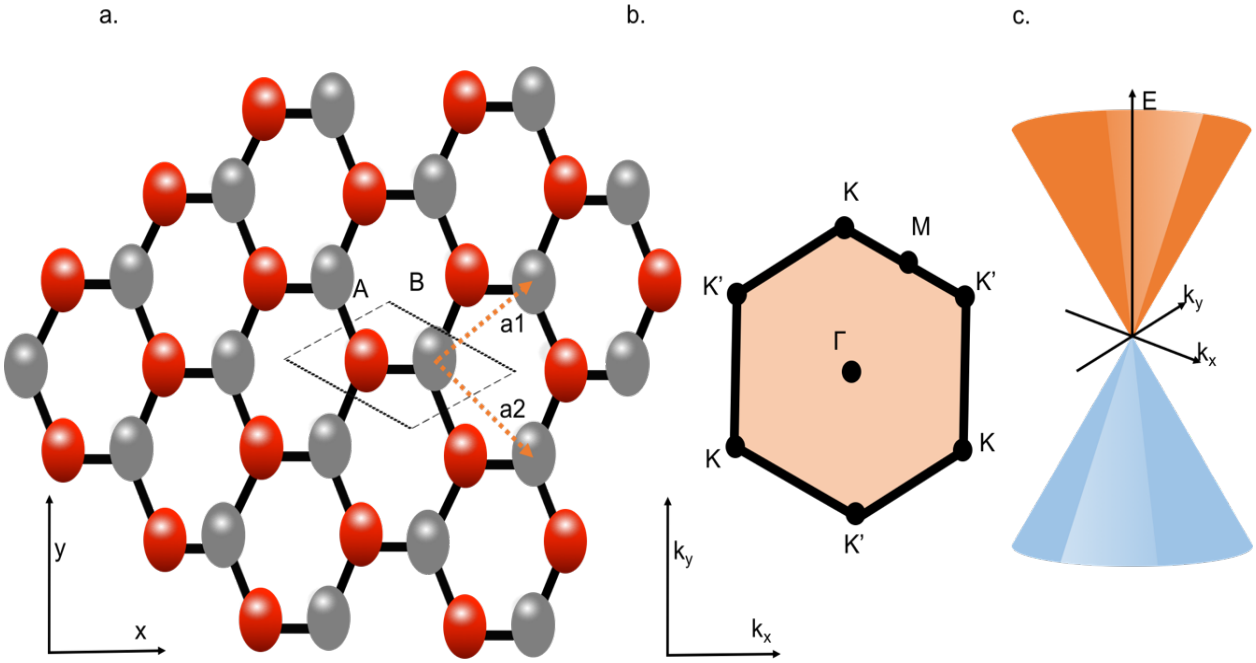

Figure 2.1 a. Scheme of the honeycomb lattice structure of graphene. In this honeycomb lattice structure, individual carbon atoms are held together with strong covalent bonds and all of the carbon atoms are sp^2 hybridized with the nearest neighbor spacing a_0=1.42Å. The primitive unit cell of graphene, shown as the square box, and two unit vectors, a_1 and a_2, are shown with two non-equivalent carbon atoms A and B. All other atoms can be translated back to A and B by using suitable combinations of these unit vectors, $a_1 = a_0(3/2, \sqrt{3}/2)$ and $a_2 = a_0(3/2, -\sqrt{3}/2)$. b. First Brillion zone of reciprocal lattice of graphene rotated 30^0 with respect to the real space. Four high symmetry points K, K', M, Γ are distinctively marked c. Electronic dispersion spectrum of graphene. The cone-shaped energy bands present no band gap [33].

Moreover, these optical and electronic properties of graphene can be tuned with doping level, gating, or chemical potential. Graphene can be easily doped with nitrogen, boron and other elements. For example, nitrogen doped graphene provides much higher electro-catalytic activity towards oxygen reduction, boron doped graphene shows better adsorption of Lithium ions, and electrical gating of graphene provides an extra degree of freedom to carrier concentration [34-39].

2.1.2 Electronic and Optical Properties of Hexagonal Boron Nitride

Hexagonal boron nitride (h-BN) is another sp^2 bonded 2D material and is recently gaining significant attention due to its contrasting electronic properties to graphene. Although h-BN has a similar honeycomb lattice structure to graphene, it is a typical insulator with a band gap of ~5.97eV (Fig. 2.2). Its crystal is composed of an equal number of boron (B) and nitrogen (N) atoms with a B-N bond length of 1.44 Å. h-BN has higher oxidation resistance as well as thermal and chemical stability compared to graphene, even in reactive environments[40-43]. For this reason, h-BN presents significant advantages in chemical reactions, especially with corrosion passivation coating[44]. h-BN also has an atomically flat nature without any interface trap states or dangling bonds, which makes it an ideal substrate for graphene and electronic gating. A monolayer h-BN is highly transparent, like graphene, and can transmit over 99% of the visible spectrum.

h-BN can be exfoliated with scotch tape or synthesized using the CVD method, both similar to graphene. In addition, the graphene lattice can be converted to boron nitride in nanometer scale with a high degree of chemical purity by using a carbothermal reduction method [45].

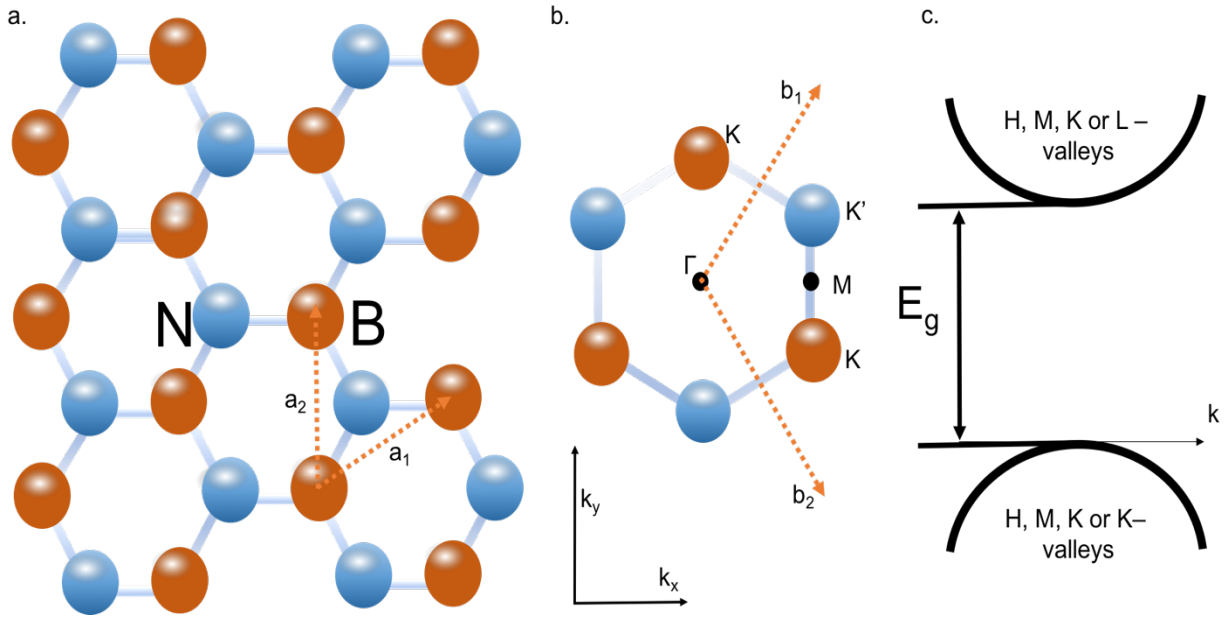

Figure 2.2 a. Scheme of the honeycomb lattice structure of h-BN. This honeycomb lattice structure is constructed with alternating boron and nitrogen atoms. Boron and nitrogen atoms form ionic bonds and produce similar sp2-bonded structures to graphene. The lattice unit vectors, a1=a(√3/2,1/2, 0) and a2= a(0,1,0), where a= 2.5Å is the lattice constant. b. First Brillion zone of reciprocal lattice of h-BN. The reciprocal lattice vectors, b1 and b2, are shown in the Brillouin zone. c. Electronic dispersion spectrum of h-BN. The wide band gap value estimated ~5.97 eV.

2.2 High surface area materials

High surface area materials can be attributed to either the particle where the surface to volume ratio is very high, such as in nano-particles, nanowires, and their derived clusters, or materials with a very high void fraction and high porosity. Porous, high-surface area materials are the main focus of this thesis. These porous materials are highly desired materials for many important applications including energy storage, sensing, hydrogen or methane storage, and water desalination, among other purposes. A number of promising porous materials have been introduced in the scientific literature, such as metal-organic frame works, zeolites, metallic foams, etc. Among all these porous materials, the aerogels are considered to be one of the most promising material systems.

Aerogel is a general term for diverse mesoporous solid materials with a porosity of more than 50%. An aerogel is comprised of a network structure constructed by interconnected nanoparticles. This network structure creates an extremely low density structure, ranging from 1.1 10^{-3} to 0.5g/cm3, with a high internal void volume. Some of the more widely known aerogel types in the industry are carbon based. Carbon based aerogels (CBA) are electrically conductive and have good mechanical stability. Moreover, the conductivity and mechanical strength can be controlled by adjusting porosity concentration and density [46-48]. Because of these properties, CBA finds many applications in industry and in research. Their applications range from energy storage and conversion to catalyst support and sensors [49-52]. Graphene based aerogel, graphene aerogel (GA), is the most attractive carbon-based system because of graphene's superior physical and electrical properties, containing a large surface area, mechanical strength, tunable high chemical stability, etc. In addition to these properties, GA can be synthesized by cost-effective methods compared to other carbon-based analogues and can be easily functionalized or activated by chemical attachments to fit the desired applications.

Apart from carbon based aerogels, boron nitride based aerogels are very promising and versatile. Boron nitride is a ceramic, non-oxide material with very low density, high melting point, and outstanding chemical resistance. Thus, honeycomb hexagonal boron nitride (h-BN) based nanomaterials can have properties far superior to their carbon counterparts, such as higher oxidation resistance and outstanding high temperature stability, with no compromise in mechanical strength [21, 22]. These unique properties and insulating behaviors make h-BN based aerogels attractive for a variety of technological applications and some applications are complimentary to graphene aerogels. In the next two sections, I will briefly introduce the electronic and mechanical properties of graphene and boron nitride aerogels.

2.2.1Electronic and Mechanical Properties of Graphene Aerogels

Graphene received tremendous attention for its potential to develop valuable derivatives, especially three-dimensional (3D) aerogel structures. There are several methods to interconnect graphene to produce a 3D solid network, such as hydrothermal, chemical reduction, sol-gel polymerization, template guided growth method, etc. [48, 53-62]. Choosing the synthesis method is pertinent to GA's electronic and mechanical properties. The conductivity can be significantly improved up to 1x10^{2} S/m, by sol–gel polymerization of resorcinol (R) and formaldehyde (F)

with sodium carbonate as a catalyst (C) in an aqueous suspension of graphene oxide (GO) [63]. This conductivity value is significantly higher than that of other GA synthesizing methods and even higher than any other carbon-based aerogel. Additionally, the conductivity can be further improved using various kinds of reduction agents and a post annealing process [61].

The mechanical properties of GA are also directly dependent on the fabrication method. Some of these methods result in brittle GA structures. In order to increase the mechanical strength of graphene aerogels, various polymer reinforcements are developed. For example, graphene aerogels reenforced with polystyrene exhibit a large compressive strain of 80% and a high compressive stress of 80kPa, while GA without polymer binders exhibits much lower mechanical performances [61].

Moreover, GA can support more than 14000 times its own weight, which is approximately twice as much as other carbon aerogel counterparts [64]. In general, the measured Young's modulus and strength of GA can go up to about 20MPa and 2.2MPa, respectively [56, 64-67].

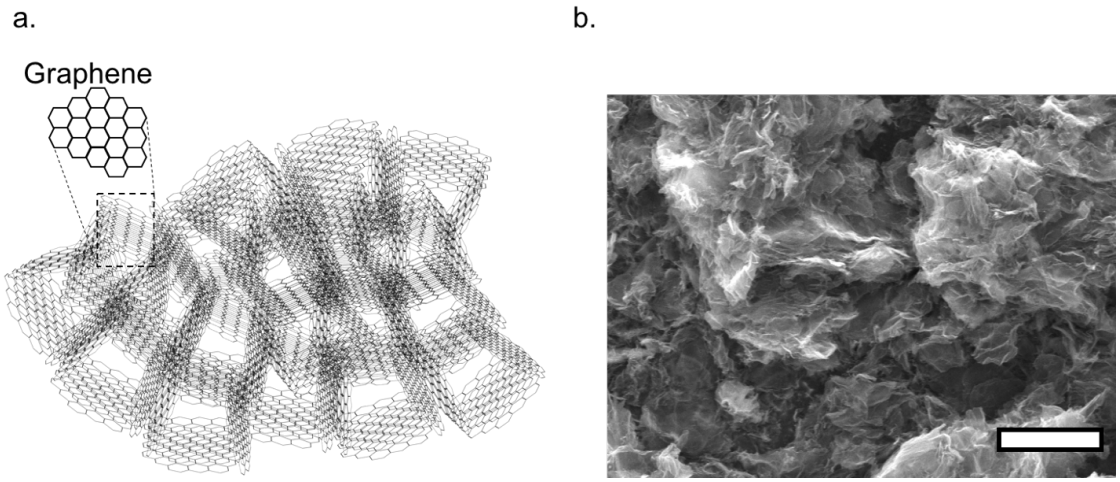

Figure 2.3 a. Schematic illustration of graphene aerogel, constructed by self-assembly of graphene b. SEM image of graphene aerogel. Scale bar:1μm.

2.2.2 Electronic and Mechanical Properties of Boron Nitride Aerogels

Boron nitride aerogels exhibit similar characteristics to graphene aerogels. Boron nitride contains boron and nitrogen bonds instead of carbon-carbon (C-C). While boron belongs to Group IIIA on the Periodic Table, it is a non-metal element and shares many of its properties with carbon, having one less electron and lower electronegativity. On the other hand, nitrogen belongs to Group V and contains one more electron than a carbon atom, thus exhibiting higher electronegativity. The difference in electronegativity of boron and nitrogen significantly alters both the molecular and solid-state electronics properties of h-BN when compared to its C-C counterparts. The BN displays optically transparent insulating behavior with a wide band gap of around 5.97eV. Boron and Nitrogen form ionic bonds and produce a similar sp^2-bonded structure to graphene. This ionic bonded BN is also complementary and isoelectronic to all carbon

analogues. The dipolar field between boron and nitrogen atoms also provides superior physisorption properties, low dielectric constant, and high temperature oxidation resistance [45, 68, 69].

BN-based 3D porous materials, boron nitride aerogels (BNAG), also provide ultra-low densities, high surface area and comparable mechanical strength to graphene aerogels. Even though BNAG is a very promising material system, it does not get its deserved attention, due to its challenging synthesis methods. BN synthesis methods usually require complex procedures with very high temperatures and toxic precursors. Fortunately, it was recently shown that carbon based materials can be directly converted to boron nitride by carbothermal reduction, using non-toxic reactants [45, 70, 71]. Thus BNAG can be synthesized from graphene aerogels by using this reduction method [45]. GA and boron oxide are placed in an induction furnace and forced to react with each other at sufficiently high temperatures in a nitrogen environment to form sp^2 bonded BN networks. With this conversion process, GA can completely convert to BNAG by maintaining nano-scale morphology. Moreover, GA can also be partially converted to BNAG to produce efficient BN/graphene heterostructures.

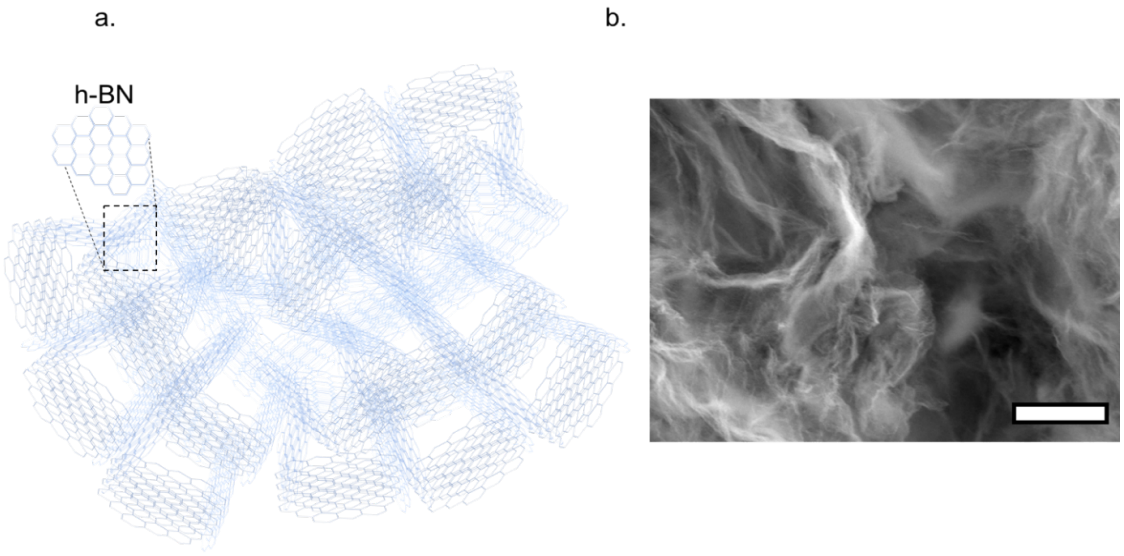

Figure 2.4 a. Schematic illustration of boron nitride aerogel, constructed by self-assembly of h-BN b. SEM image of graphene aerogel. Scale bar :1μm

PART II

Chapter 3

Energy Harvesting Devices

In recent years, growing demand for environmentally sustainable and economical energy sources has become a crucial challenge for researchers to address [72-75]. Means of harnessing solar energy has developed especially rapidly and the cost of solar electricity is beginning to reach grid tariff parity —equaling that of traditional retail power— due to advancements in silicon photovoltaics technology. With these advancements, the price of silicon photovoltaic modules has fallen drastically. However, the balance of system (BOS) cost, which is approximately sixty percent of the overall cost, including the cost of installation, mounting materials, shipping, licensing, and inverters, etc., continues to prove expensive. Today, developing very-high efficiency solar cell modules has become the main focus of photovoltaic research so that the BOS cost can be reduced. High efficiency modules can generate the same power with fewer panels, directly affecting roof space, mounting materials, installation times, etc., substantially lowering BOS costs [76, 77]. The fabrication process required to produce a high efficiency silicon solar cell, above 20%, is currently expensive and quite complicated, thus limiting progress in commercializing the technology. For this reason, developing a light weight novel solar cell system that can provide very high efficiency at a low cost remains a significant goal.

In the following chapters, several important solar cell architectures will be introduced. First, I will focus on perovskite based photovoltaics and how we developed a way around this intransigent BOS tradeoff between efficiency and cost. Then, I will highlight other photovoltaic materials and techniques we also developed to produce a novel and low cost solar cell system. These architectures emphasize the critical importance of utilizing two-dimensional (2D) layer and high surface area materials in energy conversion devices. The development of these systems is a clear and strong example of combining physics, chemistry, and engineering in an innovative way.

3.1 Perovskite based Photovoltaics

Organic-inorganic perovskite material is a promising key player in the development of low cost, high performance solar cells. In recent years, its rapid improvement in the power conversion efficiencies (Fig. 3.1) has fueled excitement for future solar cell exploration.

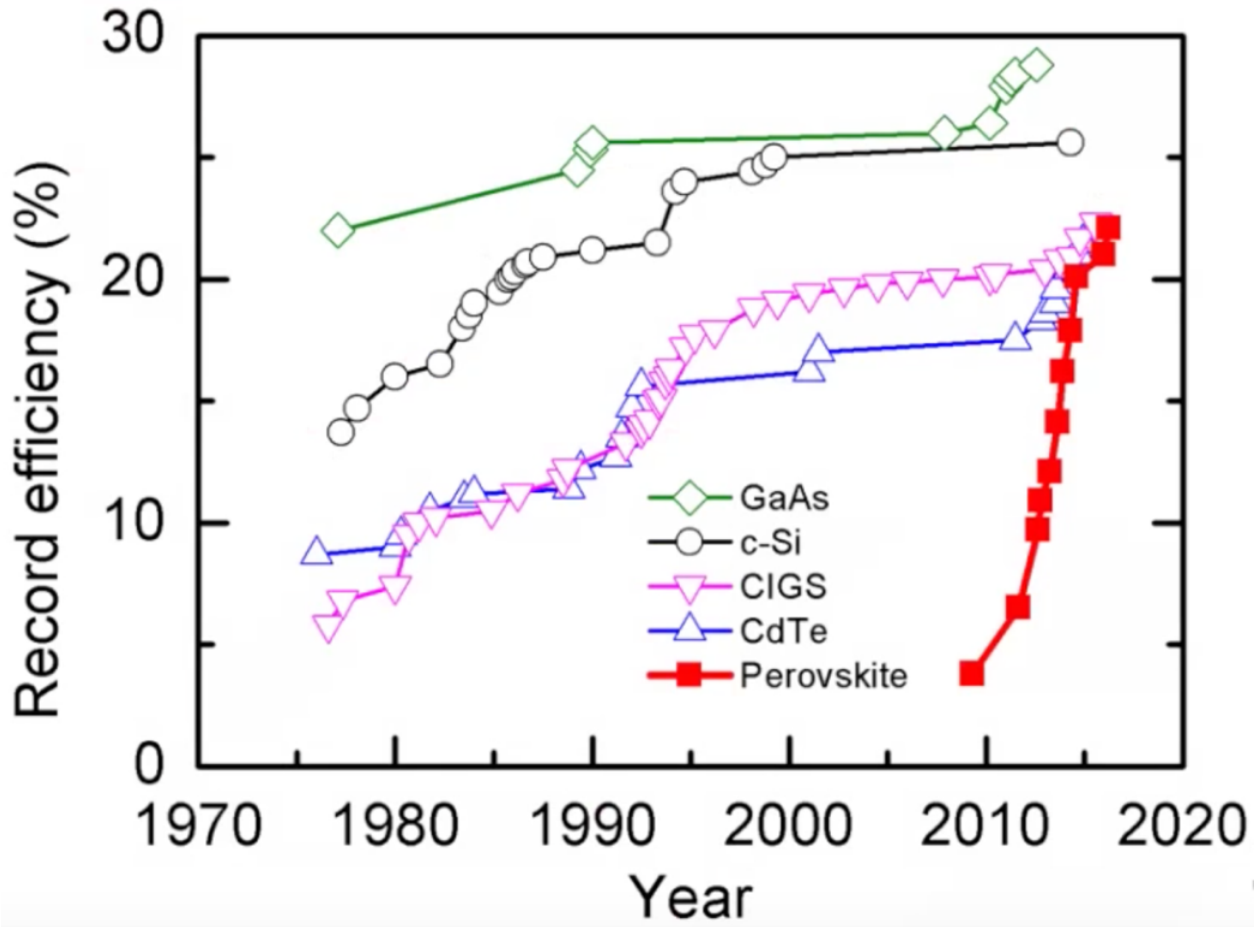

Figure 3.1 Power Conversion Efficiency evaluation of different photovoltaic technologies [1]. Perovskite solar cells have an unprecedented rate of progress compared to any other photovoltaic technology.

The term “perovskite” is a family name for a group of materials with a general formula of ABX_3 (Fig. 3.2). In this chemical formula, A is an organic cation, B is an inorganic big cation and X is a smaller halogen anion. Although perovskites have been a well-known material for several decades, they remained largely overlooked for solar energy applications until 2009. *Kojima, et al* reported the first perovskite based device and studied photovoltaic function of the organic inorganic lead halide perovskite ($CH_3NH_3PbBr_3$ and $CH_3NH_3PbI_3$). However, perovskite based photovoltaics attracted tremendous attention after a breakthrough paper by *M.M. Lee, et al* appeared in 2012. The power conversion efficiency (PCE) values have significantly increased since 2012, current reaching over 22% (Fig. 3.1). The success of perovskite solar cells on PCE is remarkable because they reached a level during the last five years that silicon took more than three decades to reach.

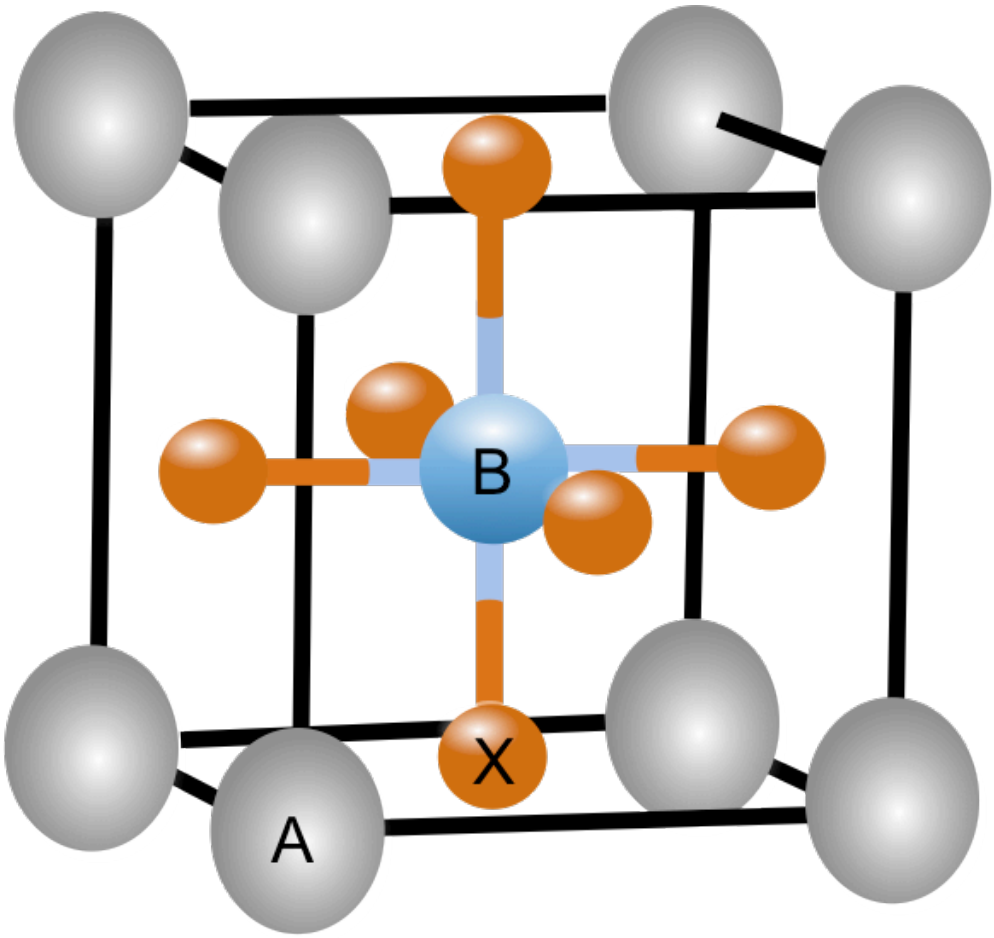

Figure 3.2 The three-dimensional crystal structure of perovskite materials.

Furthermore, most of the organic-inorganic hybrid perovskites are solution-processable which enables a highly scalable, low cost solar energy conversion. The most compelling characteristics of perovskite are its tunable electronic and optical properties with very long carrier diffusion length [78-81].

Organic-inorganic perovskite solar cells are typically prepared in a single band gap configuration, where an absorber layer (ABX_3, $A=CH_3NH_3(MA)$;B=Pb ,Sn; and X=Cl, Br, I) is sandwiched between an electron injection layer (ETL) and a hole transport layer (HTL) (Fig. 3.3)[82-86].

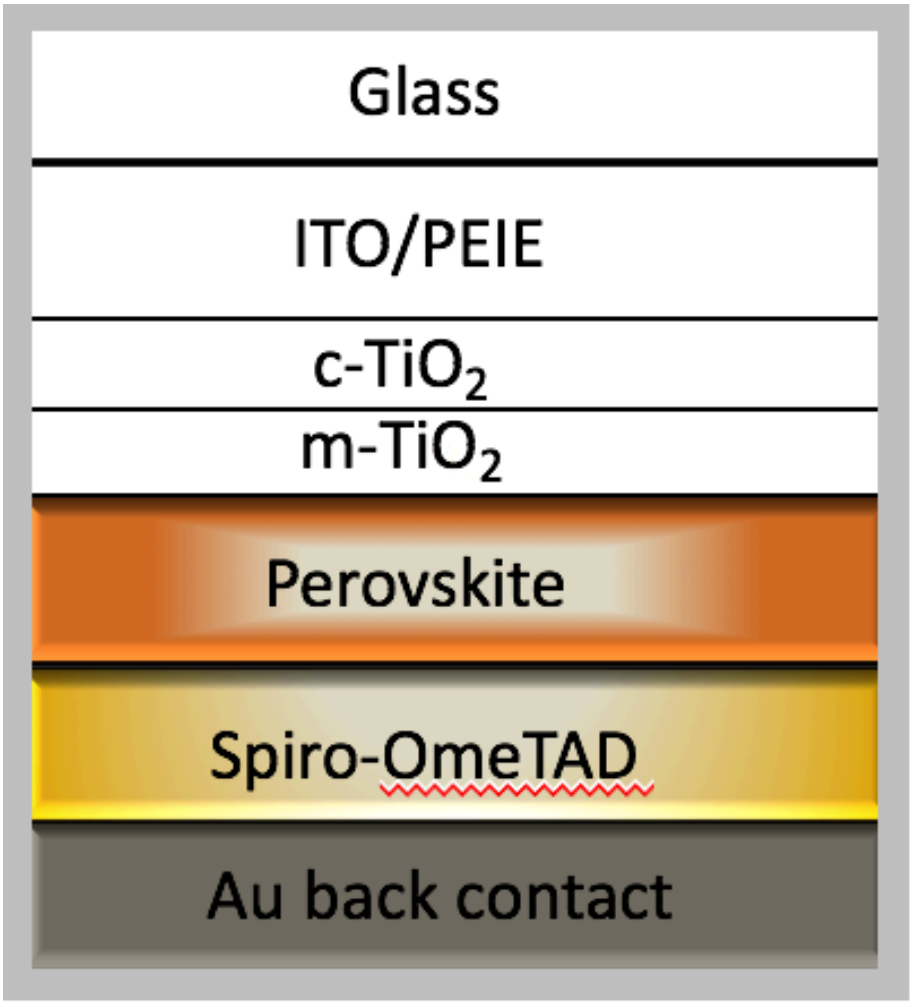

Figure 3.3 The generic structure of a typical perovskite solar cell.

Following significant efforts to optimize interface layers and to control the carrier dynamics, power conversion efficiencies (PCE) for this design, for a single cell, have surpassed 20% [83-87]. Additionally, due to the toxicity of lead in the absorber layer, lead free tin halide perovskite solar cells have gained tremendous importance. However, due to their chemical instability[86], lead free cells do not display such high photovoltaic performances (less than 7%). The tunable band gap of methylammonium-lead-halide has also led researchers to construct multi-junction tandem cells, which aims to maximize the solar irradiative spectrum [88-93]. In these tandem cells, the perovskite layer can be integrated with crystalline silicon (c-Si) and copper indium gallium selenide (CIGS). However, the tandem cell requires complex electrical coupling and interconnection between the perovskite sub-cells, which generates electron-hole recombination centers. Despite numerous proposals for band gap engineering of perovskite layers by replacing the metal cations, varying the composition of halide ions, or altering the moisture content, only one report has emerged of a successful perovskite/perovskite two terminal tandem cell[92], with a PCE of 7-10%. An appealing alternative is the perovskite-based graded band gap solar cell, for which, in principle, the electron-hole collection efficiency can be enhanced considerably, resulting in acceptable open circuit output voltage and very large output current. In contrast to tandem cells, complex interconnections and current coupling are not needed in this architecture. Despite these advantages, a functioning perovskite-based graded band gap solar cell has proved elusive, likely due to excessive cation mixing. The next chapter introduces graded band gap perovskite solar cells. The supplementary figures for this section can be seen in Appendix-A.

3.1.1 Graded Bandgap Perovskite Solar Cells

Grading the energy band gap of materials is one of the key approaches to producing high efficiency solar cells and other optoelectronic devices. Graded band gap semiconductors are studied at length, but the difficulty involved in physically producing these materials in controllable ways precludes its use. For this reason, this type of solar cell is known but not fully exploited by the photovoltaic community.

The graded band gap solar cells are designed in order to maximize their solar spectrum absorption. Grading the width of the energy band forms a high in-built electric field inside the cell that drastically enhances the electron collection efficiencies. This results in a very large photocurrent output. Basically, the photo-generated charge carriers are separated and accelerated by electric field to the junctions. This charge separation results in an almost fully depleted active layer, depending on grading, while drastically reducing recombination and generation contribution. Furthermore, short circuit current densities can be remarkably improved by using impurity photovoltaic effect, impact ionization and multilevel absorption of infrared radiation [94-96]. Hence, graded band gap solar cells have great advantages over abrupt, p-n junction solar cells. However, there are not many materials available for this purpose and the available ones have challenging fabrication methods. The properties of organic-inorganic perovskites, especially their tunable band gap, makes them a suitable candidate for producing an efficient graded band gap structure.

Here high-efficiency graded bandgap perovskite solar cells with large current outputs are introduced. We fabricated mixed halide double-layer perovskite devices (layer 1: $CH_3NH_3SnI_3$ and layer 2: $CH_3NH_3PbI_{3-x}Br_x$) in order to create a graded bandgap. Perovskite layers are deposited on a heavily doped gallium nitride (GaN) substrate, which in turn serves as

an electron injection layer. A monolayer of hexagonal boron nitride (h-BN) is used as a cationic discussion barrier and adhesion promoter between these two layers, in addition to its excellent electron tunneling properties. Moreover, we manipulate the carrier transport properties in the spiro-OMeTAD based HTL by incorporating a graphene aerogel (GA). The architecture is robust and the cells reliably produce very large current densities up to 45mA cm^{-2}, with average PCEs of 18.41%, with the highest steady-state PCE topping 21.7% (freshly illuminated cells display PCEs of nearly 26%).

Fig.3.4a shows schematically the stacked architecture of the graded band gap perovskite solar cell. The positions of the key h-BN and GA components are clearly indicated. Briefly, the cells are fabricated as follows (full details in the methods section): solution processing is employed using mixed halide perovskite solutions ($CH_3NH_3SnI_3$ and $CH_3NH_3PbI_{3-x}Br_x$) on plasma etched GaN at room temperature. A monolayer of h-BN is sandwiched between these two absorbers to prevent possible cation mixing. A hole-transporting layer (spiro-OMeTAD based incorporated into GA) and a final current collecting layer (Au) are then deposited. Contact to the GaN layer is via a stacked Ti/Al/Ni/Au finger electrode. A cross sectional scanning electron microscope (SEM) image of the device is shown in Fig. 3.4b.

Fig. 3.5 shows photoluminescence (PL) spectra of typical devices and their performances under constant illumination. Photocurrent generation for a complete device (with h-BN and GA modifications) begins in the range of ~600nm to ~1300nm. The presence of broad and multiple peaks implies the formation of a graded band gap. Using Sn as an active metal cation in the first perovskite layer provides a narrow band gap in the 1.2eV to 1.5eV range [97-102].

However, Sn containing semiconductors can be strain sensitive, which can cause further narrowing of the bandgap [103]. The strain at the GaN/Perovskite interface can result in significant energy band gap shifts due to splitting of valance band degeneracy which leads to the lowest bandgap of our device, around 1eV, and results in an enhanced photocurrent generation up to 1250nm. Replacing Sn with Pb in the second layer facilitates a larger band gap between 1.5eV to 2.2eV by varying halide composition [104-107].

The experimental evidence of this effect is also shown in the absorption and steady-state photoluminescence spectra (Supplementary Fig.A-S1; in Appendix-A). The red shifts of the luminescent peaks (Supplementary Fig.A-S1; in Appendix-A) are due to this gradual increase in iodide fraction. An energy dispersive x-ray spectroscopy (EDAX) line scan analysis also shows characteristic features of cationic diffusion and confirms the variation in iodide concentration (Supplementary Fig. A-S5b; in Appendix-A).

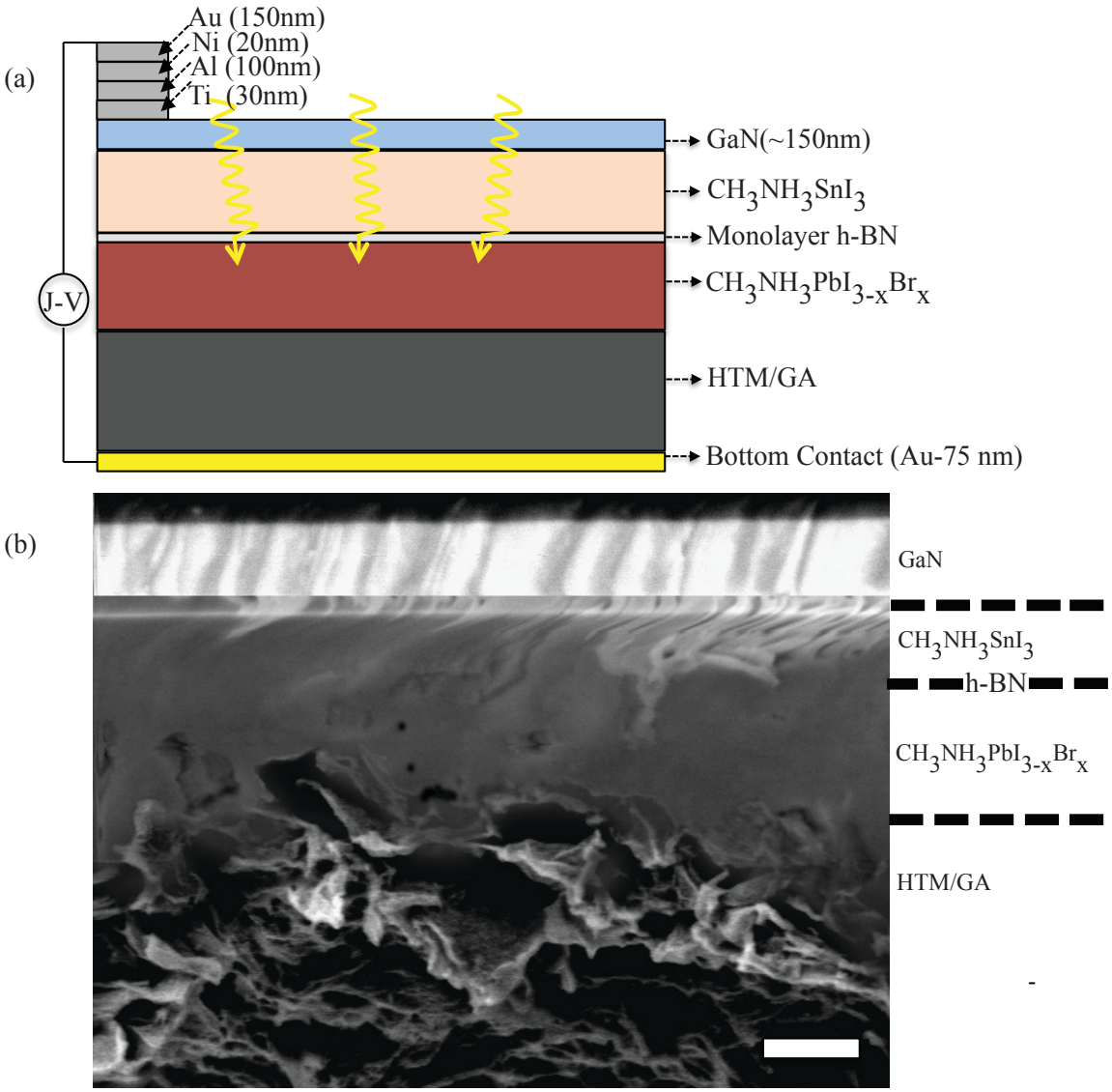

Figure 3.4 Cross-sectional schematic and SEM images of a perovskite cell with integral monolayer h-BN and graphene aerogel. a. Schematic of a graded bandgap perovskite solar cell. Gallium nitride (GaN), monolayer hexagonal boron nitride (h-BN), and graphene aerogel (GA) are key components of the high-efficiency cell architecture. b. Cross-sectional scanning electron microscopy (SEM) image of a representative perovskite device. The division between perovskite layers and the monolayer h-BN is not visible in this SEM image. The dashed lines indicate the approximate location of the perovskite layers and the monolayer h-BN as a guide to the eye. The location of perovskite layers and monolayer h-BN are extracted from the related EDAX analysis. Thickness of the $CH_3NH_3SnI_3$ layer is ~150nm and the $CH_3NH_3PbI_{3-x}Br_x$ is ~300nm. Scale bar, 200nm.

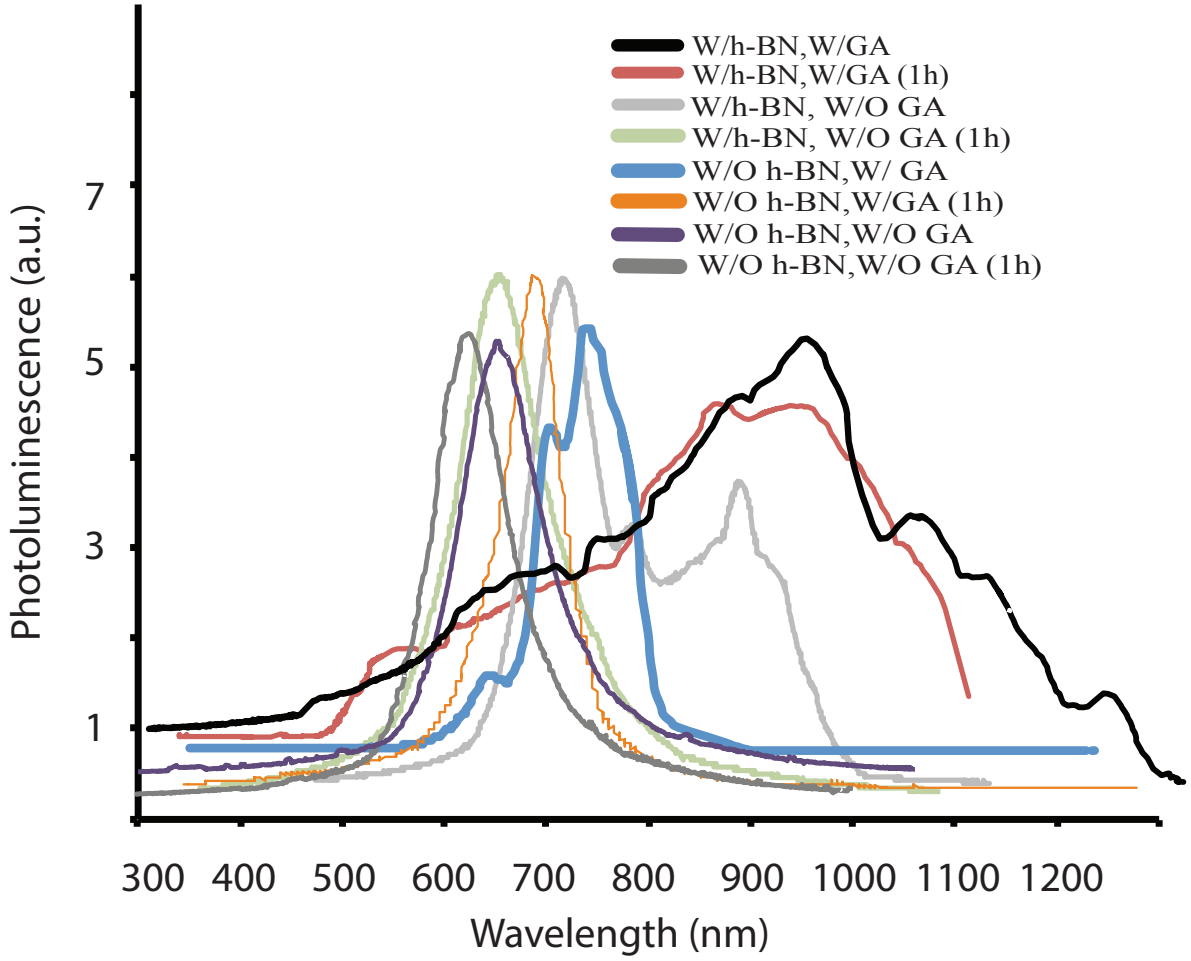

Figure 3.5 Photoluminescence (PL) spectra of perovskite cells with (W/) and without (W/O) monolayer h-BN or graphene aerogel (GA) components. The data are recorded in the steady-state regime after a few minutes of constant illumination, or after one hour (1h) of constant illumination. Cells with h-BN and GA show significant stability over time. Cells without GA but with the h-BN layer exhibit brief graded bandgap formation and moderate degradation afterwards. Cells without h-BN exhibit no graded bandgap formation.

Fig. 3.6a shows external quantum efficiency (EQE) measurements for devices with and without GA and h-BN modifications. The data shows significant differences in spectral response. For samples with h-BN and GA, the response extends up to ~1400nm (increasing the theoretical short circuit limit to 50mA/cm^2). The long wavelength absorption, higher than 1250nm, arises due to an extra PL peak in the near infrared region (NIR) which appears only under constant illumination. This light induced peak forms at ~1300nm and broadens with increased light intensity (Supplementary Fig. A-S11; in Appendix-A). This peak can be attributed to two main effects: a possible defect induced lattice absorption or a free carrier accumulation which results in charge screening at the band edges thus further reducing the bandgap. This band gap narrowing is independent of strain induced bandgap lowering and arises only under illumination [108, 109]. The EQE data also clearly indicate excellent light trapping properties due to the textured surface of GaN caused by residual etching (Supplementary Fig. A-S14; in Appendix-A). The cells without h-BN and GA modifications exhibit poor spectral response at long wavelengths which progressively decreases over time. This confirms the critical importance of h-BN and GA modifications. In the EQE data, the cells without GA also display compositional fluctuations due to ionic motion with more incomplete collection of photo-generated charge. However, the high surface area of GA helps to reduce fluctuations and improve collection efficiency. The current density-voltage (J-V) characteristics of these devices are shown in Fig. 3.6b. J-V parameters are measured (2400 Series Source Meter Keithley Instruments) under AM 1.5 illumination at an intensity of 1000Wm^{-2}. The measured short circuit current density (J_{sc}) ranges from ~25 mA/cm^2 to ~45 mA/cm^2. These large J_{sc}s are record-setting for perovskite solar cells. We suspect carrier multiplications, such as impact ionization and multi-exciton formation, might also play an important role in Jsc improvement due to a strong built-in electric field in the device [110, 111].

The cells with GA and h-BN modifications show the highest current output and efficiency. Other current-voltage trends can also be seen in Fig. 3.6b. The graded band gap formation (cells with GA and h-BN modifications) provides an effective built-in electric field, which also enhances the electron hole collection efficiency but necessarily lowers the open circuit voltage (V_{oc}). V_{oc} ranges from ~0.64V to ~0.9V for these cells and is limited by the lowest bandgap of the device.

We have found that perovskite-based solar cells have time-dependent performance characteristics. Freshly illuminated cells tend to have higher PCE, for example, than cells that have been illuminated for more than a few minutes. Fig. 3.7a shows this trend for a given graded band gap perovskite cell. Within the first two minutes of illumination and characterization, the PCE is between 25% and 26%. After approximately five minutes, the cell reaches a "steady state", with stable performance (in this case a PCE of 20.8%). In this report, the performance characteristics we quote are for the steady state. Fig. 3.7b shows a histogram for all 40-graded band gap perovskite cells measured, having the configuration shown in Fig. 3.4.

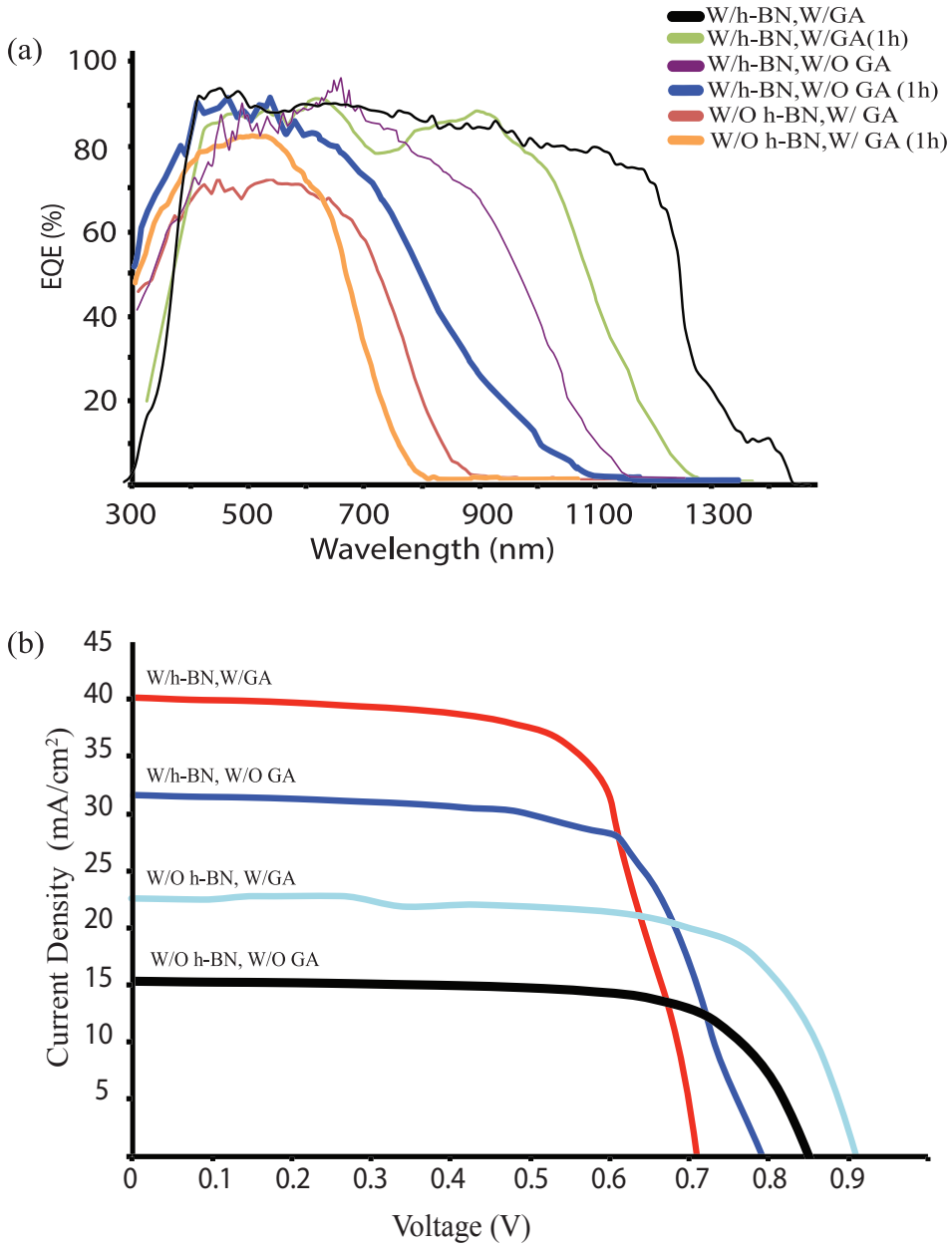

Figure 3.6 Response characteristic of perovskite cells, with and without h-BN and graphene aerogel. a. External quantum efficiency (EQE) spectra for typical graded bandgap perovskite cells with and without h-BN and GA components. The cells without GA exhibit compositional fluctuation due to ionic motion. b. Current density versus voltage characteristics of perovskite solar cells under 1,000Wm^{-2} AM 1.5 illumination, showing cells with both h-BN and GA, with h-BN but without GA, without h-BN but with GA, and without either h-BN or GA.

The average steady state PCE over all devices is 18.4%. The average fill factor (FF) for the same set of devices is 72% (not shown in Fig. 3.7b), and the cells consistently exhibit similar characteristics between reverse and forward sweep directions (Supplementary Fig. A-S9; in Appendix-A). The measured solar cell parameters of our best graded band gap cell in the steady state are J_{sc}=42.1mA/cm^2, V_{oc}= 0.688V, FF=0.75, and PCE = 21.7% (mean value of PCE=21.66%, surface area of 0.07cm^2). The current density-voltage (J-V) characteristics of this cell are shown in Fig. 3.1.1.4c and integrated spectral response can be seen in Supplementary Fig. A-S13. These, the highest efficiency cells, have Jsc=42.1mA/cm^2 out of a possible 49.4 mA/cm^2 available for a bandgap ~1eV under AM1.5 global illumination.

3.1.1.1 Role of h-BN and Graphene Aerogel

I will now further discuss the architecture and internal functioning of the graded band gap perovskite solar cells. Devices without a monolayer h-BN layer between the mixed halide double layer perovskites exhibit almost no graded bandgap characteristics at any time. Moreover, such devices consistently exhibit low performance and a rapid photocurrent decrease (Figs. 3.1.1.2 and Fig. 3.1.1.3). This demonstrates that h-BN plays a key role in facilitating the graded band gap function. EDAX line mapping of cells with and without h-BN incorporation can be seen in Supplementary Fig. A-S5b, c. Sn and Pb concentrations drastically diminish from one layer to another at the h-BN interface. This demonstrates that h-BN acts as a diffusion barrier to prevent cation mixing. Devices with h-BN and GA modifications also exhibit stable electrical characteristics even under constant illumination (Supplementary Fig. A-S6; in Appendix-A). These characteristics are likely due to increased oxidation or segregation of iodide at the interfaces of h-BN and HTM/GA. Furthermore, tin may tend to have stronger bonds with bromine at the h-BN interface, forming an intermediate medium of $CH_3NH_3SnBr_3$[99, 100].

The graphene aerogel (GA) acts as a barrier to moisture ingress (Supplementary Fig. A-S2d; in Appendix-A). The barrier may alleviate moisture penetrating into deeper depths of the absorber layer and help maintain the interface stability. It is well known that humidity exposure or a decreasing iodide fraction leads to a wider band gap perovskite up to ~2.4eV (Supplementary Figs A-S2 and A-S5; in Appendix-A) [104-109]. EDAX line mapping of the oxygen signature of a perovskite with and without GA shows dramatic differences (Supplementary Fig. A-S2d; in Appendix-A). GA also plays an important role in shaping the crystallinity and morphology of the perovskite film due to its high surface area. The GA modification is critical to obtain highly crystalline and homogeneous perovskite films, and we find that without GA modifications the perovskite films have significantly smaller grain sizes and form isolated perovskite islands rather than continuous films (Supplementary Fig. A-S4; in Appendix-A) [111]. Limiting the nucleation of small islands with the GA modification has the benefit of allowing for quick growth and aggregation, promoting large grain sizes (Supplementary Figs A-S3 and A-S4; in Appendix-A). Furthermore, the mobility also exhibits a clear dependence on the presence of a GA layer; all of the films with a GA layer exhibit better performance than without it (Supplementary Fig. A-S7; in Appendix-A). GA is a key component in ultra-high-performance devices.

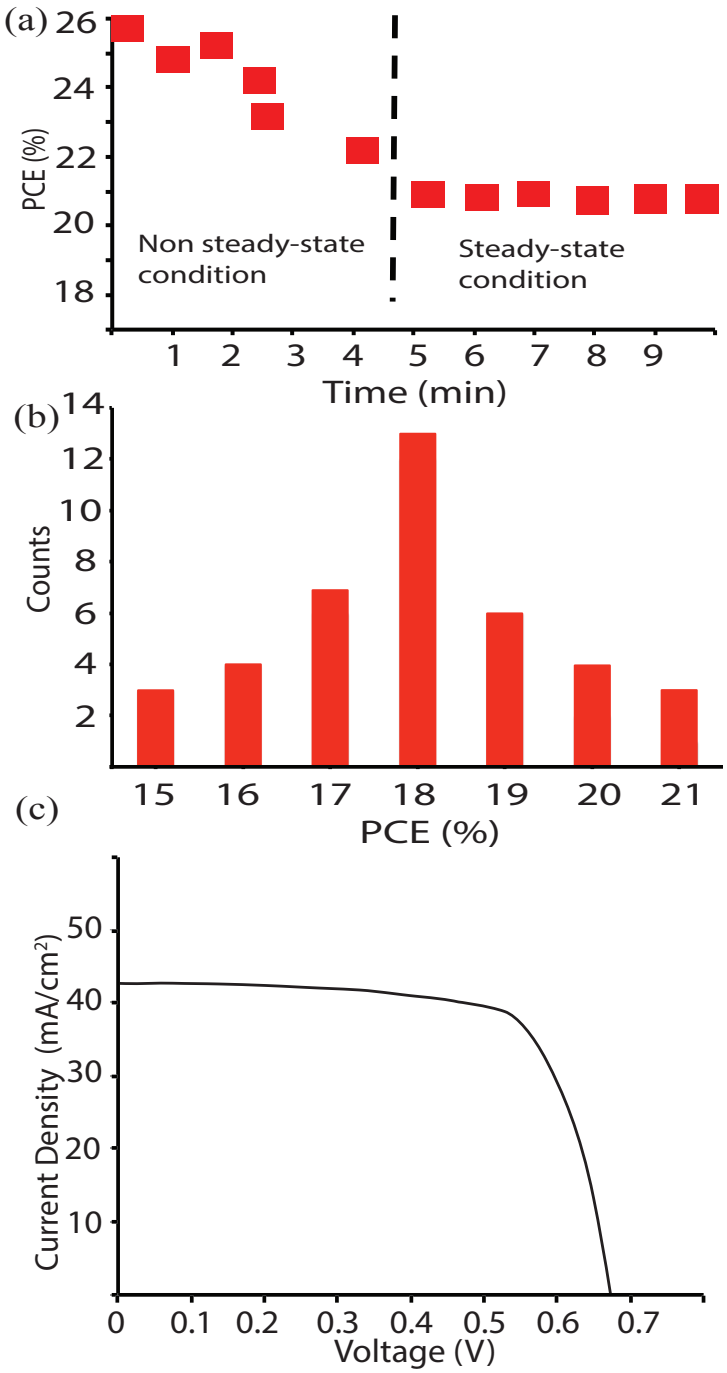

Figure 3.7 Time evolution of perovskite cell performance, with steady state histogram and best-cell current-voltage response. a. Time dependence of power conversion efficiency (PCE) for a given graded bandgap perovskite cell; the vertical dashed line indicates the onset of steady-state behavior. Freshly illuminated cells exhibit PCEs of nearly 26%, for a short period of time. After the cells reach the steady state, they exhibit stable performance at a slightly lower PCE. For this cell the steady-state PCE is 20.8%. b. Histogram of 40 graded bandgap solar cells. All PCEs are calculated in the steady state. c. J–V characteristic of a 21.7% PCE cell in the steady state, without antireflective coating.

3.1.1.2 Shockley-Queisser Limit and IR Contribution

The effective bandgap of our stabilized top performing cells is around ~1.0eV. This 1eV energy band gap can theoretically provide maximum ~0.75V and ~48mA/cm2 open circuit voltage and short circuit current densities, respectively. Thus, our reported current and voltage values are always within the Schockley-Queisser (SQ) limit.

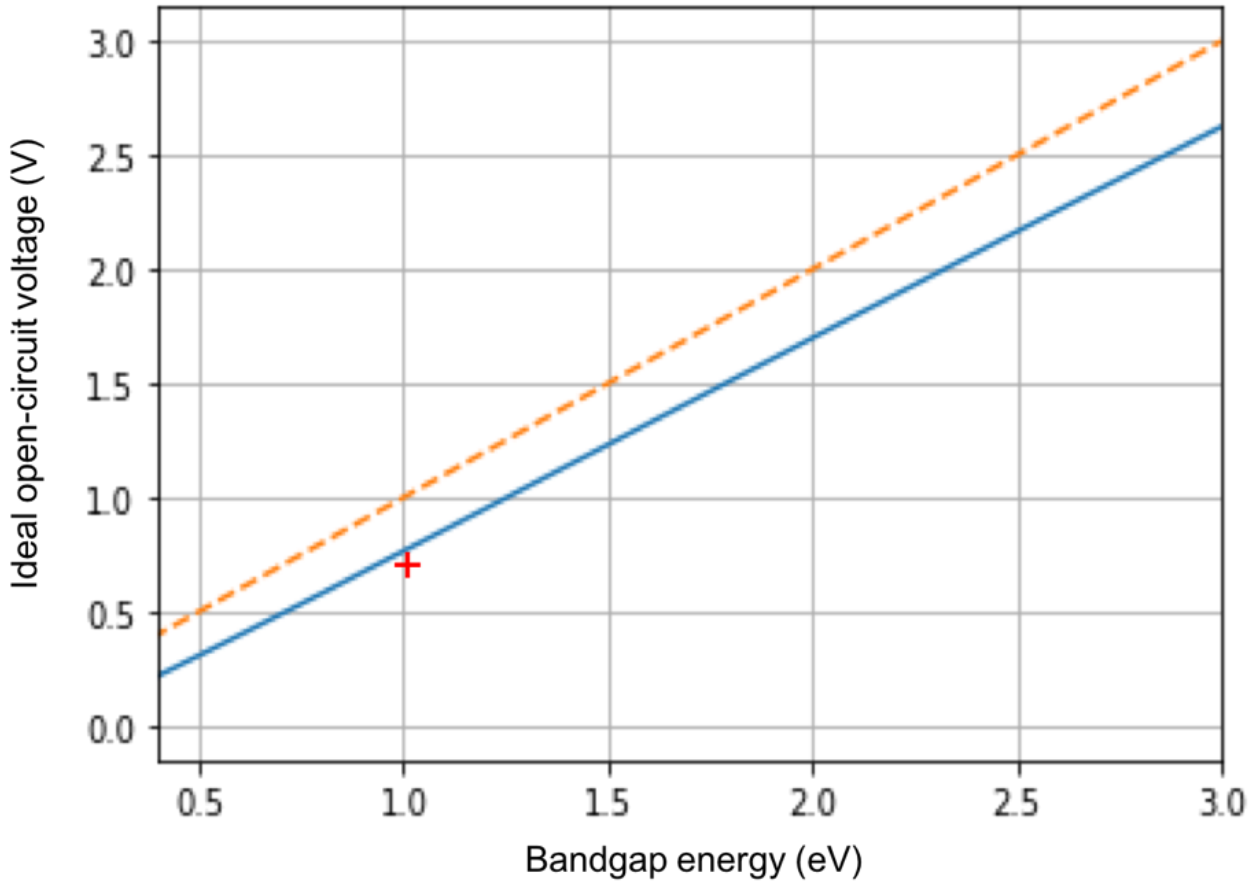

Figure 3.8 Open circuit voltage as a function of the band gap energy. Orange dotted line shows the band gap and blue solid line indicates the Shockley Quesser model. Red plus sign is associated with our highest open circuit voltage values, which is always within the SQ limit.

3.1.1.3 Long Term Stability and IR Response

We received a confirmation of the photovoltaic performance from an independent certified laboratory, Newport Inc, 439 days after the device fabrication (Supplementary Fig. A-S16; in Appendix-A). Even after this long period of time, our devices exhibit a very stable performance and one device was certified at an efficiency of 15.77%. The efficiency degradation for the certified cell is thus 76% of its original value after 10,526 hours, or a linearized decay of 0.38% per week. The longest time study for perovskite solar cells we could find in the literature gives an efficiency drop to 90% after 1440 hours [112], or a linearized decay of 1.2% per week. To the best of our knowledge, this is the longest time a perovskite solar cell has survived while maintaining high performance with almost no hysteresis. This result reinforces the importance of the graphene aerogel (GA).

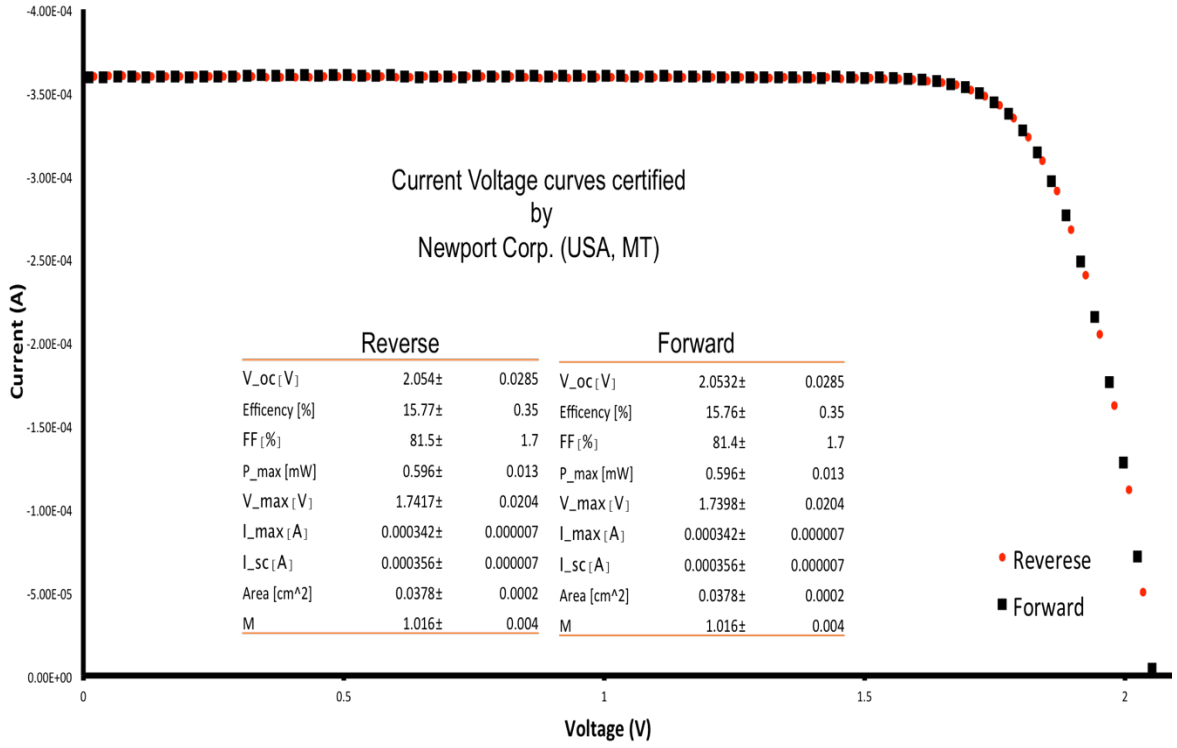

Figure 3.9 Certified I-V curves by Newport Group. After 439 days (10,526 hours) of storage, a PCE of 15.77%. Certification document can be seen in Supplementary Fig.A-S16 in Appendix A. (Device # 27)

The main cause of perovskite degradation is linked to the solubility of the active perovskite layer under moisture intrusion and humidity [113, 114] and the GA acts as a barrier to the moisture ingress. However, it should be noted that our cells have evolved during this time span, as expected in Supplementary Fig. A-S6a. The certified cell now exhibits a very high open circuit voltage (~2eV), fill factor (~80%), and almost no hysteresis. It is clear that a recombination center is formed on the h-BN, as an efficient extracting layer. However, at this point, it is very difficult to conclude why or how the perovskite is evolved to form this interface (Fig. 3.11). Most strikingly, the independent measurements by the Newport Group on our finished devices have confirmed a strong absorption beyond 1240nm (1eV) region even after 439 days (Fig. 3.9).

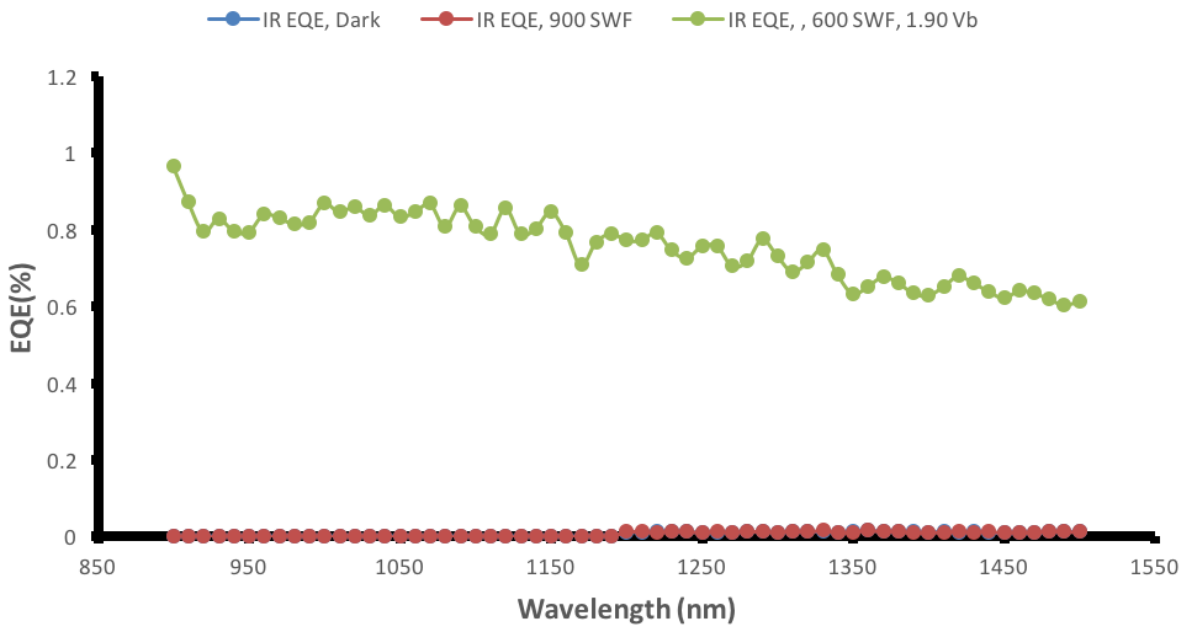

Figure 3.10 The near infrared response EQE study of complete cell after lengthy storage time (over 10,000 hours). Leakage of higher-order light from the monochromator has been confirmed not to be the origin of the EQE signal, both with #024 and with a Silicon photovoltaic reference cell which measured less than 0.1% in EQE beyond 1200nm. The measurements are taken by Newport Group. (Device #24)

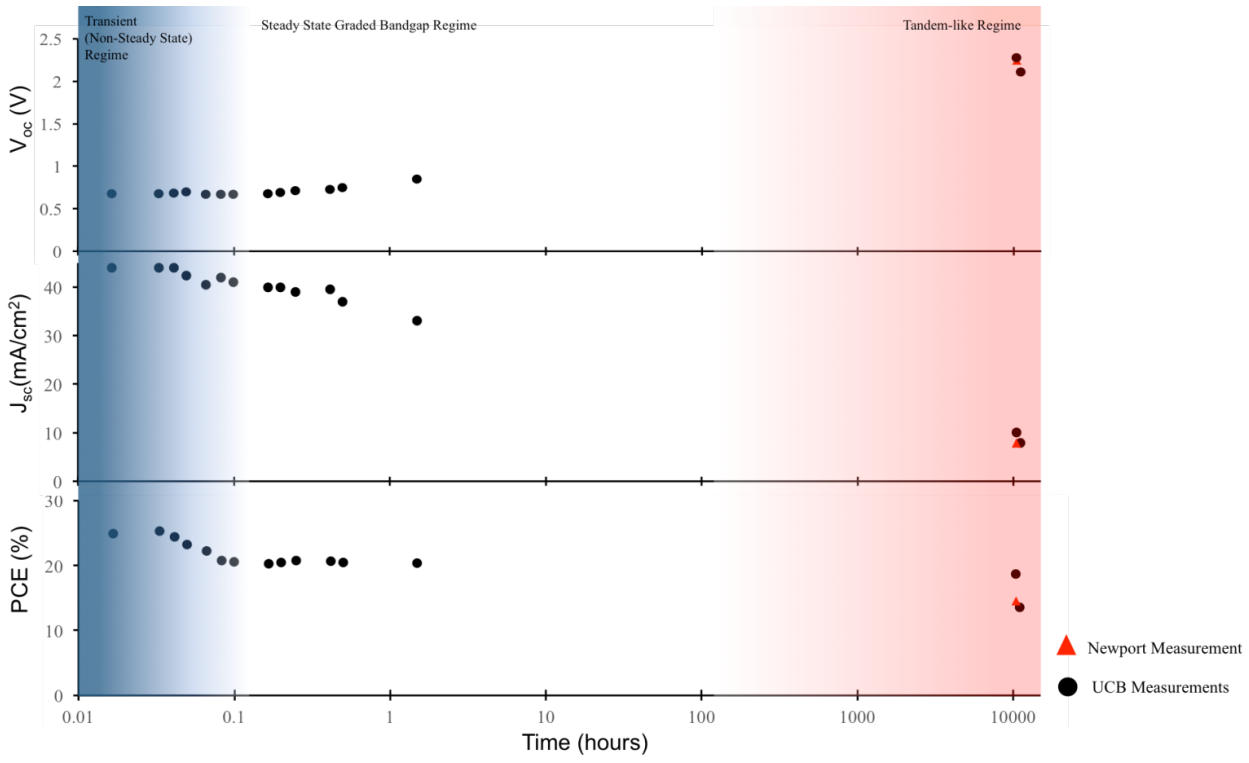

Figure 3.11 Short and long-term time evaluation of samples. The cells continue to evolve during the extensive time period but they still exhibit a high performance. These results complement our findings in Fig. A-S6.

3.1.1.4 Experimental: Fabrication and characterization

Commercial GaN on a silicon (Si) wafer was annealed at 650^{o}C for 2 hours in argon (Ar) environment. The backside of the wafer (silicon surface) was mechanically polished by diamond paste, until the silicon layer was thin. This thin layer was photolithographically masked by a silicon nitride (Si3N4) film and etched entirely by 45wt% potassium hydroxide (KOH, Sigma-Aldrich) at 110^{o}C for 14 hours. Then, a Ti/Al/Ni/Au (30/100/20/150nm) stack layer was deposited by e-beam lithography and e-beam evaporation followed by rapid thermal annealing at 850^{o}C. The GaN surface was briefly plasma etched to help evenly disperse the perovskite solution. Next, $CH_3NH_3SnI_3$ was spin coated at 4000 r.p.m for 45 seconds and crystallized at 80^{o}C. Afterwards a monolayer h-BN was transferred directly onto the prepared substrate. The HTM layer was deposited on a graphene aerogel (GA) by spin coating 2000 r.p.m for 30 seconds and then left at room temperature for 5 min. Subsequently, $CH_3NH_3PbI_{3-x}Br_x$ was spin coated on this GA/HTM layer at 3000 r.p.m for 30 seconds and the film crystallized at 60°C. This second layer was gently placed onto the first layer, in the glove box, and annealed at 60°C. Finally, a 75nm thick gold (Au) electrode was evaporated on top of the HTM/GA layer. $CH_3NH_3SnI_3$ and $CH_3NH_3PbI_{3-x}Br_x$ were synthesized according to procedures published in reference [115-117] and [118-123]. The HTM layer was prepared according to refs. *89* and *98*. h-BN was prepared as in ref. *124* and the GA sheets were prepared by the gelation of a GO suspension. The aqueous GO suspension (2wt%) was prepared by ultrasonication. In a glass vial, 3ml of the GO suspension was mixed with 500uL (microliter) of concentrated NH_4OH (28-30%). The vial was sealed and placed in an oven at 80°C overnight. The resulting wet gel was washed in deionized water to purge NH_4OH followed by an exchange of water with acetone inside the pores. The washed gel then underwent supercritical drying by using CO2 and was converted to the final graphene aerogels by pyrolysis at 1050°C under nitrogen flow [124].

The XRD spectra were measured using a Siemens D500 X-ray diffractometer, and EQE measurements were performed using a QEPVSI measurement system (Newport 300 W xenon lamp, 66920, Newport Cornerstone 260 monochromator, and Lock-in amplifier SRS810). UV/VIS absorption spectra were recorded on a PG T80 spectrophotometer in the 1190-1100nm wavelength range at room temperature. Photoluminescence spectra were measured with a modified Renishaw inVia Raman microscope (Ar ion laser 514nm and 488nm and HeNe 633nm). J-V curves were measured using a solar simulator (Newport, 91195A) with a source meter (Keithley 2420) at 1000W/m2 AM 1.5 illuminations, and a calibrated Si-reference cell certified by NREL. The voltage sweep was maintained at very slow rate (<10mV/s-1), to ensure that the device reached its equilibrium and yielded a hysteresis-free response. J-V data were also corrected by the spectral mismatch factor, calculated to be less than 1%. All devices were measured while masking the active area with a metal mask of size 0.07 cm2. All measurements were conducted at room temperature in air.

The bottle neck of this fabrication process is transferring the h-BN on to the receiver substrate. With the method described above, we successfully deposited perovskite before the h-BN transfer. However, with later h-BN batches this method did not provide successful results and the devices began to fail. We linked this failure to contamination and accumulation of polymer residue. Therefore, we developed an alternative method called the syringe method. In the syringe method, h-BN is transferred first followed by perovskite injection. This injection works with capillary force that guides the perovskite under the h-BN to the active area. The

perovskite should only be introduced from one side to avoid full surface coverage. (For more detailed fabrication steps, refer to Appendix-A.)

3.1.1.5 Conclusion and Future Work

Graded band gap perovskite photovoltaic cells are prepared successfully with outstanding output current and power efficiency by implementing a new cell architecture. GaN is chosen to replace typical TiO2 ETL to provide a better surface morphology and enhanced electron injection due to its ability to dope heavily. A graphene aerogel makes an excellent barrier layer to moisture ingress and improves hole collection efficiency in the HTL. The aerogel also promotes a more crystalline perovskite structure. Choosing the right metal cation and varying halide anion concentration also successfully establishes band gap tuning of the perovskite absorber layer. The combination of GA and h-BN enables this band gap formation, and this configuration produces cells that are remarkably reproducible and stable.

3.2 Metal Insulator Semiconductor Photovoltaics

Metal insulator semiconductors (MIS) are also another promising photovoltaic architecture, which retain similar electronic properties to p-n junction diodes and have a highly efficient, low cost solar energy conversion. Metal and a semiconductor interface deliberately produce a Schottky junction. The properties of this junction highly depend on the work function of the metal and semiconductor. However, intensive surface recombination and possible fermi level pining occur when the metal and semiconductor directly contact with each other. Thus, the work function difference between metal and semiconductor becomes insignificant.

However, inserting a very thin insulating layer between the metal and semiconductor provides more precise control over the Schottky barrier height and carrier recombination by blocking majority carrier diffusion between the metal and semiconductor. Even though MIS solar cells were first introduced decades ago, the lack of proper interface engineering to manage such sensitive surface states hindered the production and application of MIS base solar cell structures. 2D layered material is a promising candidate for suppressing the interface recombination and charges. In the next chapter, we demonstrate cuprous oxide (Cu_2O) based metal insulator semiconductor Schottky (MIS-Schottky) solar cells with power conversion efficiency exceeding 3%. Even though the efficiency number seems low compared to our perovskite solar cell architecture, this device is one of the most efficient of any Cu_2O, based MIS-Schottky solar cell. In this architecture, we use Cu_2O as an active semiconducting layer and h-BN as an insulating and passivating layer. This architecture is another example of the effective application of two-dimensional (2D) layer materials in energy harvesting devices.

3.2.1 Metal insulator semiconductor solar cell devices based on a Cu2O substrate utilizing h-BN as an insulating and passivating layer

Cuprous oxide (Cu_2O) has been investigated off and on as a possible non-toxic, low-cost, earth-abundant photovoltaic material for several decades [121-123, 125-127]. Unfortunately, Cu_2O is exceedingly difficult to chemically dope, limiting its application for conventional p-n

junctions [125-127]. In 1979, L.C Olsen suggested that a high efficiency Cu_2O solar cell might be possible using either a metal insulator semiconductor Schottky (MIS-Schottky) configuration, or a heterojunction. Both offered a highly attractive theoretical conversion efficiency of ~20% [121-123, 125, 126]. The highest conversion efficiency for a Cu_2O- based system is 5.38%, reported for a heterojunction solar cell using undoped gallium oxide (Ga_2O_3) as a buffer middle layer for Al-doped ZnO/Cu_2O [116, 117]. However, in the thirty-five years since Olsen's prediction, no notable Cu_2O-based MIS-Schottky devices have been realized, presumably due to difficulties with highly sensitive surface states of Cu_2O [115-117, 121-123, 126, 127]. There have been many reports of Metal/Cu_2O Schottky junction solar cells, but even these cells struggle to achieve efficiencies over 2% due to dangling bonds on the surface and uncontrolled reduction of the Cu_2O on the surface to an undesirable copper-rich phase [115-117, 121-123, 128-133].

Here we demonstrate a unique direct growth technique utilizing copper and hexagonal boron nitride (h-BN) to create a stable MIS-Schottky solar cell structure. The h-BN layer serves simultaneously as a passivation and insulation layer on the active Cu_2O film; formation of an undesirable copper-rich interface layer is thus prevented. The resulting MIS-Schottky solar cell devices display high short circuit current density (J_{sc}) and open circuit voltage (V_{oc}) with a conversion efficiency as high as ~3.44%.

This is one of the highest efficiencies yet reported for a Cu_2O- based MIS-Schottky solar cell device and a direct experimental demonstration of two-dimensional layer materials in energy conversion devices.

Figure 3.12 illustrates two related fabrication processes we have employed for our Cu_2O MIS-Schottky structures, which we label Type 1 and Type 2. The devices are constructed using 0.025mm thick copper foil with a ~15nm thick h-BN layer grown by chemical vapor deposition (CVD), (Figs. 3.12a & b) [134]. Because h-BN grows on both sides of the copper foil, a light polishing is applied to the bottom layer to allow oxidation to proceed through the bottom surface (Fig.3.2.1c). Cu_2O growth is performed with a standard two-step oxidation process to achieve larger grain size (Fig. 3.2.1d) [135-139]. Next, an annealing step is performed at 850^{o}C for 2 hours in 1 Torr O_2 partial pressure in order to lower the defect density to improve mobility. High temperatures are necessary in order to convert copper to cuprous oxide, in the correct phase [126, 129, 135, 137, 138, 140]. However, oxidation of thin copper foil at high temperatures is a challenging process due to its thermal expansion and crystallization behavior. Fortunately, the relatively thick hexagonal boron nitride layer provides additional mechanical strength to the foil during growth and allows for easy handling of the material after growth. During step (d), following the growth and annealing steps, the substrates are slowly cooled in one of three different gaseous environments: argon/oxygen (Ar/O_2), nitrogen (N_2), or hydrogen (H_2). By introducing different gas environments, we induce distinct passivation layers on the top surface of the Cu_2O. This passivation process is enabled by the h-BN layer. The h-BN layer also obviates the traditional wet etching process for a possible cupric oxide (CuO) layer on the top surface of Cu_2O [139, 140]. Since in our process a cupric oxide (CuO) layer is formed only on the bottom surface of the oxidized foil, the top surface is being protected by the existing h-BN layer (Fig. 3.13b)

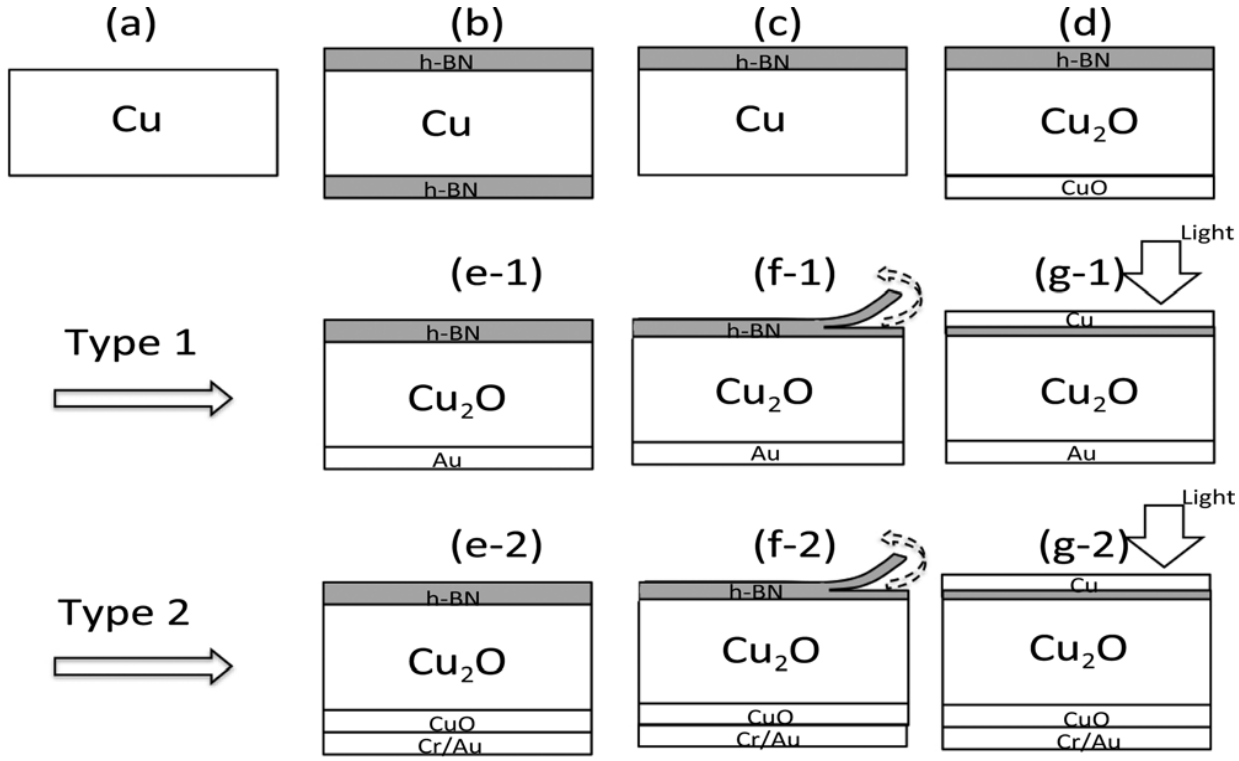

Figure 3.12 Cross-sectional schematic diagram of Cu_2O based MIS cells, type 1 and type 2. a-c. A 15nm thick h-BN layer deposited on 0.025mm thick copper foil via CVD followed by applying a light polish to the bottom layer to remove h-BN from the back surface. d. The Cu foil is oxidized using a standard two-step annealing process to form a Cu_2O layer . In this oxidation step, different carrier gases (Ar/O_2, N_2, and H_2) are introduced during cooling. CuO formation is only occurring at the bottom surface of the Cu_2O, not at the h-BN/Cu_2O interface. e-2. For type 1 devices, this CuO layer is removed by lightly polishing and 10nm Au is deposited as a back contact. f. The h-BN is exfoliated. As a final step, a 5nm thick transparent Cu layer is deposited as a top contact. The process of a type 2 structure is identical to type 1, except step (e). In this step for the type 2 device, CuO is not polished and Cr/Au is deposited as a back contact (5nm/10nm), followed by annealing at 200^oC in an Ar environment. We achieve up to 2.3% and 3.44% efficiencies for type 1 and type 2 devices, respectively. g. Illumination direction is shown by the arrows.

To produce a Type 1 device, the bottom surface of the foil following conversion is lightly polished to remove the CuO layer followed by ~10nm thick Au film deposition as a back contact (Fig.3.12-(e-1)). To produce an MIS cell, the h-BN layer is thinned by exfoliation, using the standard scotch tape and polydimethylsiloxane (PDMS) stamp techniques, decreasing the h-BN thickness in a range of ~1nm to ~6nm (Fig. 3.12-(f-1)). This exfoliation process is crucial for forming a proper MIS device structure utilizing h-BN as an insulator layer. As a final step, a ~5nm thick transparent copper layer is evaporated on the top surface of the exfoliated h-BN layer as a top contact. The composition of a Type 2 structure is identical to Type 1, except for step (e). In this step for Type 2, CuO is not polished off and Cr and Au are deposited, 5nm and 10nm thick respectively as a back contact, followed by an annealing process at 200^0C in an Ar environment (Fig. 3.12-(e-2)). This annealing process helps Cr diffuse into the CuO layer to create a degenerately doped region.

Fig. 3.13(a) shows an optical image of the complete device and Fig. 3.13(b) shows a cross-sectional SEM image of h-BN/Cu_2O at step (d) in Fig. 3.12. Fig. 3.13(b) confirms that there is no CuO formation on the h-BN/Cu_2O interface. The quality of cuprous oxide is characterized by X-ray diffraction (XRD) (Fig. 3.14(a)) and optical transmission spectroscopy (Fig. 3.14(b)). As seen in Fig. 3.14a, the sharp diffraction peaks indicate high quality Cu_2O. The h-BN formation seems to prevent unwanted CuO formation on the top surface of Cu_2O layer, which correlates with Fig.3.13b. The optical transmittance spectra in Fig. 3.14(b) indicates a band-gap of ~2.08eV (λ=595nm) using the standard absorption fitting method. This value is consistent with band gap values reported in literature of Cu_2O (2.0-2.1ev) [125, 126, 140]. The depth of oxidation is also easily controlled by varying the growth time. For instance, a buried Cu/Cu_2O layer is readily achieved using short growth times (Supplementary Fig. B-S1; in Appendix-B).

In order to verify that the h-BN layer remains intact after Cu_2O growth, we employ Raman spectroscopy. The Cu_2O substrate is slowly etched using saturated nitric acid and the h-BN is transferred to a Si/SiO_2 substrate for analysis. As seen in Supplementary Fig. B-S2, the signature B-N vibrational E_{2g} peak of h-BN is observed at 1366.7 cm^{-1}[134, 136]. The thickness of h-BN on devices is estimated via capacitance measurements. High-frequency (1MHz) capacitance-voltage (C-V) characteristics are measured at room temperature using an HP4192 A LCR meter. Capacitance, which is inversely proportional to the thickness of the dielectric, is measured on exfoliated h-BN/Cu_2O substrates by probing during electrical measurements. The exfoliation process makes the h-BN layer thin enough to allow the tunneling current transport process. We estimate the thinnest h-BN layer to be approximately 2nm from electrical response analysis. The two other thicker layers were approximately 5nm apart as demonstrated by decreasing the dielectric capacitance in the C-V curve; which is also consistent with atomic force microscopy (AFM) measurements (Supplementary Figs B-S6 & 8; Appendix-B).

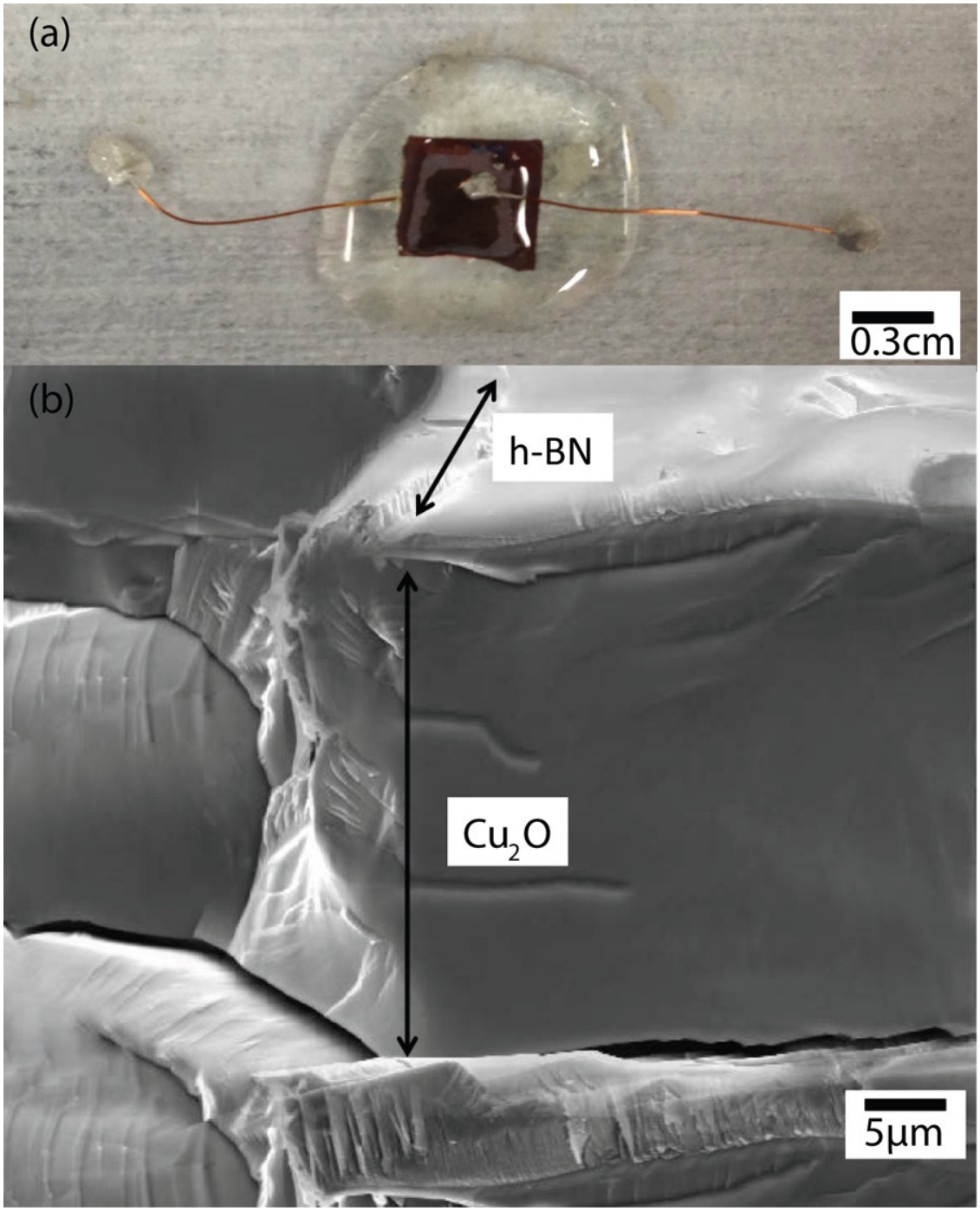

Figure 3.13 a. Optical photograph of complete device structure of MIS- Schottky solar cell. b. Cross sectional SEM image of h-BN on Cu2O. There is no CuO formation on the h-BN/Cu2O interface. The boron nitride layer remains intact after Cu2O growth. (See supplementary material for performed Raman spectroscopy in Appendix B).

Fig. 3.15a shows I-V curves of several different MIS solar cells under AM1.5G illumination. It is clear that the electronic properties of the solar cells are directly affected by the kind of cooling gas used during synthesis. Thin films of polycrystalline Cu_2O are expected to have many dangling bonds, which act as an interface recombination center on the grain surface [130, 131, 141-143].The improvement of the short circuit current density could be a clear signature of reducing interface states and increasing carrier collection efficiency, which is a sign of active passivation while trapping hydrogen and nitrogen between interfaces (Fig. 3.15a). The improvement of front and rear surface recombination is also shown in the external quantum efficiency measurement (Supplementary Fig.B-S7; in Appendix-B). Another important characteristic of the h-BN layer is that it prevents the formation of copper-rich interface layers, which is linked to lowered efficiency in metal/Cu_2O devices due to tuning of the work function and is correlated with low open circuit voltage (V_{oc}) [126, 128, 129, 140]. We also suspect monolayer nitrogen doping under the h-BN layer, which controls Fermi level pinning at the interface (Fig. 3.15a) [121-123, 125, 126, 141-143].

The overall photovoltaic cell efficiency of the Type 1 device produced in hydrogen is approximately 2.3% with 12.1 mA/cm^2 current density over an area of 0.35cm by 0.4cm. The h-BN appears to play an essential role in improving device performance, as the devices fabricated without h-BN layer are consistently less responsive to cooling gases. Non-h-BN devices also display a marked decline in device performance, especially when hydrogen gas is introduced into the system due to Cu_2O surface reduction. However, we have observed V_{oc} increase in the device with O_2 cooling due to increase in grain dimensions, as predicted in literature [137, 138, 140-144].

For selected Type 2 devices, we employ Cr/Au as a contact layer on the back surface of the Cu_2O/CuO interface. Later, the device is annealed at 200°C in an Ar environment to allow Cr diffusion into the cupric oxide, which results in an improvement in V_{oc}. Although more experiments are needed to clarify the contribution of various interfaces, it is likely the diffusion of Cr into the Cu_2O/CuO interface that provides an additional band offset leading to an increase in V_{oc}. No improvement has been observed in Type 1 devices with a Cr layer. Despite a small increase in resistivity and a decrease in the short circuit current (I_{sc}), the overall efficiency of such a Type 2 device is improved to 3.44%, in contrast to ~2% we observed previously for Cu_2O based Schottky devices. No anti-reflection coating is necessary for this improvement (Fig. 3.15b). 3.44% is the highest efficiency reported for Cu_2O based Schottky solar cells.

We have observed that for both Type 1 and Type 2 devices, a non-uniform thickness of the h-BN layer influences the current tunneling ability of the device, and hence the noise response. Variable thickness h-BN results in the fill factor (FF) directly dependent on the rate of bias sweeping. We note that fast voltage sweep rates (1msec) reflect a very different FF than slower (~1sec) voltage sweep rates and increased FF affects the apparent efficiency of the device (Supplementary Fig.B-S3; in Appendix-B) [145].

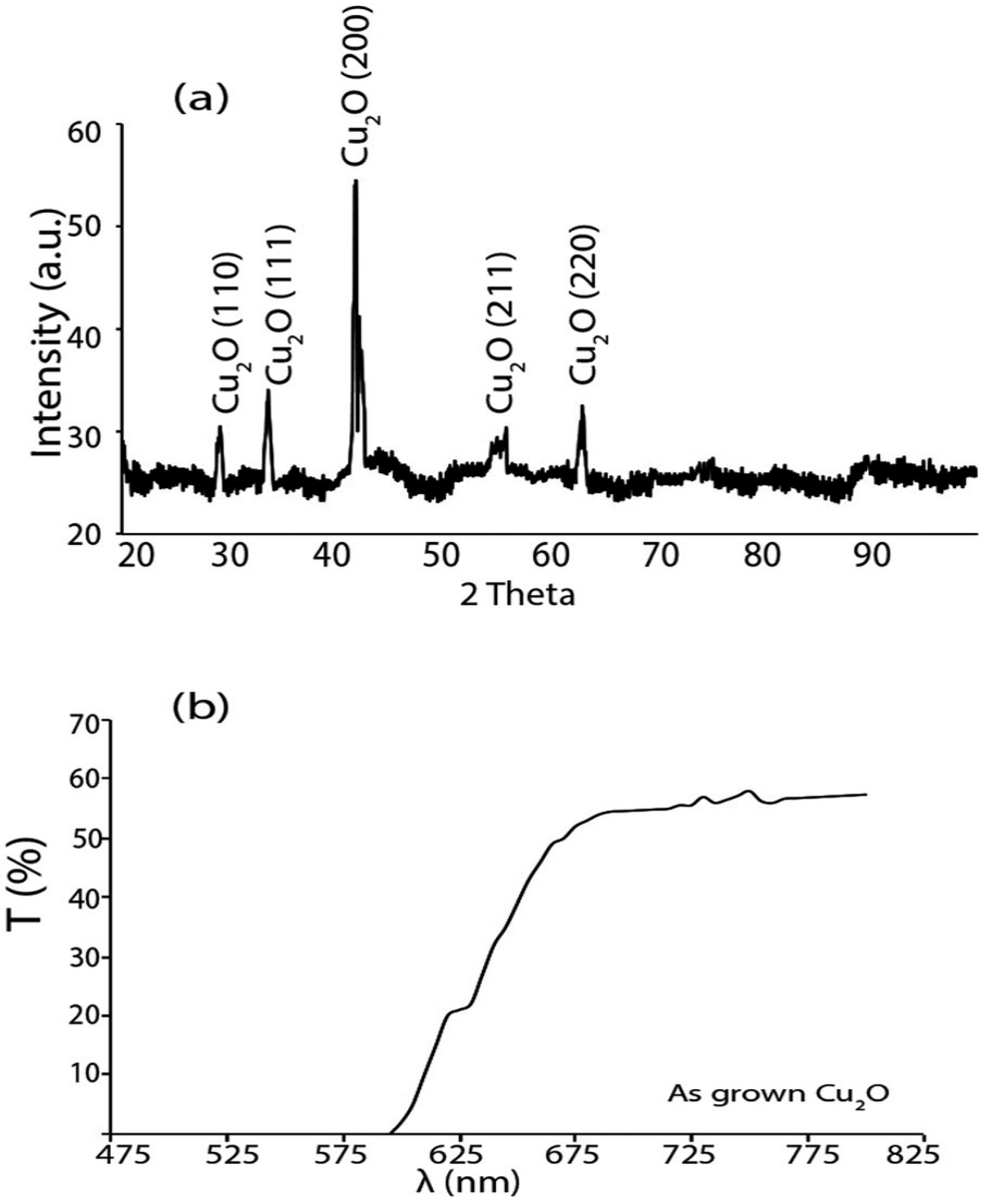

Figure 3.14 a. X-ray pattern of a grown Cu2O. The sharp diffraction peaks indicate high quality Cu2O. b. Short-scan of optical transmittance spectra, at room temperature, indicates energy band gap equal to 2.08eV using absorption fitting method. Both figures show high quality Cu2O material formation.

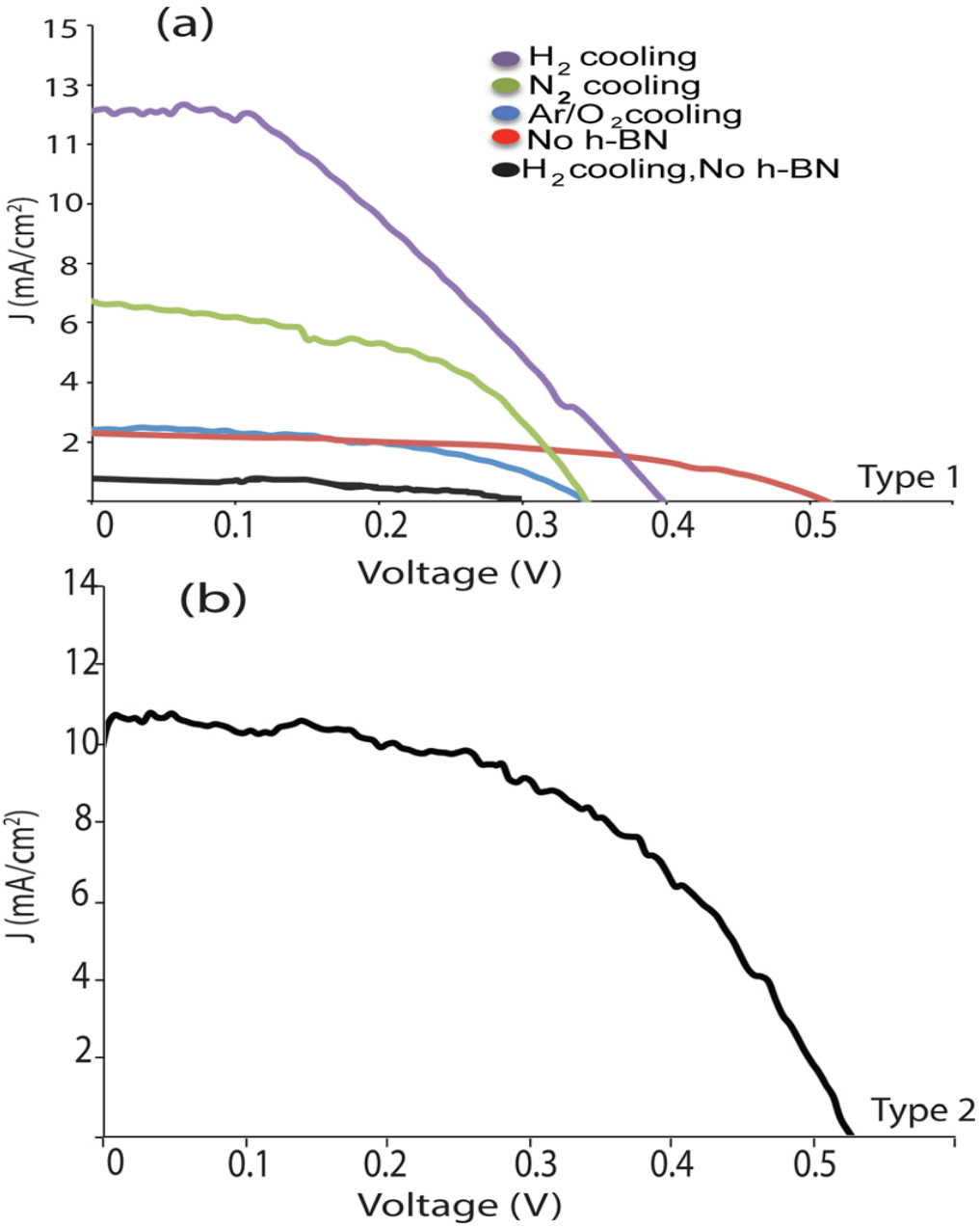

Figure 3.15 a. J-V curves of type 1 device structures show remarkable short circuit increases with respect to Cu/Cu_2O devices utilizing different cooling gas environments, Ar/O_2, N_2, and H_2, respectively, N_2 and H_2 cooling remarkably increases J_{SC}. The overall photovoltaic cell efficiency of the device cooled in hydrogen is approximately 2.3% with 12.1 mA/cm^2 current density over an area of 0.35cm by 0.4cm. This graph indicates that h-BN plays a very important role in improving device performance because the devices fabricated without h-BN layer are not favorable. b. J-V curve of type 2 device structure indicates having CuO and Cr/Au combination at the back surface of Cu_2O helps to increase V_{OC} and solar conversation efficiency. The efficiency of this device is 3.44% with V_{oc} 0.52 V.

3.2.2 Experimental: Fabrication and characterization

CVD h-BN was grown on 0.025mm thick copper foil (99.999% Puratronic, Alfa Aesar), which was then cut into 0.2cm by 0.3cm pieces. The back surface of the sample was mechanically polished to increase the bottom to top oxidation rate. The two step thermal oxidation process was carried out for 30 minutes at 950 ^{0}C with O_2 partial pressure of 2.7 Torr followed by 2 hours at 850 ^{0}C with O_2 partial pressure of 1 Torr. After the Cu_2O growth, the chamber and all gas lines were purged with 200sccm of argon to remove all the O_2 from the system. Next, only one of the three transport gases, Ar/O_2, N_2, and H_2, was introduced in the chamber during the cooling process under a partial pressure of 1 Torr. After cooling, the back surface of the substrate was slightly polished, for Type I only, followed by deposition of a 10nm Au film and bonding of a thin copper wire. Then, the sample was carefully attached to a glass slide using an epoxy glue. The sample was exfoliated using a combination of scotch tape and PDMS stamp techniques. Finally, the substrate was loaded into a thermal evaporator for the deposition of a ~5nm Cu layer as a top contact electrode.

3.2.3 Conclusion and Future Work

We have demonstrated a versatile route toward the controllable synthesis of a cuprous oxide solar cell, with an efficiency of 3.44%, using a surface sensitive thin film of h-BN and a back CuO layer to increase the band offset. The ability to control passivation of the non-radiative recombination centers and donor-like defects is suggested, in addition to inhibiting reduction of the Cu_2O surface, which is another contributor in blocking out the majority carrier flow to reduce the reverse saturation current [118-123]. This technique has advantageous features including easy fabrication, the ability to use thinner Cu foil, and prevention of an unwanted CuO layer. It is also highly generic and has great potential to construct an exquisite passivation on the sensitive surfaces in combination with hydrogen and nitrogen treatment.

We also note that in this current work we evaporated top contacts of sufficient thicknesses to avoid pinhole shorts. In our future work, we hope to optimize the contacts and achieve even higher efficiencies. In the future, this technique might be used to design high efficiency, low cost, and stable solar cell structures.

PART III

Chapter 4

Energy Storage Devices

Since the discovery of electricity, the issue of storage has been a relevant concern for sustainable development. The need for electricity is inevitably increasing every day, but the lack of effective electrical energy storage capabilities makes it more challenging to balance this rising demand. For this reason, over the last century, science and technology in electrical energy storage has continued to evolve in order to fulfill the rising needs for electrical energy. Today, rechargeable lithium ion batteries are widely used as major electrical energy storage systems and as a primary power source. By powering a wide range of commercial products from small portable computation and communications devices to electric vehicles, lithium ion batteries (LIBs) have become an integral part of everyday life for most individuals. However, power demands on LIBs are ever increasing, and as such the batteries are often operated close to or even exceeding design limits. Thermally-induced internal breakdown is alarmingly common, sometimes leading to catastrophic failure (fire or explosion). For this reason, producing explosion and fire-resistant LIBs are essential requirements for next-generation battery systems.

Aside from physical safety concerns, there are still various unanswered questions concerning whether LIBs will truly satisfy future energy storage demands or not. The expected development of the electric vehicle industry alone will exponentially increase the electrical energy storage demand over the next decade. Limited theoretical energy densities of LIBs present the opportunity for new battery chemistries and designs to reach higher energy densities for next-generation energy-storage systems.

In the next chapters, I will first introduce a new architecture towards explosion proof Li-ion batteries by incorporating either boron nitride aerogels (BNAG) or boron nitride nanotubes (BNNTs) into the electrolyte complexes. Then, I will discuss another rechargeable battery chemistry, lithium air (Li-air), with extremely high theoretical energy densities compared to LIBs.

4.1 High-temperature explosion-resistant Li-ion battery cells utilizing boron nitride aerogels

Despite the many advantages and wide commercial usage of lithium-ion batteries (LIBs), there remain substantial performance limitations and safety concerns [146-149]. The most serious safety issue involves operating temperature range and stability. An increase in internal temperature of the battery cell can lead to internal pressure build up due to an accelerated reaction rate between the electrolyte and electrodes. Mechanical stress then damages the electrolyte and separator, resulting in an increased internal resistance and thermal runaway. The cell may then short circuit and possibly explode [146, 147, 149, 150]. Since LIBs self-heat naturally as they are operated (discharged or charged), developing LIBs with high temperature operation capability is vital for overall safety and reliability. Today's commercial LIB cells are

typically unreliable if operated above 60^0C, and virtually none can survive operation above 100^0C [147, 150].

To achieve a Li-ion cell capable of relatively high temperature operation (T>60^oC), the liquid electrolyte can be replaced with a polymer electrolyte. This yields other benefits including enhanced processability, flexibility, and lighter weight [150-152]. However, polymer electrolytes still lose their integrity at temperatures above 100^0C. This has led to an examination of reinforced polymer electrolytes. The reinforcements are largely designed to increase strength, toughness, and flexibility of the polymer. Carbon based materials, such as carbon nanotubes and exfoliated graphene, have been explored for such modifications [43, 153, 154]. Hexagonal boron nitride (h-BN) flakes have also been employed [150]. Unfortunately, none of the polymer reinforcements have resulted in battery cells that maintain high temperature (T>150^oC) structural integrity and cyclability.

h-BN nanomaterials are worth a second look. The layered honeycomb structure of h-BN closely resembles that of graphite. It is important to note, however, that nanostructured h-BN often displays physical properties far superior to those of its carbon counterparts, such as higher oxidation resistance and outstanding high temperature stability, with no compromise in mechanical strength [43]. h-BN can be synthesized low dimensional forms counterpart to carbon-based structures, such as BN nanotubes (BNNTs) [155] , BN nanosheets [156], and BN aerogels (BNAGs) [45].

4.1.1 Result and Discussion

Here we report a high-temperature electrolyte-complex (HTEC) for LIBs by embedding BNAGs into polymer-ionic liquid gel to increase the electrolyte temperature stability. The advantages of chemical inertness, thermal stability, and high surface area of BNAGs together serve to elevate the reliable and safe battery operation temperature to 200^0C, while still maintaining high capacity and cyclability. Most importantly, even under adverse high temperatures, high current discharging or charging conditions, the BNAG modified LIBs cells appear immune to catching fire or exploding. We performed comparison tests with unfilled polymer electrolyte and polymer electrolyte filled with other BN-based materials. BNNT fillers are also remarkably effective, but with slightly lower performance characteristics compared to BNAG fillers. h-BN flake fillers produce markedly inferior Li-ion battery cells (see Supplementary Materials in Appendix-C).

Electrolyte complexes are prepared by mixing BNAG (or BNNTs) with polymethylmethacrylate (PMMA) and polyacrylonitrile (PAN) (1:2:9 weight percentages) dissolved in anisole. Subsequently, this mixture is incorporated into the ionic liquid PYR_{14}-TFSI-LiTFSI (PYR_{14}: N-methyl-N-butylpyrrolidinium, TFSI: bis(trifluoromethylsufonyl)imide). Occasionally TiO_2 nanoparticles are added to the solution in order to enhance the concentration of ions in the cell. We use the most common, commercially available electrodes for our anode and cathode: lithium titanate ($Li_4Ti_5O_{12}$) as the anode and lithium-rich manganese oxide ($Li_{1+x}Mn_{2-x}O_4$) as the cathode. The $Li_4Ti_5O_{12}$ is a high performance, zero strain electrode with a lithium insertion potential of 1.55V. $Li_{1+x}Mn_{2-x}O_4$ has excellent compatibility with $Li_4Ti_5O_{12}$ due to the similar spinel structure [157]. More details about materials synthesis and sample preparation can be found in the Methods section.

We first characterize cells based on their ionic conductivities and concentration. One potential concern for BN filler materials is although they can be used to form more mechanically stable polymer electrolytes, their insulating properties can lower ion concentrations and inhibit

their motion across the cell. The lithium ion transference number (t_{Li}^{+}) readily determines the ion concentration gradient in the electrolyte during the charge as well as discharge process and is related to the number of moles of lithium ions passing through the electrolyte per unit capacitance. In order to determine the transference number for our BNNT and BNAG samples, we prepare lithium symmetric cells (Li/electrolyte/Li) and use a previously described dc polarization measurement[158-160]. Results of these measurements are reported in Table 4.1.

Table 4.1 Lithium transference number for different electrolyte gel composition, at selected temperatures.

Electrolyte gel	Solvent ratio	t_{Li+} (24^0C)	t_{Li+} (60^0C)	t_{Li+} (80^0C)	t_{Li+} (100^0C)
PAN-PMMA	2:9	0.652	0.691	0.713	0.774
BNAG-PAN-PMMA	1:2:9	0.482	0.501	0.532	0.593
BNNT-PAN-PMMA	1:2:9	0.392	0.412	0.443	0.501
TiO_2-BNAG-PAN-PMMA	1:6:2:7	0.583	0.596	0.621	0.641
TiO_2-BNNT-PAN-PMMA	1:6:2:7	0.471	0.487	0.505	0.549

In general, values of t_{Li+} approaching unity are desirable to assure gradient homogeneity across the electrolyte. However, in most of the cases, adding a filler such as BNAG or BNNT into the electrolyte system can produce an internal charge. This internal charge can create an additional polarization loss due to a possible ion exchange between the composite and the ionic liquid [150, 153, 161]. Thus transference numbers less than one are typical for composite electrolytes. For example, PAN/PMMA based ionic gel systems have transference numbers on the order of 0.5-0.7 [153, 161]. As shown in Table 1, t_{Li}^{+} for our electrolytes, without filler, with BNAG filler, and with BNNT filler, are 0.65, 0.48 and 0.39 at room temperature, respectively. Importantly, we find that the ion transference number increases with increasing temperatures (respective values become 0.77, 0.59, and 0.50 at 100^{o}C). Furthermore, t_{Li}^{+} for the BNAG and BNNT containing electrolytes is increased by 20% by adding a small amount of TiO2 nanoparticles, yielding 0.58 for TiO_2/BNAG addition and 0.47 for TiO_2/BNNT addition at room temperature, and 0.64 and 0.55 at 100^{o}C, respectively. These t_{Li+} values are quite acceptable.

We also investigate the thermal stability of the different electrolyte compositions by solution impedance and ionic conductivity measurements at different temperatures. Fig. 4.1a shows the ac impedance of the electrolytes as a function of temperature. Sharp increases are observed at 120^{o}C for unfilled PAN-PMMA, and at 145^{o}C and 190^{o}C for electrolytes filled with BNNTs and BNAG, respectively. Addition of TiO_2 has only a minor effect on the impedance thresholds for the BNNT and BNAG samples. The rapid increase in impedance signals failure of the electrolyte complex in blocking active ionic transport. Thereafter the impedance grows quickly with increasing temperatures, which causes severe pressure build up in the cells due to gas generation. This causes the electrolyte complex to fail entirely and short circuit the cell internally, whereupon the impedance drops precipitously.

The improvements in thermal stability for the BNNT and BNAG fillers, suggested by the impedance threshold data of Fig. 4.1a, are even more dramatic than the figure implies. In particular, the electrolyte must withstand repeated cycling. At 120^{o}C, we find that unfilled PAN-PMMA is prone to failure after only a few cycles, whereas the BNNT and BNAG filled cells show stable behavior over at least 500 cycles at 145 ^{0}C and 190 ^{0}C, respectively (Supplementary Fig.C-S1; in Appendix-C).

Fig. 4.1b shows the relationship of ionic conductivity of the electrolyte with respect to temperature. As expected, the electrolyte with only PAN/PMMA has the highest ionic conductivity, but the electrolyte composites with BNAG and BNNTs also exhibit good conductivity.

The reason the cells with BNAG have higher performance than the cells with BNNTs is the ability of BNAG to absorb more of the ionic solution due to its higher specific surface area. Adding TiO_2 nanoparticles does not appreciably affect the temperature limit but does slightly increase ionic conductivity. The data of Fig. 4.1 clearly indicate that polymer reinforcements with BNAG and BNNTs increase the strength and structural integrity of the polymer. With these fillers, the polymer can survive elevated temperatures and elevated internal pressures.

The electrochemical stability and anodic decomposition of the cells is tested by measuring the current-voltage response using linear voltage sweeps at 100°C. As shown in Figure 4.2, the BNNT electrolyte complex has an anodic stability up to 5.05V vs. Li at this elevated temperature. The decomposition voltage of the BNAG electrolyte complex extends above 5.4V vs. Li, indicating additional electrolyte absorption ability of BNAG which further improves electrochemical stability of the electrolyte. The cells with TiO_2 nanoparticles show slightly more improved anodic stability. This nested electrolyte design shows good anodic stability, which makes it compatible with negative electrode systems (eg. carbon or silicon based), essential to high-voltage batteries for high energy applications.

The impedance of the cells at different temperature and cycle numbers is measured by alternating-current impedance spectroscopy (Figure 4.3). With this method, we directly probe the interface between the electrode and the polymer electrolyte. The resistances can be broken down into three regimes: data at high frequencies are related to ionic conductivity, at medium frequencies to the charge transfer between electrodes, and at lower frequencies to diffusion of lithium ions in the cathode [162, 163].

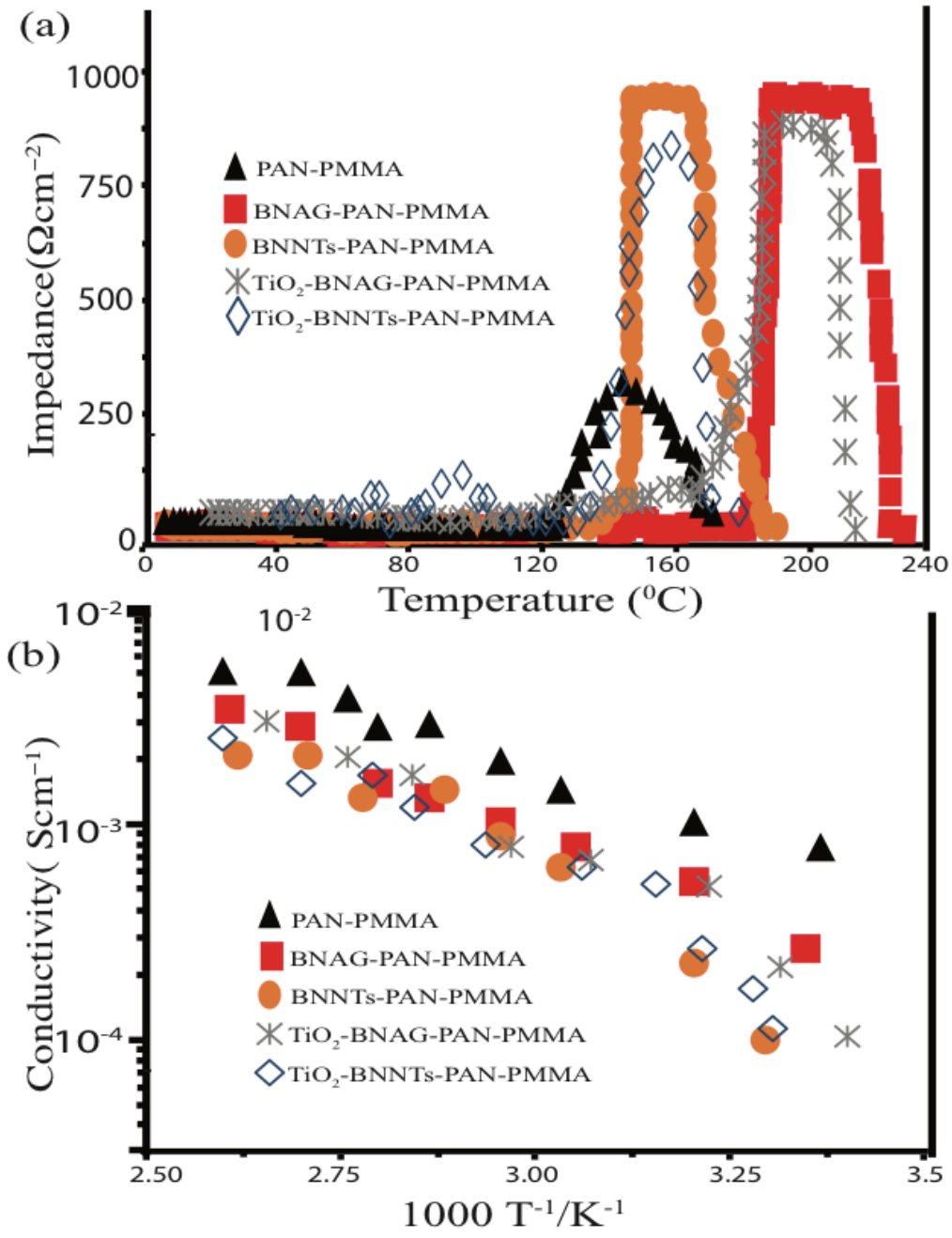

Figure 4.1 Electrical response characteristics of HTEC cells: a. Impedance of Li-ion cells with different electrolyte complexes. b. Temperature dependence of ionic conductivity of different electrolyte matrices.

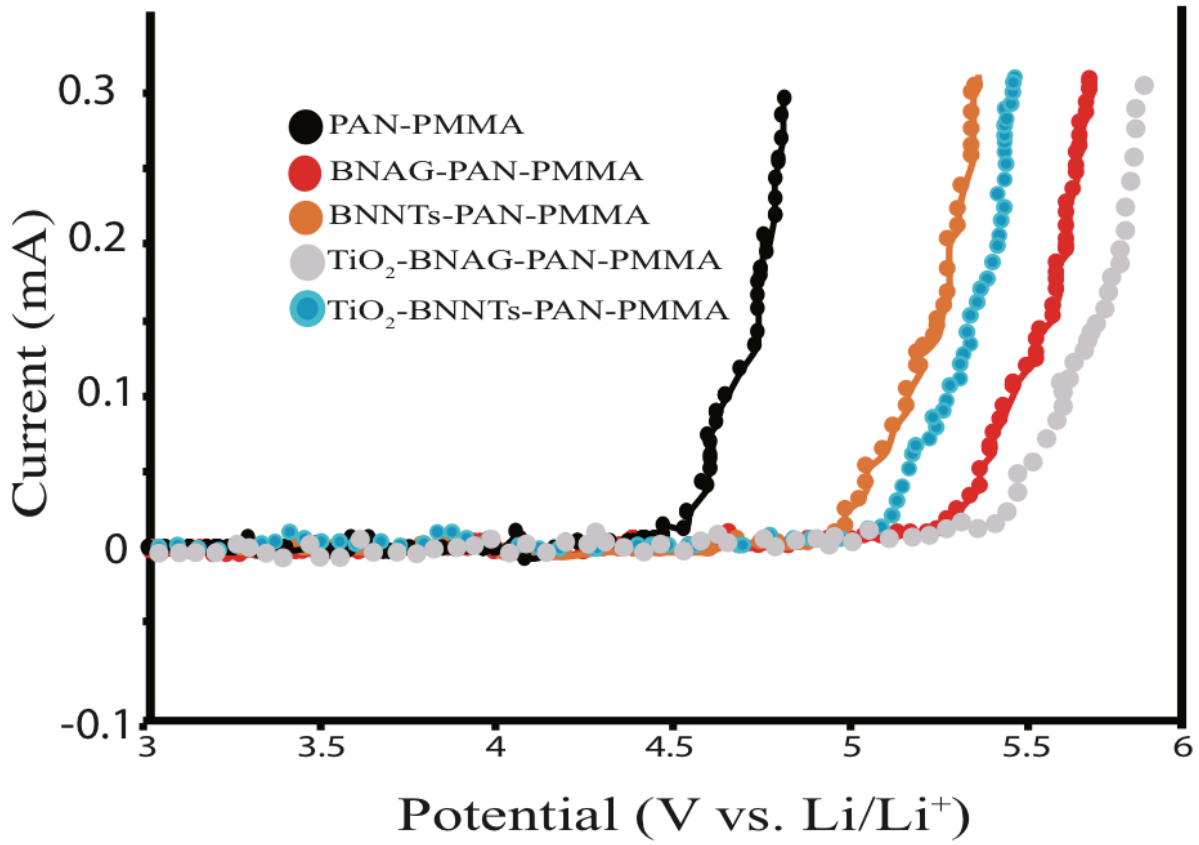

Figure 4.2 Current voltage response of different electrolyte complexes at 100^{o}C with a scan of 1mVs^{-1}.

When temperature increases, data become more intertwined and indistinguishable because of higher chemical reactivity. The thermal energy flowing in the cell provides more kinetic energy to the ions which causes the ions, at interfaces, to begin to move much faster toward the electrodes. Thus, ionic conductivity increases, diffusion processes become predominant, and the impedance decreases. Cells with BNNTs exhibit higher impedance at elevated temperatures than cells containing BNAG, which indicates that ionic diffusion is more efficient through the BNAG electrolyte complex.

In order to establish overall cell performance characteristics, we determine the variation of impedance with the cycle number (Fig. 4.3c and 4.3d). As cycle number increases the data at the middle frequency region increases due to capacity fading. The porosity of the cathode slowly decreases due to accumulation of residual reactants at the interface. The cells with BNAG and BNNTs have similar characteristics throughout the first 20 cycles. However, at later cycles the cells with BNAG modification exhibit lower resistance and have better overall charge-transfer than cells with BNNTs, which indicates the BNAG electrolyte complex has better interface stability which improves electrolyte retention characteristics. The cells with no fillers exhibit a similar trace at the first two cycles but then show a marked increase in resistance (Supplementary Fig.C-S2; in Appendix-C). The cells with TiO_2 nanoparticles exhibit better behavior at the middle frequency region, as expected, but poor characteristics in the low frequency region due to poor interstitial diffusion (Supplementary Fig.C-S3; in Appendix-C).

Figures 4.4a and 4.4b show cyclic voltammograms of cells with BNAG and BNNTs modifications at different temperatures, while Fig. 4.4c, capacity vs cycle number, provides a clear indication of the importance of polymer reinforcement on cell performance. The symmetrical feature in the voltammograms corresponds to lithium insertion and extraction [162-164]. The smooth and highly symmetric peaks indicate that the lithium insertion and extraction are reversible and no other reaction is involved during these processes. Increasing temperature results in an enhanced peak current and peak separation. The energy is also shifted due to the stronger diffusion process by 30mV and 40mV for BNNTs and BNAG, respectively. This behavior results in inequality of anodic and cathodic current behavior. But, as seen in Fig. 4, cells are very stable even at high temperatures. These cells are very stable over 500 cycles at elevated temperatures (145^0C and 190^0C for BNNTs and BNAG, respectively), while the cells with no filler decline steadily after 5 cycles (Fig. 4.4c and Supplementary Fig.C-S1; in Appendix-C). The cells with TiO_2 yield better capacity at room temperature up to 100 cycles, but at elevated temperatures the cells suffer severe capacity degradation after the first 20 cycles (Supplementary Fig.C-S4; in Appendix-C). The battery power loss at elevated temperatures could be due to the parasitic reactions among the solvents and TiO_2 interface.

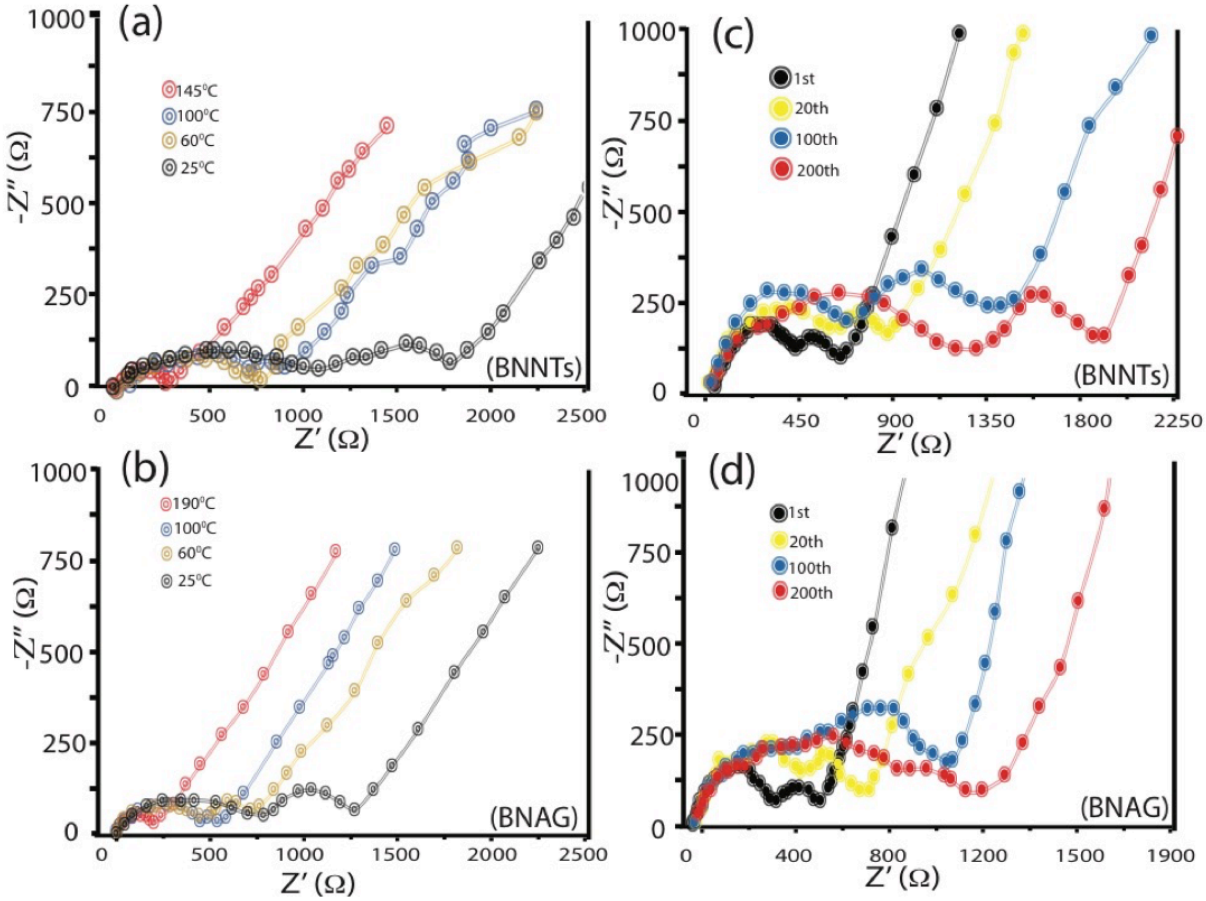

Figure 4.3 Impedance spectra of the Li-ion cells. The impedance of the cells at different temperatures; a. the cells with BNNTs modification and b. the cells with BNAG modification. The impedance of the cells with different cycle numbers; c. the cells with BNNTs modification and d. the cells with BNAG modification.

4.1.2 Experimental: Fabrication and characterization

4.1.2.1 Electrolyte and Electrode Preparation

The lithium titanate ($Li_4Ti_5O_{12}$), spinel nanopowder, (<200nm particle size (BET)) >99%, Sigma Aldrich) anode was prepared by casting a slurry of 80wt% active material, 15wt % conductive reagent (acetylene black), and 5wt% poly-vinylidene difluoride (PVDF) binder on to aluminum (Al) foil. Lithium-rich manganese oxide ($LiMnO_4$) powder was mixed with acetylene black and PVDF at a rate of 85:10:5 (wt%) and coated on Al foil. Then the electrodes dried at 100^0C in vacuum overnight. The loading ratio between the anode and cathode was ~2:5 by weight. PAN/PMMA electrolyte was prepared by polymer solution casting method by reinforcing with BNNTs or BNAG at a rate 1:2:9 (wt%). This mixture then activated with 1M ionic liquid PYR_{14}-TFSI-LiTFSI. This electrolyte mixture was then deposited onto the electrode surface as an individual solid layer by thickness of 150-250µm.

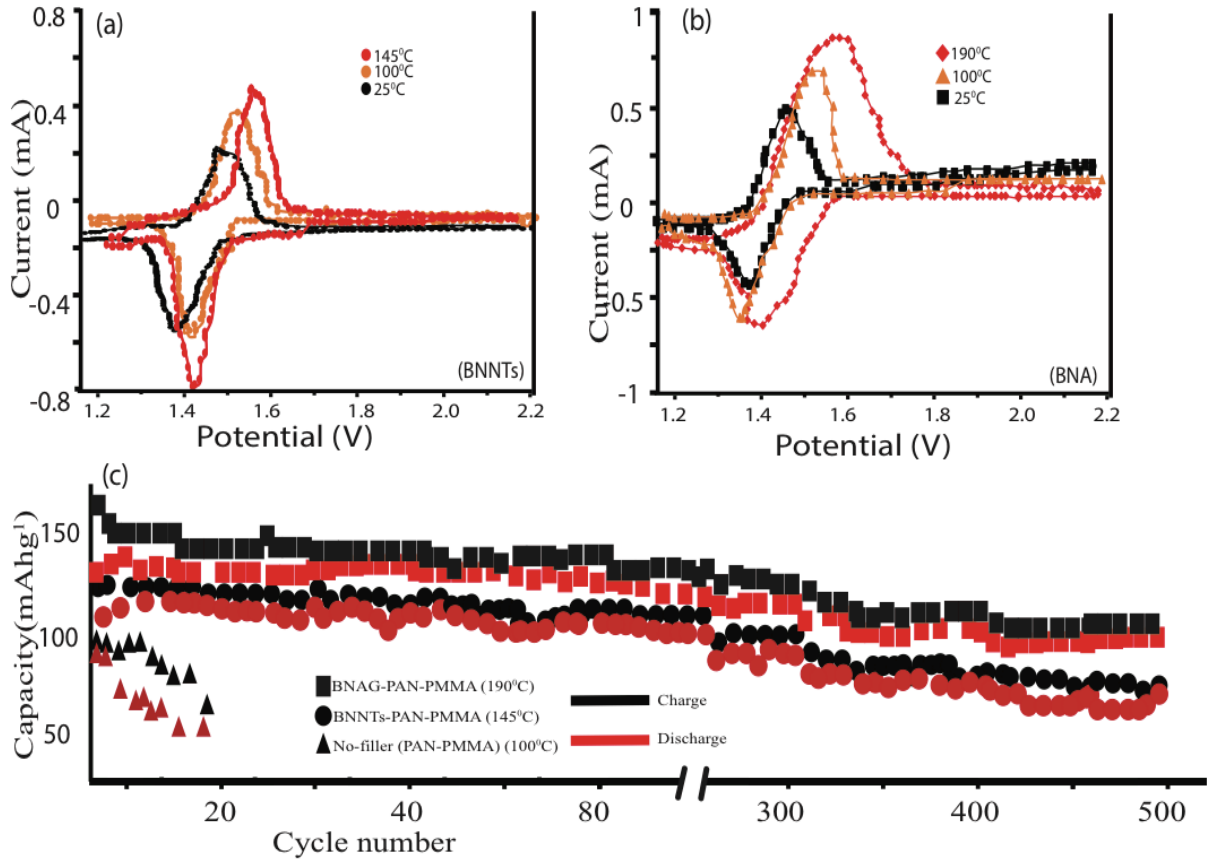

Figure 4.4 Cyclic voltammograms of Li-ion half cells with Li4Ti5O12 at different temperatures: a. the cells with BNNTs, and b. the cells with BNAG modifications. c. Performance of HTEC cells with and without BNAG and BNNTs modifications. These cells are studied at extremely elevated temperatures for a Li-ion battery. We tested the cells at 190°C, 145°C, and 100°C for BNAG, BNNTs, and no filler, respectively. Performance of HTEC cells with TiO_2 can be seen in Supplementary Fig. A-S4 in Appendix-C.

4.1.2.2 Electrochemical Characterization

The lithium transference number was measured in lithium symmetric cells (Li/electrolyte/Li) at room temperature with a dc polarization method as described in reference *19, 20, 21*. The electro chemical impedance spectroscopy, cyclic voltammetry, galvanostatic charge discharge analysis and the ionic conductivity of the cells were taken using computer controlled Gamry Reference 600 potentiostat–galvanostat and Gamry impedance analyzer at the frequency range from 0.1Hz-1000kHz.

4.1.3 Conclusion and Future Work

In conclusion, we have successfully developed explosion-resistant Li-ion battery cells that can operate at high temperatures with a long cycle lifetime. We prepare electrolyte complexes by embedding polymer electrolytes with BNAG or, with slightly less efficacy, BNNTs. The cells with the BNAG modification display good electrolyte wettability with excellent ionic conductivity and transference numbers. These modifications also improve overall thermal protection of the battery cells. The cells with BNAG modification can operate at 190^0C with over 500 cycles (and no sign of failure to at least 200^0C), while BNNTs extend safe and reliable full cyclability operation up to 145^0C. It is demonstrated that BNNT and BNAG modifications enable high voltage, high performance Li-ion batteries with outstanding performance and attractive safety features towards explosion proof batteries.

4.2 Li-air, rechargeable, solid-state batteries using graphene and boron nitride aerogel matrices

Li-air batteries have recently received substantial research interest in battery technologies due to their high theoretical energy densities. These energy densities are often compared with gasoline and are almost 5-10 times higher than commercial Li-ion batteries [165-169]. Because of this exceptional energy storage potential, Li-air battery cells are considered an ideal candidate for next-generation energy-storage systems. Therefore, various device architectures have been studied experimentally and notable improvements in performance including capacity have been achieved [165-174]. However, these cells display many serious problems including electrode decomposition, limited cycle life time, polarization losses, and air sensitivity [168, 170-179]. Moreover, a high throughput air-breathing cathode is required to enable efficient oxygen supply while keeping out other environmental contaminations (e.g., CO_2 and H_2O).

4.2.1 Result and Discussion

Here we demonstrate high performance rechargeable Li-air battery architectures using unique aerogel matrices. We used a graphene aerogel (GA) as a conducting air breathing cathode and a boron nitride aerogel (BNA) as a separator to increase cycling stability of Li metal anode. We fabricated cylindrical core shell battery cells with and without nitrogen doped graphene aerogel (N-GA). This design enables efficient air throughput and allows centrifugal rotation that leads to easier electrolyte penetration into the carbon matrices due to a centripetal force gradient. Thus, the reaction area is greatly increased, allowing for high capacity utilization. We also studied two different catalysts (LiI and LiF) and their interaction with these aerogel matrices.

The aerogel matrices provide high surface area and porosity for efficient catalysis while improving the charge transfer between electrodes. Therefore, these battery cells exhibit high electrochemical performances, up to 200 to 300 cycle in air with a capacity of 5120mAg^{-1}.

Figure 4.5a shows a schematic illustration of the Li-air battery architecture. The cells are fabricated as follows: Graphene aerogel membrane is prepared as an open cylinder configuration. The inner surface of the open cylinder is coated with BNA and filled with tetra ethyleneglycol dimethylether (TEGDME) based gel polymer electrolyte. Then, the cell is spun at 6000 rpm for 5 minutes. The centripetal force allows the gel to penetrate further into the carbon matrix, which significantly increases the reaction area and provides a larger capacity for the electrolyte system. Subsequently, the lithium metal anode is placed along the central axis at the core of the cylinder and finally metal contacts are deposited on the cathode and anode to complete the device. A cross sectional scanning electron microscope (SEM) of the device is shown in Fig. 4.5b.

Fig. 4.6 shows the discharge-charge profiles of different Li-air battery designs at current densities of 2000mAg^{-1}. The discharge capacity of the Li-air cell with nitrogen doped graphene aerogel matrices (N-GA), LiF catalyst, and BNA coating is reached at 5120mAg^{-1} with a cycle life over 200 in air. The N-GA cells with LiI catalyst and BNA coating maintains a stable cycling [180] for more than 300 cycles, however their capacity is 3930mAg^{-1}. We also observed that the capacity rapidly fades in the cells without catalyst due to the possible accumulation of discharge products in the porous cathode. The catalyst helps to further decompose the by-products in the porous air cathode which helps the charge-discharge capacities of the electrode [181].

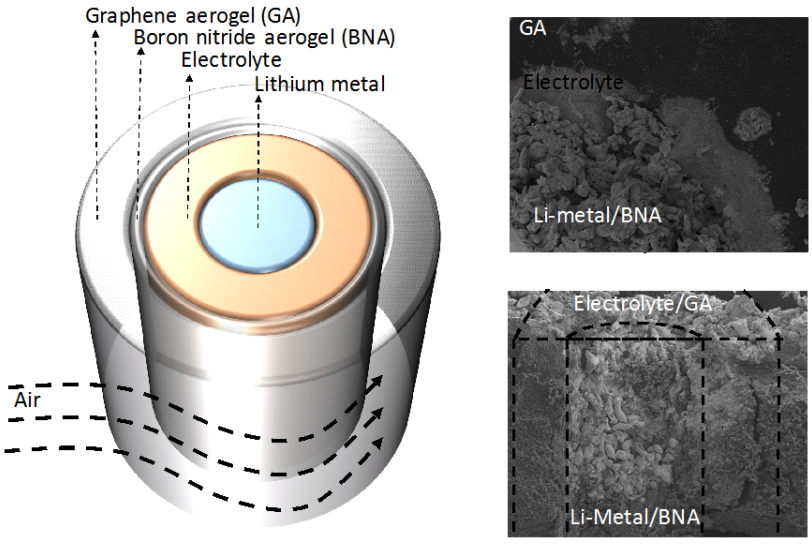

Figure 4.5 a. Schematic illustration of cylindrical core shell Li-air battery cell. b. Top-view SEM image and c. cross sectional SEM image of battery cell.

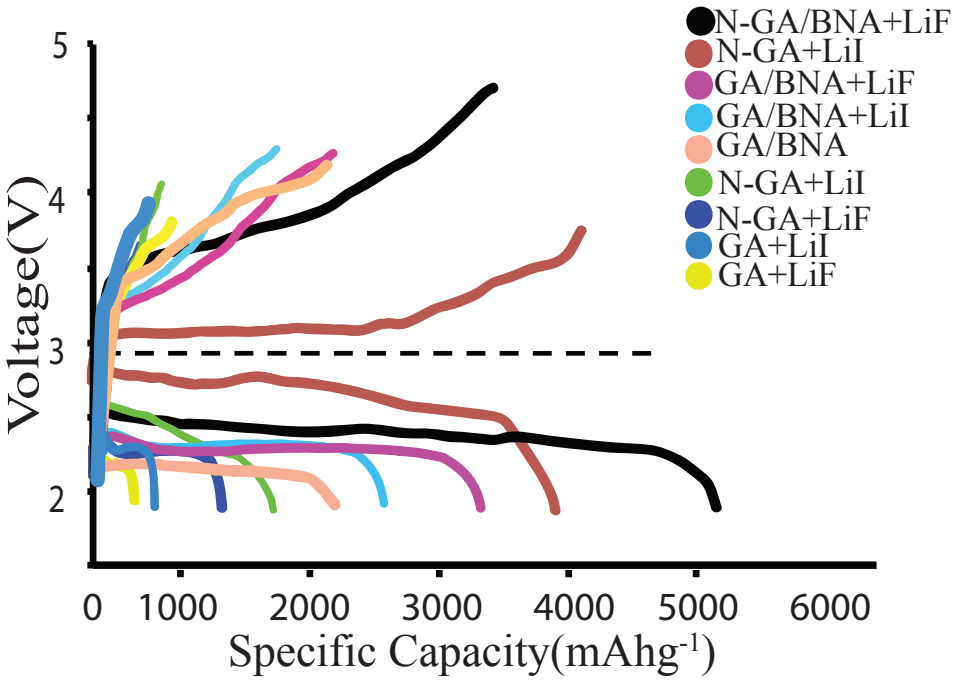

Figure 4.6 Discharge-charge profiles of the Li-air batteries with different cathode architectures at the current density of 2000mAg^{-1} in air

Fig.4.7a shows the cycle life performance of different cell designs. Certain architectural designs demonstrate enhanced capacities and cycle life times. Nitrogen doped GA cathodes with BNA coatings show significantly better performance and stability than other device architectures. Nitrogen doping helps to improve the electrochemical performance, especially oxygen reduction reaction (ORR) activity, while enhancing corrosion resistance and conductivity [165, 182, 183]. N-GA/BNA cells with LiF catalyst deliver the best performance, but lower cycling life time than the N-GA/BNA with LiI cell. This highlights the catalyst's important role in determining device performance. Moreover, the cells without BNA have a much lower capacity than the cells with BNA.

Fig. 4.7b shows energy efficiency versus cycle number of Li-air battery cells. The energy efficiency of the N-GA/BNA electrode with LiF catalyst is 82.1%, significantly higher than any other electrode architecture. The cells with N-GA, LiF, and BNA coatings deliver a discharge capacity of above 5000mAg^{-1} in air. However, the N-GA cells with LiI catalyst provides the best cycling performance; a capacity of ~4000mAg^{-1} up to 300 cycles. Fig. 3 clearly reveals nitrogen doping as a key player in maximizing capacity with BNA coating. Using the right catalyst is also crucial to improve cycling life.

Fig. 4.8 shows the Raman spectrum of different cathode architectures, N-GA/BNA and GA/BNA. GA, N-GA, and BNA Raman spectrums are also included for reference. This Raman study gives us further details regarding the discharge products. The strong D and G peaks are observed at around 1350 and 1600cm^{-1} at the graphene aerogel and a Raman peak of 1366cm^{-1} at BNA. No typical Li_2O_2 and Li_2O peaks are observed for both N-GA/BNA and GA/BNA cathodes, while Li_2CO_3 peak at 1090nm is observed only with the GA/BNA electrode. The I_D/I_G band intensity ratio is also improved with nitrogen doped graphene aerogels, while D peak is

broadened due to the intermediate product of the BNA and GA combination. Fig. 4.8 clearly indicates the quantity of lithium oxide is negligible for these electrode matrices. Thus, the capacity loss due to formation of lithium oxide passivation layer is imperceptible.

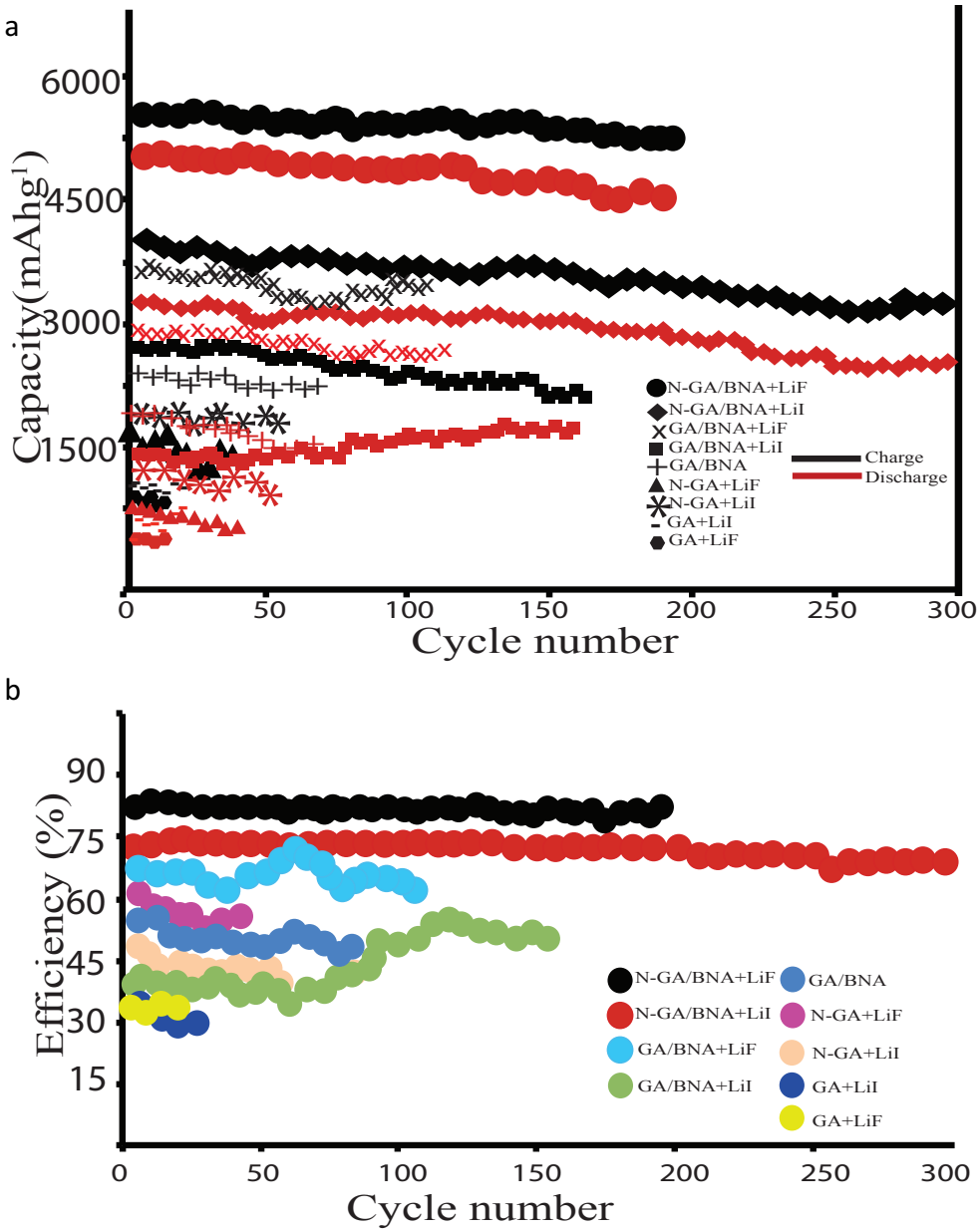

Figure 4.7 Electro chemical profile of Li-air a. cyclability, b. efficiency vs cycle number of different electrode architectures with LiI and LiF catalysis.

4.2.2 Conclusion and Future Work

In summary, high performance rechargeable Li-air batteries are prepared with different aerogel cathode architectures and different catalyst materials. Graphene aerogel is chosen as an air breathing cathode which provides a high surface area for effective electrochemical reaction and porosity for additional transport paths to deliver charge faster. These air cathodes are very light and have controllable thickness which gives them a great advantage over charge balance between electrodes and helps reduce the total mass of the battery cells. GA cathodes are also modified with nitrogen doping and BNA coating. Devices without nitrogen doping and BNA coating exhibit low performance and a poor cycling life. This reveals nitrogen doping and BNA modifications as playing a key role in high performance. Nitrogen doping provides enhanced discharge capacity and more stable GA structure while facilitating higher electro-catalytic activity. BNA coating helps maintain the anode stability and prevent possible shortage in the cell. The effect of different catalysts also plays an important role in determining device performance. The cells with LiF catalyst exhibit higher capacity and columbic efficiency while the cells with LiI catalyst have better cycling performance. The combination of nitrogen doping and BNA coating on GA with the right catalyst cathode produces Li-air cells with a long cycle life, thermal stability, and high rechargeable characteristics.

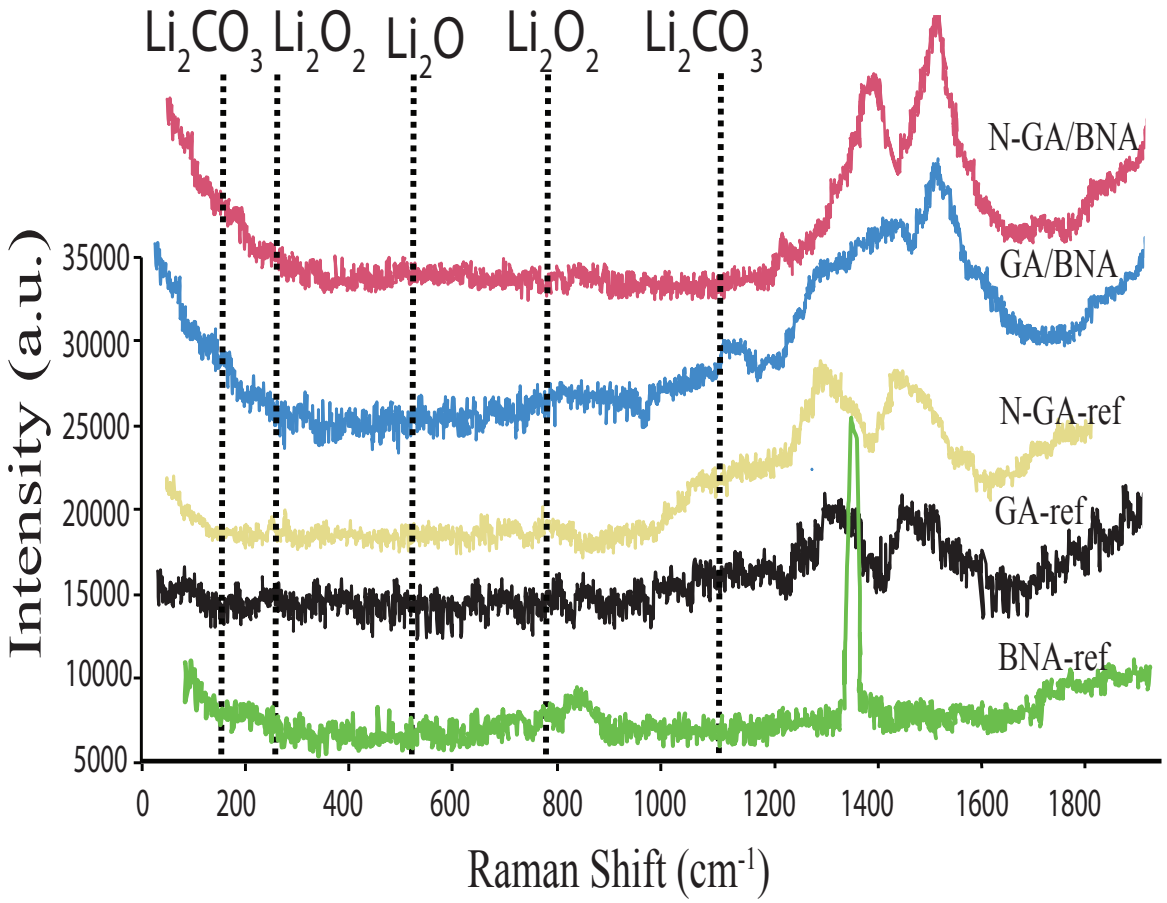

Figure 4.8 Raman spectra of discharged BNA coated graphene aerogel, with and without nitrogen doping. N-GA, GA, and BNA are also included as a reference.

Bibliography

1. Park, N.-G., *High Efficiency Mesoscopic Organometal Halide Perovskite Solar Cells.* 2016.
2. Xu, M., et al., *Graphene-Like Two-Dimensional Materials.* Chemical Reviews, 2013. **113**(5): p. 3766-3798.
3. Novoselov, K.S., et al., *Two-dimensional gas of massless Dirac fermions in graphene.* Nature, 2005. **438**(7065): p. 197-200.
4. Mas-Balleste, R., et al., *2D materials: to graphene and beyond.* Nanoscale, 2011. **3**(1): p. 20-30.
5. Mak, K.F., et al., *Atomically thin MoS 2: a new direct-gap semiconductor.* Physical review letters, 2010. **105**(13): p. 136805.
6. Liu, H., et al., *Phosphorene: An Unexplored 2D Semiconductor with a High Hole Mobility.* ACS Nano, 2014. **8**(4): p. 4033-4041.
7. Lin, Z., et al., *2D materials advances: from large scale synthesis and controlled heterostructures to improved characterization techniques, defects and applications.* 2D Materials, 2016. **3**(4): p. 042001.
8. F. Bassani and G. Pastori Parravicini, *Electronic States and Optical Transitions in Solids* 1975, New York: Pergamon press.
9. Reinhart, F. and R. Logan, *Interface stress of Al x Ga1− x As–GaAs layer structures.* Journal of Applied Physics, 1973. **44**(7): p. 3171-3175.
10. Ploog, K., M. Hauser, and A. Fischer, *Fundamental studies and device application of δ-doping in GaAs Layers and in AlxGa1− xAs/GaAs heterostructures.* Applied Physics A, 1988. **45**(3): p. 233-244.
11. Novoselov, K.S., et al., *Electric field effect in atomically thin carbon films.* science, 2004. **306**(5696): p. 666-669.
12. Novoselov, K.S. and A. Geim, *The rise of graphene.* Nat. Mater, 2007. **6**: p. 183-191.
13. Novoselov, K., et al., *Two-dimensional atomic crystals.* Proceedings of the National Academy of Sciences of the United States of America, 2005. **102**(30): p. 10451-10453.
14. Geim, A.K., *Graphene: status and prospects.* science, 2009. **324**(5934): p. 1530-1534.
15. Zhang, Y., et al., *Experimental observation of quantum Hall effect and Berry's phase in graphene.* arXiv preprint cond-mat/0509355, 2005.
16. Wu, Z.S., et al., *Field emission of single-layer graphene films prepared by electrophoretic deposition.* Advanced Materials, 2009. **21**(17): p. 1756-1760.
17. Wang, X., L. Zhi, and K. Müllen, *Transparent, conductive graphene electrodes for dye-sensitized solar cells.* Nano letters, 2008. **8**(1): p. 323-327.
18. Wang, D.-W., et al., *Fabrication of graphene/polyaniline composite paper via in situ anodic electropolymerization for high-performance flexible electrode.* ACS nano, 2009. **3**(7): p. 1745-1752.
19. Bolotin, K.I., et al., *Ultrahigh electron mobility in suspended graphene.* Solid State Communications, 2008. **146**(9): p. 351-355.

20. Song, L., et al., *Large scale growth and characterization of atomic hexagonal boron nitride layers.* Nano letters, 2010. **10**(8): p. 3209-3215.
21. Ooi, N., et al., *Structural properties of hexagonal boron nitride.* Modelling and Simulation in Materials Science and Engineering, 2006. **14**(3): p. 515.
22. Lipp, A., K.A. Schwetz, and K. Hunold, *Hexagonal boron nitride: fabrication, properties and applications.* Journal of the European Ceramic Society, 1989. **5**(1): p. 3-9.
23. Novoselov, K.S., et al., *Two-dimensional gas of massless Dirac fermions in graphene.* arXiv preprint cond-mat/0509330, 2005.
24. Geim, A.K. and K.S. Novoselov, *The rise of graphene.* Nature materials, 2007. **6**(3): p. 183-191.
25. Wallace, P.R., *The band theory of graphite.* Physical Review, 1947. **71**(9): p. 622.
26. Neto, A.C., et al., *The electronic properties of graphene.* Reviews of modern physics, 2009. **81**(1): p. 109.
27. Abanin, D., et al., *Fractional quantum Hall effect in suspended graphene: transport coefficients and electron interaction strength.* Physical Review B, 2010. **81**(11): p. 115410.
28. Wang, L., et al., *One-dimensional electrical contact to a two-dimensional material.* Science, 2013. **342**(6158): p. 614-617.
29. Mak, K.F., et al., *Measurement of the optical conductivity of graphene.* Physical review letters, 2008. **101**(19): p. 196405.
30. Du, X., et al., *Approaching ballistic transport in suspended graphene.* Nature nanotechnology, 2008. **3**(8): p. 491-495.
31. Lee, C., et al., *Measurement of the elastic properties and intrinsic strength of monolayer graphene.* science, 2008. **321**(5887): p. 385-388.
32. Zhao, H., K. Min, and N. Aluru, *Size and chirality dependent elastic properties of graphene nanoribbons under uniaxial tension.* Nano letters, 2009. **9**(8): p. 3012-3015.
33. Zhu, Y., et al., *Graphene and graphene oxide: synthesis, properties, and applications.* Advanced materials, 2010. **22**(35): p. 3906-3924.
34. Si, W., et al., *Selective sensing of catechol and hydroquinone based on poly (3, 4-ethylenedioxythiophene)/nitrogen-doped graphene composites.* Sensors and Actuators B: Chemical, 2014. **199**: p. 154-160.
35. Panchal, V., et al., *Visualisation of edge effects in side-gated graphene nanodevices.* Scientific reports, 2014. **4**.
36. Pan, S., et al., *Enhanced electrochemical sensing of nitroaromatic compounds based on hydroxyl modified carbon submicroparticles.* Electrochimica Acta, 2016. **203**: p. 301-308.
37. Kim, J., et al., *Electrical control of optical plasmon resonance with graphene.* Nano letters, 2012. **12**(11): p. 5598-5602.
38. Das, D., et al. *Finding out the optimal boron concentration in BCx sheets for high capacity anode material in Li-ion batteries*. in *APS Meeting Abstracts*. 2016.
39. Bae, S., et al., *Roll-to-roll production of 30-inch graphene films for transparent electrodes.* Nature nanotechnology, 2010. **5**(8): p. 574-578.
40. Zhang, Y., et al., *Hexagonal boron nitride cover on Pt (111): a new route to tune molecule–metal interaction and metal-catalyzed reactions.* Nano letters, 2015. **15**(5): p. 3616-3623.

41. Tian, Y., et al., *Theoretical study of the adsorption of CHO radicals on hexagonal boron nitride sheet: Structural and electronic changes.* Applied Surface Science, 2014. **295**: p. 137-143.
42. Ponce-Pérez, R., G.H. Cocoletzi, and N. Takeuchi, *Two-dimensional boron nitride structures functionalization: first principles studies.* Journal of molecular modeling, 2016. **22**(9): p. 226.
43. Fathalizadeh, A., et al., *Scaled synthesis of boron nitride nanotubes, nanoribbons, and nanococoons using direct feedstock injection into an extended-pressure, inductively-coupled thermal plasma.* Nano letters, 2014. **14**(8): p. 4881-4886.
44. Zhang, J., Y. Yang, and J. Lou, *Investigation of hexagonal boron nitride as an atomically thin corrosion passivation coating in aqueous solution.* Nanotechnology, 2016. **27**(36): p. 364004.
45. Rousseas, M., et al., *Synthesis of highly crystalline sp2-bonded boron nitride aerogels.* ACS nano, 2013. **7**(10): p. 8540-8546.
46. Pekala, R., et al., *Carbon aerogels for electrochemical applications.* Journal of non-crystalline solids, 1998. **225**: p. 74-80.
47. Pekala, R., *Organic aerogels from the polycondensation of resorcinol with formaldehyde.* Journal of materials science, 1989. **24**(9): p. 3221-3227.
48. Nardecchia, S., et al., *Three dimensional macroporous architectures and aerogels built of carbon nanotubes and/or graphene: synthesis and applications.* Chemical Society Reviews, 2013. **42**(2): p. 794-830.
49. Wang, L., et al., *Capacitive deionization of NaCl solutions using carbon nanotube sponge electrodes.* Journal of Materials Chemistry, 2011. **21**(45): p. 18295-18299.
50. Meng, F., et al., *Alkali-treated graphene oxide as a solid base catalyst: synthesis and electrochemical capacitance of graphene/carbon composite aerogels.* Journal of Materials Chemistry, 2011. **21**(46): p. 18537-18539.
51. Hrubesh, L.W., *Aerogel applications.* Journal of Non-Crystalline Solids, 1998. **225**: p. 335-342.
52. Biener, J., et al., *Advanced carbon aerogels for energy applications.* Energy & Environmental Science, 2011. **4**(3): p. 656-667.
53. Zhao, Y., et al., *A versatile, ultralight, nitrogen-doped graphene framework.* Angewandte Chemie, 2012. **124**(45): p. 11533-11537.
54. Yin, S., Z. Niu, and X. Chen, *Assembly of graphene sheets into 3D macroscopic structures.* Small, 2012. **8**(16): p. 2458-2463.
55. Yao, B., et al., *Base-Induced Liquid Crystals of Graphene Oxide for Preparing Elastic Graphene Foams with Long-Range Ordered Microstructures.* Advanced Materials, 2016. **28**(8): p. 1623-1629.
56. Xu, Y., et al., *Self-assembled graphene hydrogel via a one-step hydrothermal process.* ACS nano, 2010. **4**(7): p. 4324-4330.
57. Li, C. and G. Shi, *Three-dimensional graphene architectures.* Nanoscale, 2012. **4**(18): p. 5549-5563.
58. Jalili, R., et al., *Organic solvent-based graphene oxide liquid crystals: a facile route toward the next generation of self-assembled layer-by-layer multifunctional 3D architectures.* Acs Nano, 2013. **7**(5): p. 3981-3990.

59. Cong, H., et al., *ACS Nano, 2012, 6, 2693–2703.* CrossRef| CAS| Web of Science® Times Cited. **114**.
60. Chen, Z., et al., *Three-dimensional flexible and conductive interconnected graphene networks grown by chemical vapour deposition.* Nature materials, 2011. **10**(6): p. 424.
61. Chen, W. and L. Yan, *In situ self-assembly of mild chemical reduction graphene for three-dimensional architectures.* Nanoscale, 2011. **3**(8): p. 3132-3137.
62. Chen, W., et al., *Self-assembly and embedding of nanoparticles by in situ reduced graphene for preparation of a 3d graphene/nanoparticle aerogel.* Advanced materials, 2011. **23**(47): p. 5679-5683.
63. Worsley, M.A., et al., *Synthesis of graphene aerogel with high electrical conductivity.* Journal of the American Chemical Society, 2010. **132**(40): p. 14067-14069.
64. Zhang, X., et al., *Mechanically strong and highly conductive graphene aerogel and its use as electrodes for electrochemical power sources.* journal of materials chemistry, 2011. **21**(18): p. 6494-6497.
65. Zhou, H., et al., *Graphene/poly (3, 4-ethylenedioxythiophene) hydrogel with excellent mechanical performance and high conductivity.* Carbon, 2013. **59**: p. 495-502.
66. Huang, H., et al., *Edge-to-edge assembled graphene oxide aerogels with outstanding mechanical performance and superhigh chemical activity.* Small, 2013. **9**(8): p. 1397-1404.
67. Hu, H., et al., *Ultralight and highly compressible graphene aerogels.* Advanced materials, 2013. **25**(15): p. 2219-2223.
68. Pham, T., et al., *Nanoscale structure and superhydrophobicity of sp2-bonded boron nitride aerogels.* Nanoscale, 2015. **7**(23): p. 10449-10458.
69. Harley-Trochimczyk, A., et al., *Platinum Nanoparticle Loading of Boron Nitride Aerogel and Its Use as a Novel Material for Low-Power Catalytic Gas Sensing.* Advanced Functional Materials, 2016. **26**(3): p. 433-439.
70. Han, W.-Q., et al., *Activated boron nitride derived from activated carbon.* Nano Letters, 2004. **4**(1): p. 173-176.
71. Song, Y., et al., *Ultralight boron nitride aerogels via template-assisted chemical vapor deposition.* Scientific reports, 2015. **5**.
72. Turner, J.A., *A realizable renewable energy future.* Science, 1999. **285**(5428): p. 687-689.
73. IVANAJ, S., et al., *MNEs and climate change: implications for future research*. 2017, Elsevier.
74. Ellabban, O., H. Abu-Rub, and F. Blaabjerg, *Renewable energy resources: Current status, future prospects and their enabling technology.* Renewable and Sustainable Energy Reviews, 2014. **39**: p. 748-764.
75. Hosenuzzaman, M., et al., *Global prospects, progress, policies, and environmental impact of solar photovoltaic power generation.* Renewable and Sustainable Energy Reviews, 2015. **41**: p. 284-297.
76. Masuko, K., et al., *Achievement of more than 25% conversion efficiency with crystalline silicon heterojunction solar cell.* IEEE Journal of Photovoltaics, 2014. **4**(6): p. 1433-1435.

77. Woodhouse, M., et al., *On the Path to SunShot. The Role of Advancements in Solar Photovoltaic Efficiency, Reliability, and Costs*. 2016, National Renewable Energy Lab.(NREL), Golden, CO (United States).
78. Shi, D., et al., *Low trap-state density and long carrier diffusion in organolead trihalide perovskite single crystals.* Science, 2015. **347**(6221): p. 519-522.
79. Dong, Q., et al., *Electron-hole diffusion lengths> 175 μm in solution-grown CH3NH3PbI3 single crystals.* Science, 2015. **347**(6225): p. 967-970.
80. Xing, G., et al., *Long-range balanced electron-and hole-transport lengths in organic-inorganic CH3NH3PbI3.* Science, 2013. **342**(6156): p. 344-347.
81. Stranks, S.D., et al., *Electron-hole diffusion lengths exceeding 1 micrometer in an organometal trihalide perovskite absorber.* Science, 2013. **342**(6156): p. 341-344.
82. Jeon, N.J., et al., *Compositional engineering of perovskite materials for high-performance solar cells.* Nature, 2015. **517**(7535): p. 476.
83. Zhou, H., et al., *Interface engineering of highly efficient perovskite solar cells.* Science, 2014. **345**(6196): p. 542-546.
84. Saliba, M., et al., *Cesium-containing triple cation perovskite solar cells: improved stability, reproducibility and high efficiency.* Energy & environmental science, 2016. **9**(6): p. 1989-1997.
85. Green, M.A., et al., *Solar cell efficiency tables (version 46).* Progress in Photovoltaics: Research and Applications, 2015. **23**(7): p. 805-812.
86. Noel, N.K., et al., *Lead-free organic–inorganic tin halide perovskites for photovoltaic applications.* Energy & Environmental Science, 2014. **7**(9): p. 3061-3068.
87. Bi, D., et al., *Efficient luminescent solar cells based on tailored mixed-cation perovskites.* Science advances, 2016. **2**(1): p. e1501170.
88. Bailie, C.D., et al., *Semi-transparent perovskite solar cells for tandems with silicon and CIGS.* Energy & Environmental Science, 2015. **8**(3): p. 956-963.
89. Werner, J., et al., *Sputtered rear electrode with broadband transparency for perovskite solar cells.* Solar Energy Materials and Solar Cells, 2015. **141**: p. 407-413.
90. Mailoa, J.P., et al., *A 2-terminal perovskite/silicon multijunction solar cell enabled by a silicon tunnel junction.* Applied Physics Letters, 2015. **106**(12): p. 121105.
91. Löper, P., et al., *Organic–inorganic halide perovskite/crystalline silicon four-terminal tandem solar cells.* Physical Chemistry Chemical Physics, 2015. **17**(3): p. 1619-1629.
92. Jiang, F., et al., *A two-terminal perovskite/perovskite tandem solar cell.* Journal of Materials Chemistry A, 2016. **4**(4): p. 1208-1213.
93. Albrecht, S., et al., *Monolithic perovskite/silicon-heterojunction tandem solar cells processed at low temperature.* Energy & Environmental Science, 2016. **9**(1): p. 81-88.
94. Olsen, L.C., *Graded Bandgap Solar Cells*. 1989, WASHINGTON UNIV SEATTLE.
95. Dalal, V.L. and G. Baldwin, *Design and fabrication of graded bandgap solar cells in amorphous Si and alloys.* MRS Online Proceedings Library Archive, 1993. **297**.
96. Dharmadasa, I., *Advances in thin-film solar cells*. 2012: CRC Press.
97. Umari, P., E. Mosconi, and F. De Angelis, *Relativistic GW calculations on CH3NH3PbI3 and CH3NH3SnI3 perovskites for solar cell applications.* Scientific reports, 2014. **4**: p. 4467.
98. Hao, F., et al., *Lead-free solid-state organic-inorganic halide perovskite solar cells.* Nature Photonics, 2014. **8**(6): p. 489-494.

99. Stoumpos, C.C., C.D. Malliakas, and M.G. Kanatzidis, *Semiconducting tin and lead iodide perovskites with organic cations: phase transitions, high mobilities, and near-infrared photoluminescent properties.* Inorganic chemistry, 2013. **52**(15): p. 9019-9038.
100. Bernal, C. and K. Yang, *First-principles hybrid functional study of the organic–inorganic perovskites CH3NH3SnBr3 and CH3NH3SnI3.* The Journal of Physical Chemistry C, 2014. **118**(42): p. 24383-24388.
101. Takahashi, Y., et al., *Charge-transport in tin-iodide perovskite CH 3 NH 3 SnI 3: origin of high conductivity.* Dalton Transactions, 2011. **40**(20): p. 5563-5568.
102. Liang, K., D.B. Mitzi, and M.T. Prikas, *Synthesis and characterization of organic− inorganic perovskite thin films prepared using a versatile two-step dipping technique.* Chemistry of materials, 1998. **10**(1): p. 403-411.
103. Li, H., et al., *Strain sensitivity of band gaps of Sn-containing semiconductors.* Physical Review B, 2015. **91**(4): p. 045204.
104. Noh, J.H., et al., *Chemical management for colorful, efficient, and stable inorganic–organic hybrid nanostructured solar cells.* Nano letters, 2013. **13**(4): p. 1764-1769.
105. He, M., et al., *High efficiency perovskite solar cells: from complex nanostructure to planar heterojunction.* Journal of Materials Chemistry A, 2014. **2**(17): p. 5994-6003.
106. De Wolf, S., et al., *Organometallic halide perovskites: sharp optical absorption edge and its relation to photovoltaic performance.* The journal of physical chemistry letters, 2014. **5**(6): p. 1035-1039.
107. Cai, B., et al., *High performance hybrid solar cells sensitized by organolead halide perovskites.* Energy & Environmental Science, 2013. **6**(5): p. 1480-1485.
108. Hoke, E.T., et al., *Reversible photo-induced trap formation in mixed-halide hybrid perovskites for photovoltaics.* Chemical Science, 2015. **6**(1): p. 613-617.
109. Manser, J.S. and P.V. Kamat, *Band filling with free charge carriers in organometal halide perovskites.* Nature Photonics, 2014. **8**(9): p. 737-743.
110. Echendu, O., et al., *High short-circuit current density CdTe solar cells using all-electrodeposited semiconductors.* Thin Solid Films, 2014. **556**: p. 529-534.
111. McCarthy, M.A., et al., *Reorientation of the high mobility plane in pentacene-based carbon nanotube enabled vertical field effect transistors.* ACS nano, 2010. **5**(1): p. 291-298.
112. You, J., et al., *Improved air stability of perovskite solar cells via solution-processed metal oxide transport layers.* Nature nanotechnology, 2016. **11**(1): p. 75.
113. Wang, D., et al., *Stability of perovskite solar cells.* Solar Energy Materials and Solar Cells, 2016. **147**: p. 255-275.
114. Han, Y., et al., *Degradation observations of encapsulated planar CH 3 NH 3 PbI 3 perovskite solar cells at high temperatures and humidity.* Journal of Materials Chemistry A, 2015. **3**(15): p. 8139-8147.
115. Akimoto, K., et al., *Thin film deposition of Cu 2 O and application for solar cells.* Solar energy, 2006. **80**(6): p. 715-722.
116. Minami, T., Y. Nishi, and T. Miyata, *High-efficiency Cu2O-based heterojunction solar cells fabricated using a Ga2O3 thin film as n-type layer.* Applied Physics Express, 2013. **6**(4): p. 044101.
117. Lee, Y.S., et al., *Atomic Layer Deposited Gallium Oxide Buffer Layer Enables 1.2 V Open-Circuit Voltage in Cuprous Oxide Solar Cells.* Advanced Materials, 2014. **26**(27): p. 4704-4710.

118. Card, H. and E. Yang, *MIS-Schottky theory under conditions of optical carrier generation in solar cells.* Applied Physics Letters, 1976. **29**(1): p. 51-53.
119. Green, M.A. and R. Godfrey, *MIS solar cell—General theory and new experimental results for silicon.* Applied Physics Letters, 1976. **29**(9): p. 610-612.
120. Olsen, L.C., *Model calculations for metal-insulator-semiconductor solar cells.* Solid-State Electronics, 1977. **20**(9): p. 741-751.
121. Olsen, L., R. Bohara, and M. Urie, *Explanation for low-efficiency Cu2O Schottky-barrier solar cells.* Applied physics letters, 1979. **34**(1): p. 47-49.
122. Wang, E., et al. *Cuprous oxide MIS solar cells*. in *14th Photovoltaic Specialists Conference*. 1980.
123. Olsen, L., F. Addis, and W. Miller, *Experimental and theoretical studies of Cu2O solar cells.* Solar cells, 1982. **7**(3): p. 247-279.
124. Worsley, M.A., et al., *Synthesis and characterization of highly crystalline graphene aerogels.* Acs Nano, 2014. **8**(10): p. 11013-11022.
125. Rakhshani, A., *Preparation, characteristics and photovoltaic properties of cuprous oxide—a review.* Solid-State Electronics, 1986. **29**(1): p. 7-17.
126. Mittiga, A., et al., *Heterojunction solar cell with 2% efficiency based on a Cu 2 O substrate.* Applied Physics Letters, 2006. **88**(16): p. 163502.
127. Tsur, Y. and I. Riess, *Self-compensation in semiconductors.* Physical Review B, 1999. **60**(11): p. 8138.
128. Xiang, C., et al., *820 mV open-circuit voltages from Cu 2 O/CH 3 CN junctions.* Energy & Environmental Science, 2011. **4**(4): p. 1311-1318.
129. Minami, T., et al., *High-efficiency oxide solar cells with ZnO/Cu2O heterojunction fabricated on thermally oxidized Cu2O sheets.* Applied physics express, 2011. **4**(6): p. 062301.
130. Iwanowski, R. and D. Trivih, *Cu/Cu2O Schottky barrier solar cells prepared by multistep irradiation of a Cu2O substrate by H+ ions.* Solar Cells, 1985. **13**(3): p. 253-264.
131. Iwanowski, R. and D. Trivich, *The influence of hydrogen ion bombardment on the photovoltaic properties of Cu/Cu2O schottky barrier solar cells.* Radiation Effects, 1983. **76**(3): p. 87-92.
132. Briskman, R.N., *A study of electrodeposited cuprous oxide photovoltaic cells.* Solar Energy Materials and Solar Cells, 1992. **27**(4): p. 361-368.
133. Abdu, Y. and A. Musa, *Copper (I) oxide (Cu 2) based solar cells-a review.* Bayero Journal of Pure and Applied Sciences, 2009. **2**(2): p. 8-12.
134. Gibb, A.L., et al., *Atomic resolution imaging of grain boundary defects in monolayer chemical vapor deposition-grown hexagonal boron nitride.* Journal of the American Chemical Society, 2013. **135**(18): p. 6758-6761.
135. Assimos, J. and D. Trivich, *Photovoltaic properties and barrier heights of single-crystal and polycrystalline Cu2O–Cu contacts.* Journal of Applied Physics, 1973. **44**(4): p. 1687-1693.
136. Babich, I., *Raman spectrum of hexagonal boron nitride.* Theoretical and Experimental Chemistry, 1974. **8**(5): p. 594-595.
137. Trivich, D., E. Wang, and R. Komp, *Cuprous oxide photovoltaic cells. Final report, January 1, 1978-September 30, 1978*. 1978, Wayne State Univ., Detroit, MI (USA).

138. Trivich, D., et al., *Cuprous oxide photovoltaic cells*. 1978, Wayne State Univ., Detroit, MI (USA).
139. Clavaguera-Mora, M., et al., *Thermodynamic description of the Cu O system.* Journal of alloys and compounds, 2004. **377**(1): p. 8-16.
140. Biccari, F., *Defects and doping in Cu2O*. 2012: Lulu. com.
141. Poulston, S., et al., *Surface oxidation and reduction of CuO and Cu2O studied using XPS and XAES.* Surface and Interface Analysis, 1996. **24**(12): p. 811-820.
142. Ishizuka, S., et al., *Passivation of defects in polycrystalline Cu 2 O thin films by hydrogen or cyanide treatment.* Applied surface science, 2003. **216**(1): p. 94-97.
143. Okamoto, Y., et al., *Passivation of defects in nitrogen-doped polycrystalline Cu 2 O thin films by crown-ether cyanide treatment.* Applied physics letters, 2003. **82**(7): p. 1060-1062.
144. Kim, J.Y., et al., *Reduction of CuO and Cu2O with H2: H embedding and kinetic effects in the formation of suboxides.* Journal of the American Chemical Society, 2003. **125**(35): p. 10684-10692.
145. Willett, D. and S. Kuriyagawa. *The effects of sweep rate, voltage bias and light soaking on the measurement of CIS-based solar cell characteristics*. in *Photovoltaic Specialists Conference, 1993., Conference Record of the Twenty Third IEEE*. 1993. IEEE.
146. Cho, J., *Correlation between AlPO 4 nanoparticle coating thickness on LiCoO 2 cathode and thermal stability.* Electrochimica Acta, 2003. **48**(19): p. 2807-2811.
147. Bodenes, L., et al., *Lithium secondary batteries working at very high temperature: Capacity fade and understanding of aging mechanisms.* Journal of Power Sources, 2013. **236**: p. 265-275.
148. Hanisch, C., et al., *Recycling of Lithium-Ion Batteries.* Handbook of Clean Energy Systems, 2015.
149. Hu, P., et al., *Progress in nitrile-based polymer electrolytes for high performance lithium batteries.* Journal of Materials Chemistry A, 2016. **4**(26): p. 10070-10083.
150. Rodrigues, M.T.F., et al., *Hexagonal Boron Nitride-Based Electrolyte Composite for Li-Ion Battery Operation from Room Temperature to 150° C.* Advanced Energy Materials, 2016. **6**(12).
151. Song, J., Y. Wang, and C.C. Wan, *Review of gel-type polymer electrolytes for lithium-ion batteries.* Journal of Power Sources, 1999. **77**(2): p. 183-197.
152. Fasciani, C., et al., *Novel configuration of poly (vinylidenedifluoride)-based gel polymer electrolyte for application in lithium-ion batteries.* Journal of Power Sources, 2015. **294**: p. 180-186.
153. Croce, F., et al., *Nanocomposite polymer electrolytes for lithium batteries.* Nature, 1998. **394**(6692): p. 456.
154. Santhosh, P., et al., *Evaluation of a cross-linked polyurethane acrylate as polymer electrolyte for lithium batteries.* Materials research bulletin, 2006. **41**(6): p. 1023-1037.
155. Chopra, N.G., et al., *Boron nitride nanotubes.* Science, 1995. **269**(5226): p. 966.
156. Liu, F., et al., *Cheap, gram-scale fabrication of BN nanosheets via substitution reaction of graphite powders and their use for mechanical reinforcement of polymers.* Scientific reports, 2014. **4**.

157. Liu, D.-Q., X.-Q. Liu, and Z.-Z. He, *The elevated temperature performance of LiMn 2 O 4 coated with Li 4 Ti 5 O 12 for lithium ion battery.* Materials Chemistry and Physics, 2007. **105**(2): p. 362-366.
158. Bruce, P.G. and C.A. Vincent, *Steady state current flow in solid binary electrolyte cells.* Journal of electroanalytical chemistry and interfacial electrochemistry, 1987. **225**(1-2): p. 1-17.
159. Evans, J., C.A. Vincent, and P.G. Bruce, *Electrochemical measurement of transference numbers in polymer electrolytes.* Polymer, 1987. **28**(13): p. 2324-2328.
160. Koksbang, R. and E. Skou, *Transference number measurements on a hybrid polymer electrolyte.* Electrochimica acta, 1995. **40**(11): p. 1701-1706.
161. Adebahr, J., et al., *Ion transport in polymer electrolytes containing nanoparticulate TiO 2: the influence of polymer morphology.* Physical chemistry chemical physics, 2003. **5**(4): p. 720-725.
162. Ha, H.-W., N.J. Yun, and K. Kim, *Improvement of electrochemical stability of LiMn 2 O 4 by CeO 2 coating for lithium-ion batteries.* Electrochimica Acta, 2007. **52**(9): p. 3236-3241.
163. Munoz-Condes, P., et al., *On condition maintenance based on the impedance measurement for traction batteries: Development and industrial implementation.* IEEE Transactions on Industrial Electronics, 2013. **60**(7): p. 2750-2759.
164. Zhang, Y., C.-Y. Wang, and X. Tang, *Cycling degradation of an automotive LiFePO 4 lithium-ion battery.* Journal of Power Sources, 2011. **196**(3): p. 1513-1520.
165. Girishkumar, G., et al., *Lithium− air battery: promise and challenges.* The Journal of Physical Chemistry Letters, 2010. **1**(14): p. 2193-2203.
166. Christensen, J., et al., *A critical review of Li/air batteries.* Journal of the Electrochemical Society, 2011. **159**(2): p. R1-R30.
167. Kraytsberg, A. and Y. Ein-Eli, *Review on Li–air batteries—Opportunities, limitations and perspective.* Journal of Power Sources, 2011. **196**(3): p. 886-893.
168. Lim, H.D., et al., *Enhanced Power and Rechargeability of a Li− O2 Battery Based on a Hierarchical-Fibril CNT Electrode.* Advanced Materials, 2013. **25**(9): p. 1348-1352.
169. Yuan, J., J.-S. Yu, and B. Sundén, *Review on mechanisms and continuum models of multi-phase transport phenomena in porous structures of non-aqueous Li-Air batteries.* Journal of Power Sources, 2015. **278**: p. 352-369.
170. Zhang, J.-G., et al., *Ambient operation of Li/Air batteries.* Journal of Power Sources, 2010. **195**(13): p. 4332-4337.
171. Jung, H.-G., et al., *An improved high-performance lithium–air battery.* Nature chemistry, 2012. **4**(7): p. 579-585.
172. Zhang, T. and H. Zhou, *From Li–O2 to Li–air batteries: carbon nanotubes/ionic liquid gels with a tricontinuous passage of electrons, ions, and oxygen.* Angewandte Chemie, 2012. **124**(44): p. 11224-11229.
173. Thotiyl, M.M.O., et al., *A stable cathode for the aprotic Li-O2 battery.* Nature materials, 2013. **12**(11): p. 1050.
174. Suzuki, Y., et al., *Characteristics of discharge products in all-solid-state Li-air batteries.* Solid State Ionics, 2015. **278**: p. 222-227.
175. Lee, J.S., et al., *Metal–air batteries with high energy density: Li–air versus Zn–air.* Advanced Energy Materials, 2011. **1**(1): p. 34-50.

176. Lu, Y.-C., H.A. Gasteiger, and Y. Shao-Horn, *Catalytic activity trends of oxygen reduction reaction for nonaqueous Li-air batteries.* Journal of the American Chemical Society, 2011. **133**(47): p. 19048-19051.
177. Mi, R., et al., *Effects of nitrogen-doped carbon nanotubes on the discharge performance of Li-air batteries.* Carbon, 2014. **67**: p. 744-752.
178. Sun, B., et al., *Mesoporous Carbon Nanocube Architecture for High-Performance Lithium–Oxygen Batteries.* Advanced Functional Materials, 2015. **25**(28): p. 4436-4444.
179. He, M., et al., *Hierarchical porous nitrogen doped three-dimensional graphene as a free-standing cathode for rechargeable lithium-oxygen batteries.* Electrochimica Acta, 2016. **191**: p. 90-97.
180. Blase, X., et al., *Stability and band gap constancy of boron nitride nanotubes.* EPL (Europhysics Letters), 1994. **28**(5): p. 335.
181. Lim, H.D., et al., *Superior rechargeability and efficiency of lithium–oxygen batteries: hierarchical air electrode architecture combined with a soluble catalyst.* Angewandte Chemie International Edition, 2014. **53**(15): p. 3926-3931.
182. Wu, G., et al., *Nitrogen-doped graphene-rich catalysts derived from heteroatom polymers for oxygen reduction in nonaqueous lithium–O2 battery cathodes.* ACS nano, 2012. **6**(11): p. 9764-9776.
183. Yoo, E., J. Nakamura, and H. Zhou, *N-Doped graphene nanosheets for Li–air fuel cells under acidic conditions.* Energy & environmental science, 2012. **5**(5): p. 6928-6932.

Appendix A

Supplementary Information of Graded Bandgap Perovskite Solar Cells

A.1 Fabrication Steps

This section aims to further elaborate on the fabrication steps of graded bandgap perovskite solar cells and also provides "tips and tricks" for future group members. The overall simplified fabrication schematics can be seen in Fig. A1. In the next few sections, I will explain these schematics in detail.

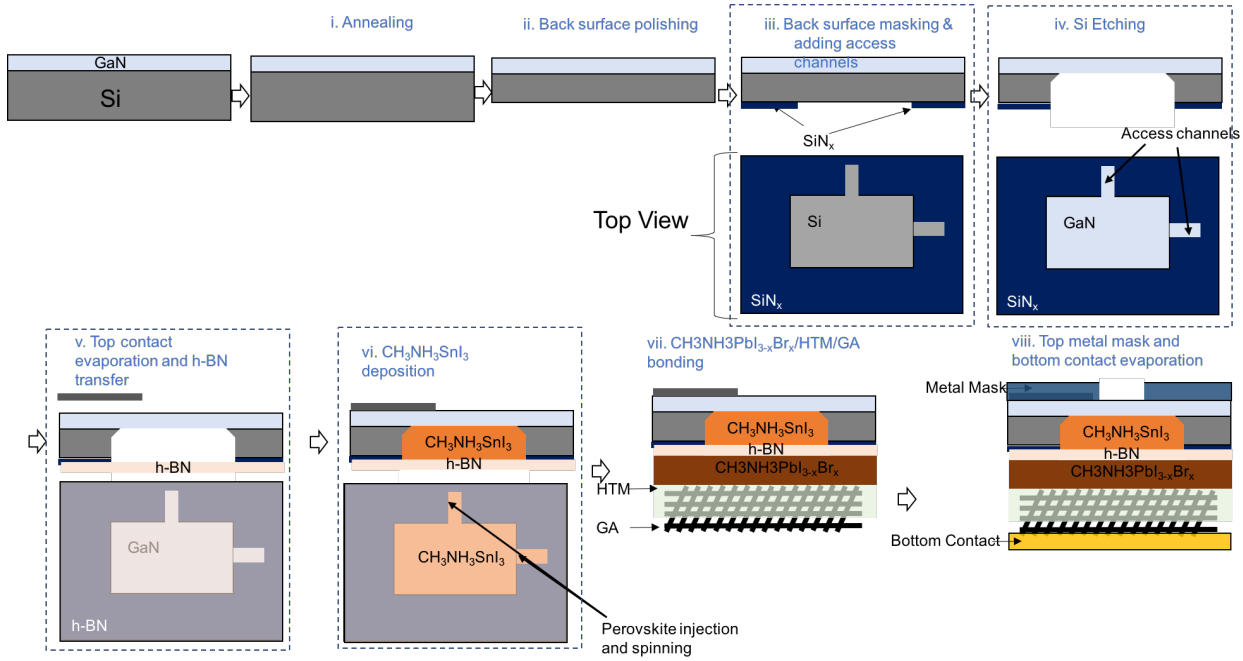

Figure A.1 Detailed fabrication process for graded band gap perovskite solar cells.

A.1.1 Annealing

As a starting substrate, we start with a commercial GaN on a silicon (Si) wafer which is ten times less expensive than GaN single crystalline substrates. However these experiments can also be carried out on single crystalline GaN substrates.

The first process for the commercial wafer is annealing. This wafer is annealed at 650^{o}C for 2 hours in an argon (Ar) environment in a regular CVD annealing chamber. The inert atmosphere is very important to ensure that no unexpected contamination or surface degradation occurs during GaN doping.

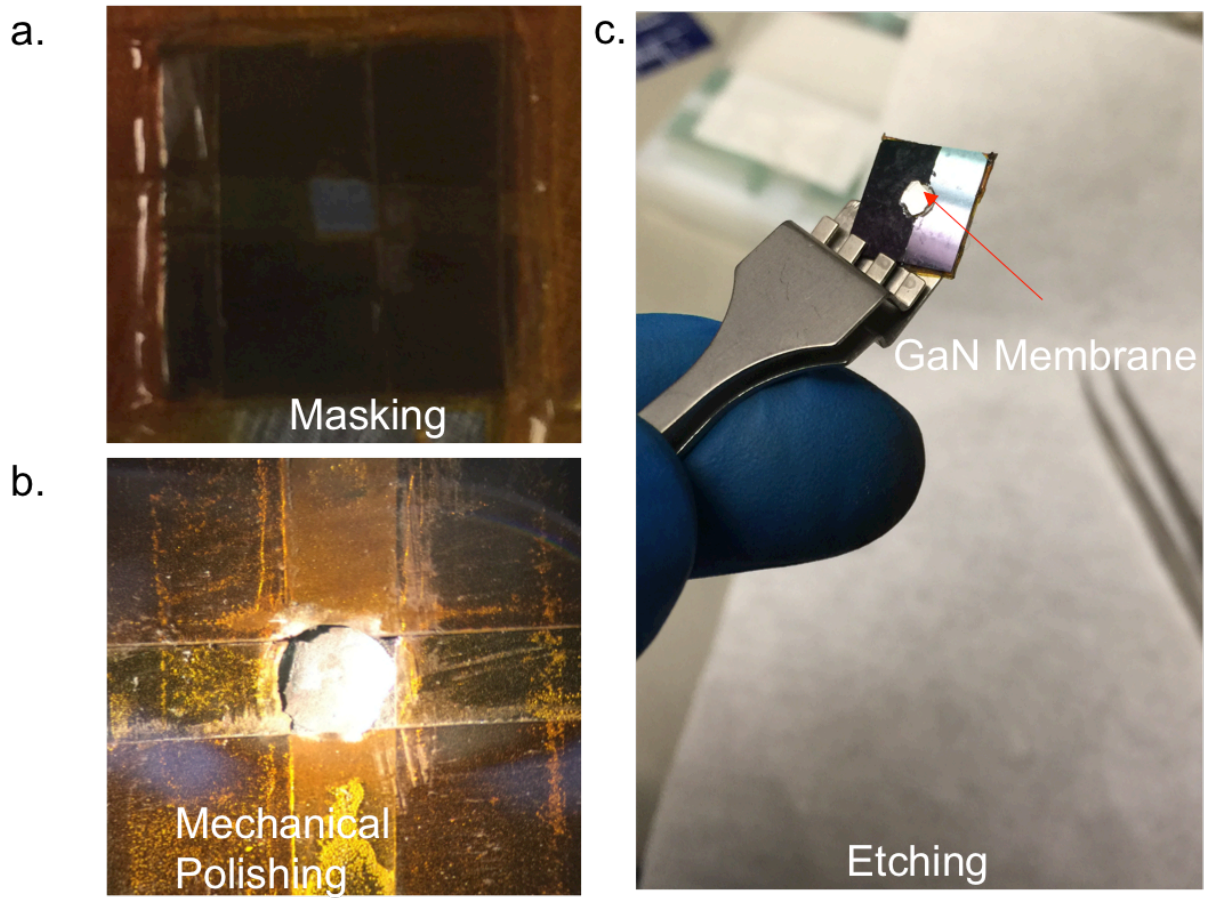

Figure A.2 Pictures of GaN/Si wafer processing. a. polyamide masking b. mechanical polishing c. after etching process is completed. (Access channels are not visible in this pictures)

A.1.2 Back Surface Polishing, Masking, & Etching

The backside of the wafer is polished by diamond paste or a simple rock polisher. The best results were obtained when the front side of the wafer, GaN side, was attached on a glass substrate, then the back side was partially masked with a polyamide film tape (Fig. A.1.2a) and polished with a rotary tool (Fig. A.1.2b). This step must be carried out carefully to avoid any cracking or breaking of the silicon. After the silicon layer was thin enough, the polymide film was removed and the thin silicon layer was photolithographically masked by a silicon nitride (Si_3N_4) film while adding injection channels (Fig. A.1.3a). Then, the unmasked silicon layer was entirely etched by 45wt % potassium hydroxide (KOH, Sigma-Aldrich) at 110^{o}C for 14h. Please also note, during this process the injection channels do not etch all the way through because these channels are not initially polished. Finally, and most importantly, the thickness of Si_3N_4 must be adjusted with respect to the thickness of the remaining silicon and KOH etching concentration. It is crucial to check the final silicon thickness after polishing and calculate the etching rates for the particular sample because there is no direct recipe and there are always significant variations between samples.

Moreover, GaN film usually comes on the Si (111) substrate which another aspect that makes this back-surface etching more complicated. Because etching of Silicon (111) crystallographic planes is much slower when compared with other silicon planes. This is not disadvantageous, but rather advantageous for a successful h-BN transfer because the KOH solution etches the other planes much faster than the silicon (111). Thus, it leaves a rather uneven, odd shape but overall smooth surface without sharp edges that h-BN can be transferred and settle more effectively on the surface of the substrate (Fig. A.1.3).

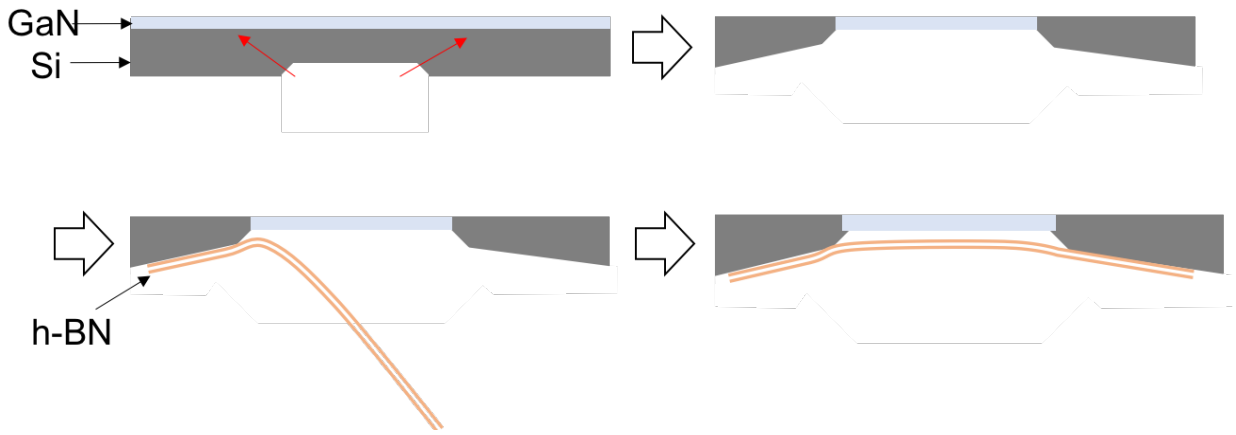

Figure A.3 Wet etching of GaN/Si (111) substrate and h-BN transfer steps.

Even though KOH etching gives successful results, it produces relatively low yield as KOH etching is not easily controlled and sample to sample variation is prominent. The best yield is obtained by direct SF6 etch but this method is very expensive and more complicated. However, the combination of SF6 and KOH etch provides the best results and yield. It produces a very high quality GaN window and leaves a very good platform for h-BN transfer.

A.1.3 Top Contact Evaporation

It is very important to create ohmic contact with GaN because the performance of the devices strongly depends on the contact resistance. In this research, the Ti/Al/Ni/Au (30/100/20/150nm) stack layer is chosen to be the ohmic contact for the GaN window layer and is deposited by e-beam lithography. After the e-beam evaporation, this stack layer is annealed with rapid thermal annealing at 850^0C. Annealing should be performed under inert atmosphere to prevent any decomposition of GaN.

A.1.4 h-BN Transfer

h-BN transfer is one of the bottlenecks of this fabrication process because h-BN needs to transfer on to the receiver substrate before perovskite layer deposition. This creates an extra challenge and requires h-BN to be slightly suspended on the window layer. To ensure this process is successful, the h-BN should cover the entire substrate, not only the window layer so it can easily settle down on the prepared substrate without tension. The best yield is achieved on the substrates with a geometry shown in Fig. A.1.3. The h-BN is transferred directly onto the substrate according to ref. *115*.

A.1.5 Perovskite deposition

Transferring h-BN before perovskite deposition complicates the process because it requires a method that $CH_3NH_3SnI_3$ can deposit under the h-BN layer. We have developed a technique called the syringe method, where a perovskite can be injected underneath the h-BN layer.

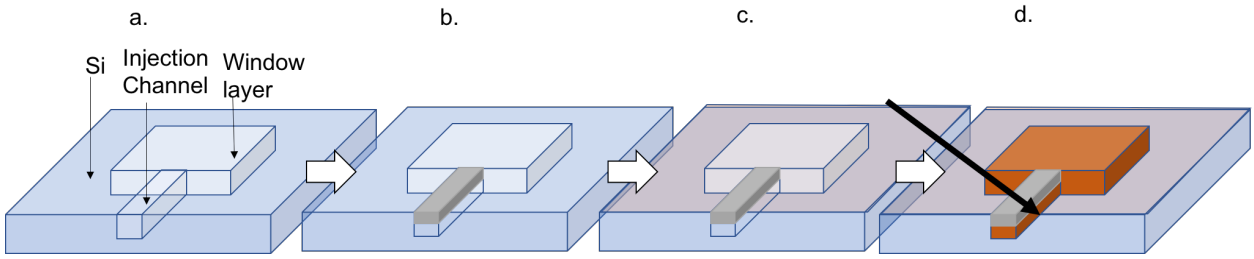

Figure A.4 a. Receiver substrate after etch b. Injection channel is partially filled with wax or a polymer c. h-BN transfer on top of the receiver substrate d. Perovskite is injected through the injection channels underneath the h-BN.

Figure A.1.4 illustrates $CH_3NH_3SnI_3$ deposition underneath the h-BN layer. The prepared substrate with injection channels is shown in Fig. A.1.4a. These injection channels should be partially filled with wax or polymer before the h-BN transfer (Fig. A.1.4b). This partial filling is very important because it also provides an additional adhesion to the h-BN layer during the transfer (Fig. A.1.4c). After the h-BN transfer, the perovskite layer is injected from the far side of the channel (Fig. A.1.4d). During this process, the syringe must be very stable otherwise the h-BN layer could be easily damaged. After this step, the sample is spun to uniformly deposit perovskite on the GaN surface and remove excess fluids from the active window region.

A.1.6 Graphene Aerogel Adaptation

The HTM layer was deposited on a graphene aerogel by spin coating as described in section 3.1.1.4. It is very important to let the sample sit at least 5 minutes to allow uniform HTM penetration into the GA. After this step, $CH_3NH_3PbI_{3-x}Br_x$ was spin coated onto the HTM/GA layer with the traditional drop cast method. This second layer was immediately placed onto the first layer, in the glove box, and annealed at 60°C. During this placement, sometimes it is necessary to re-wet the surface with perovskite solution in order to create uniform bonding across the layers.

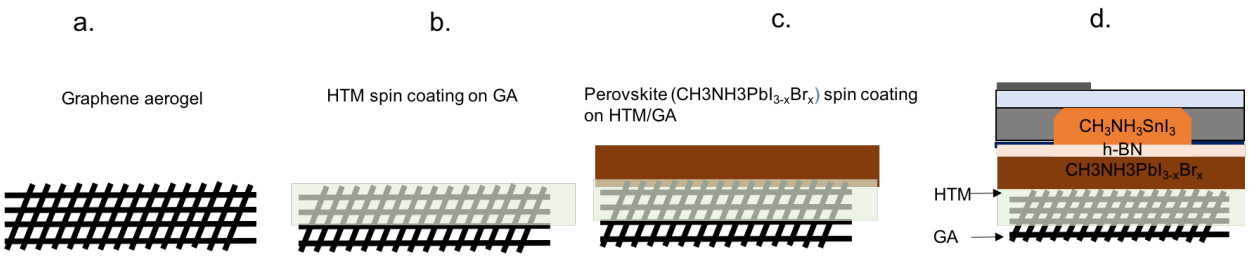

Figure A.5 Schematics of graphene aerogel adaptation. Graphene aerogel is used as a platform to deposit HTM and perovskite layers.

A.2 Supplementary Figures

This section provides supporting figures and tables.

A.2.1 Supporting Information Content

A.2.1A Material Characterization

- Absorption and Photoluminescence measurements
- SEM-EDAX study
- Top view SEM Images
- XRD patterns

A.2.1B Electrical Characterization

- Current density vs. Time
- Hall Effect mobility measurements
- I-V curve of champion cell
- The reverse and forward sweep of perovskite cells
- Ohmic contact behavior of GaN
- NIR-PL spectra of graded band gap perovskite cells
- $MASnI_3$ based solar cell with only GA modification
- EQE&IQE data of champion cell with integrated photocurrent
- Back surface pits on the GaN suface
- Mott-Schottky measurements GaN/Perovskite interface

A.2.1A Material Characterization

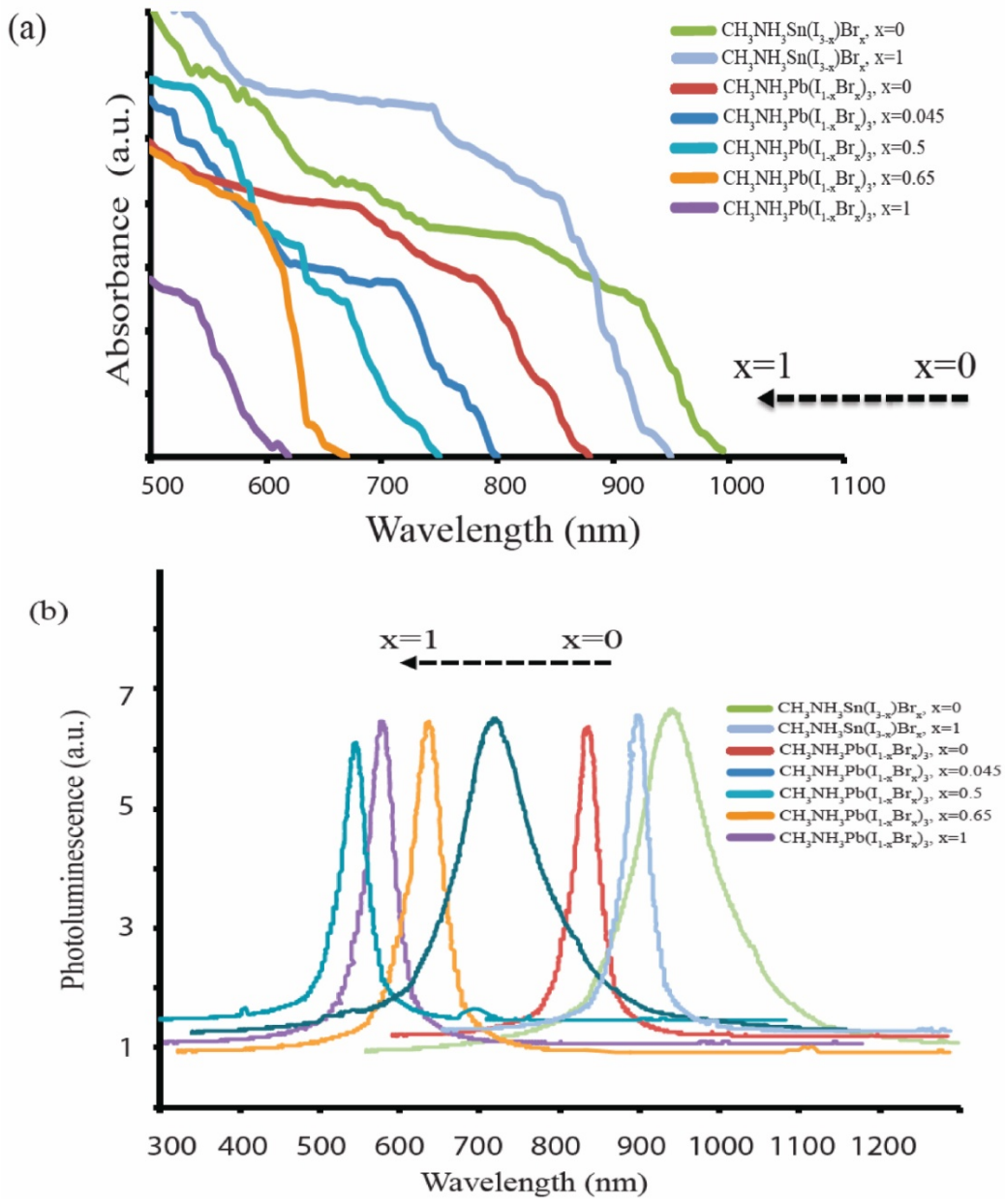

Figure A-S 1 Concentration variation. a. UV-visible light absorption spectra of $CH_3NH_3SnI_{3-x}Br_x$ and $CH_3NH_3Pb(I_1\text{-}_xBr_x)_3$, with varying iodide concentration "x", b. Photoluminescence (PL), spectra of perovskite cells, $CH_3NH_3SnI_{3-x}$ and $CH_3NH_3Pb(I_1\text{-}_xBr_x)_3$, by varying iodide concentration

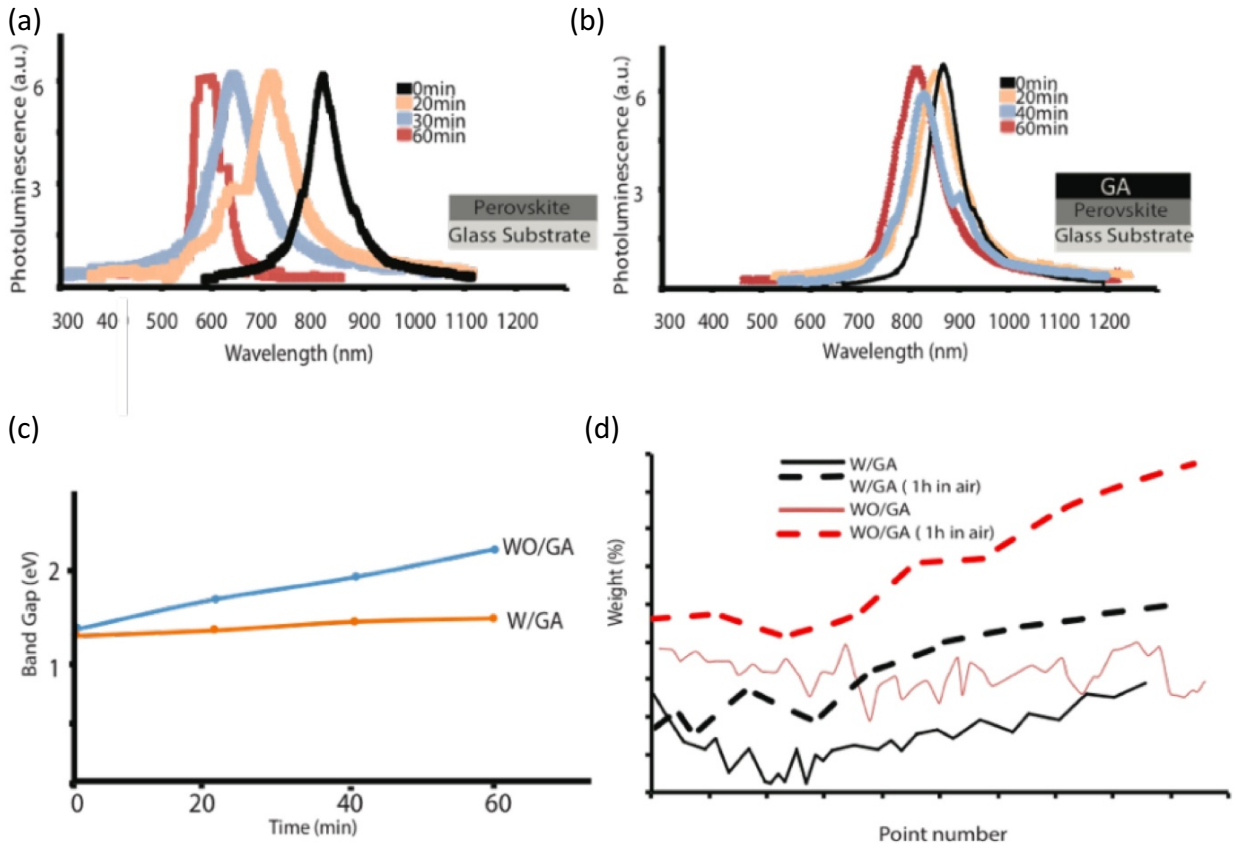

Figure A-S 2 The role of the graphene aerogels on stability. Photoluminescence analysis of perovskite cells in air (only $CH_3NH_3PbI_{3-x}Br_x$). a. without GA. b. with GA modification. c. Bandgap changing by time with and without GA layer. d. EDAX line mapping for oxygen signature of a perovskite with and without GA modification. Graphene aerogel encapsulation acts as a barrier for oxygen penetration and moisture ingress.

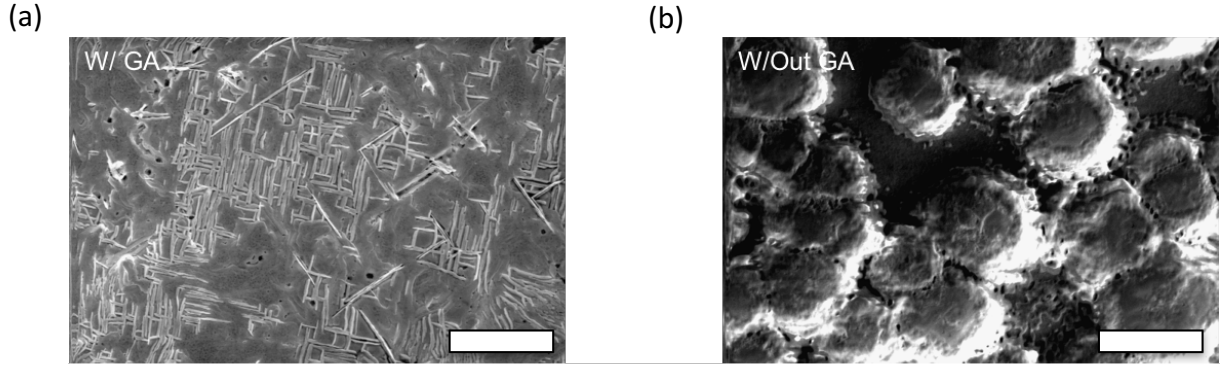

Figure A-S 3 The role of the graphene aerogels on crystallinity a. Top view SEM image of a perovskite sample after peeling off GA layer. The line formations arise due to interfacial adhesion. b. Top view SEM image of samples without GA improvement. The scale bars in the SEM images are 5μm.

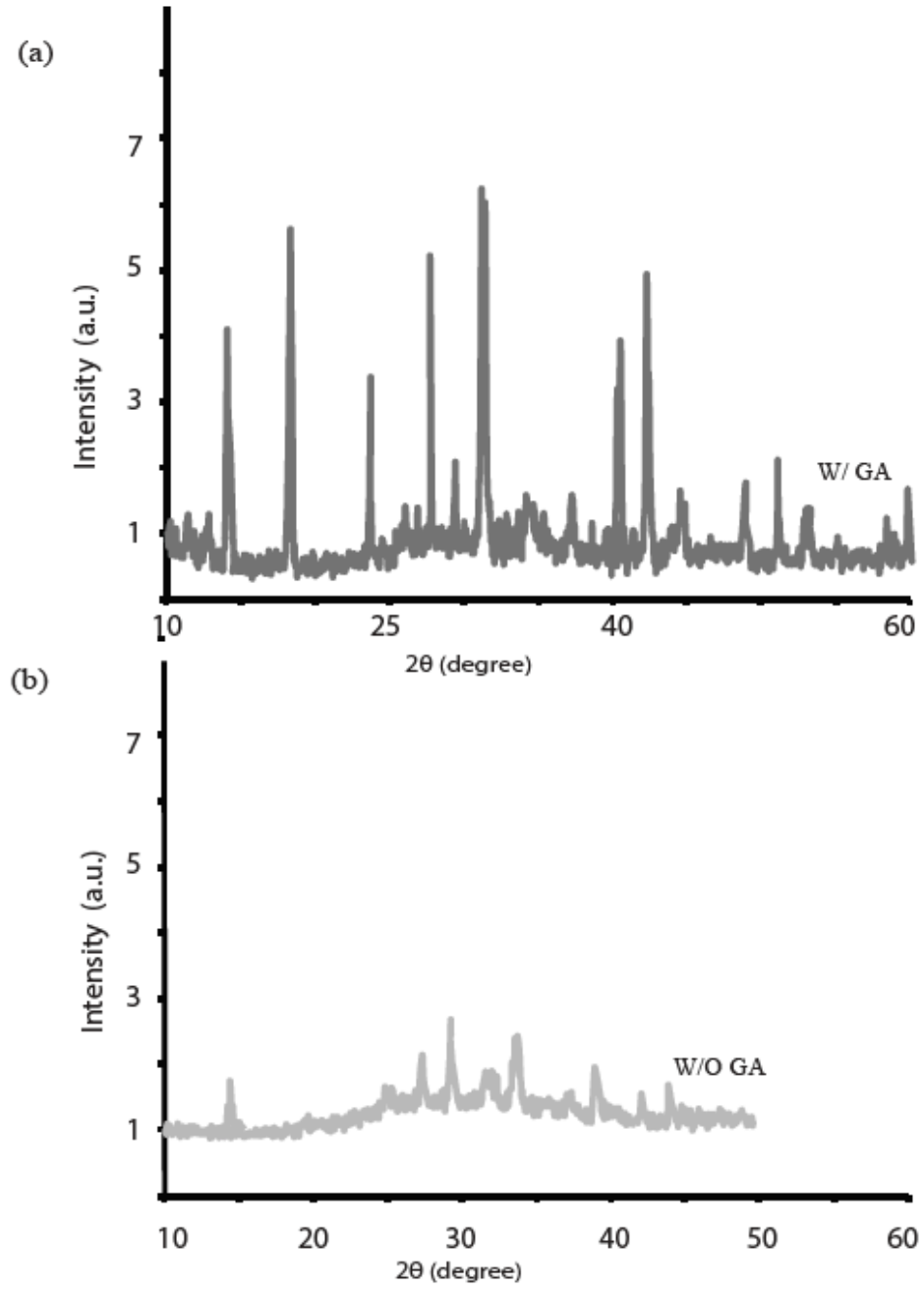

Figure A-S 4 The role of the graphene aerogels on crystallinity XRD diffraction patterns of the perovskite layers of a. W/ GA and b. W/O GA.

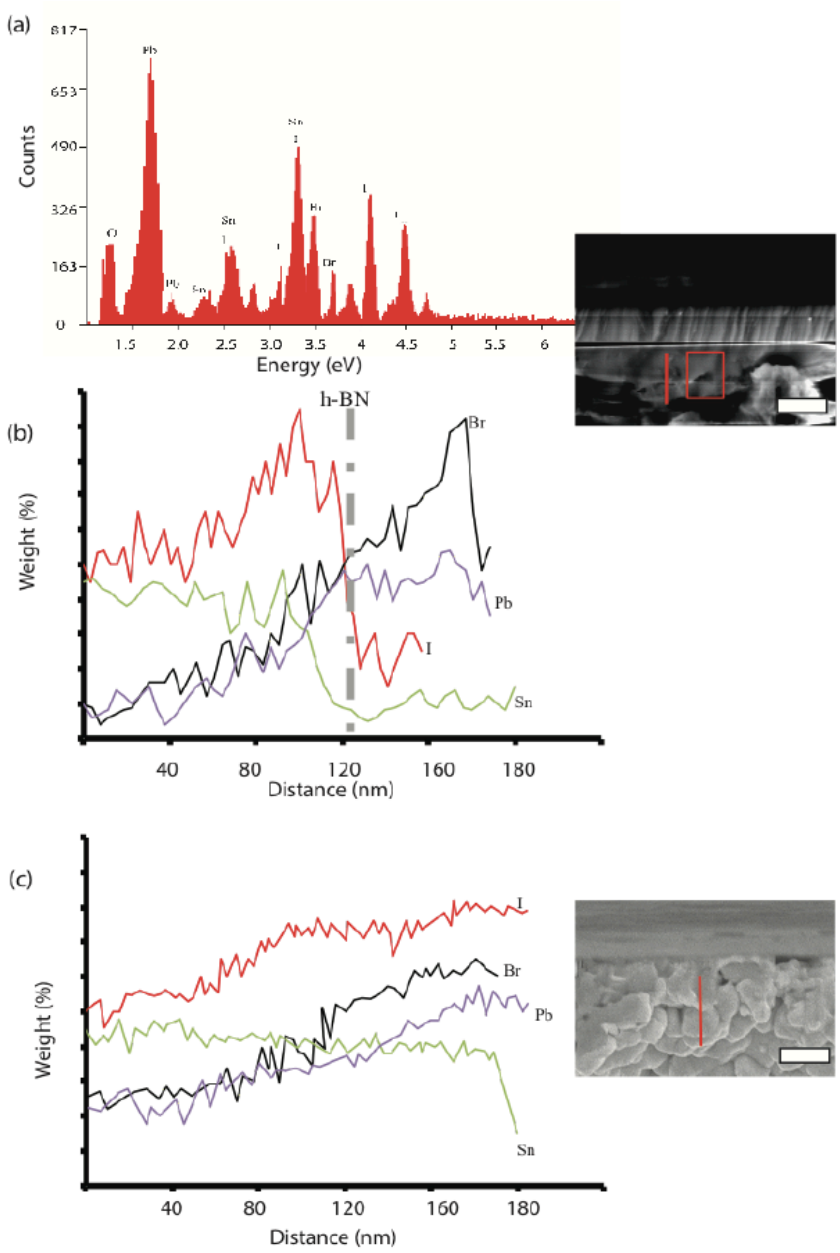

Figure A-S 5 The role of the h-BN Cross sectional SEM-EDAX analysis of perovskite cells a. EDAX signal for cell with h-BN, over the area outlined by red box in the inset SEM image. b. Line mapping of cell with h-BN modification (dashed line indicates the position of h-BN). The scan is along the vertical red line (from top to bottom) shown in the inset SEM image. (c) Line mapping of cell without h-BN modification. The scan is along the red vertical line (from top to bottom) shown in the inset SEM image. Scale bar for inset of a) and b) is 200nm; scale bar for inset of c) is 100nm.

A.2.1B Electrical Characterization

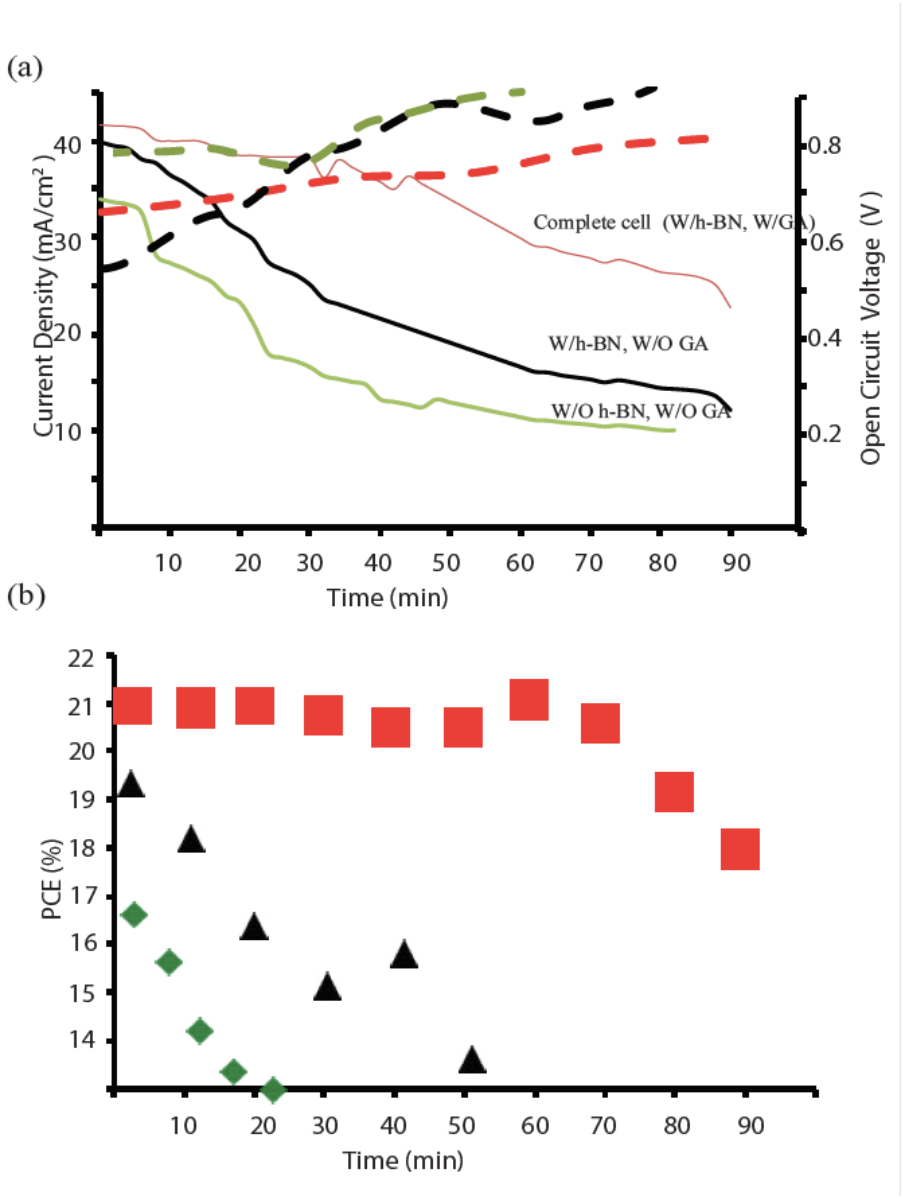

Figure A-S 6 Stability under illumination. a. Time dependent Current density (solid lines) and Voc (dashed lines) is shown. The cells without h-BN and GA exhibit faster degradation under constant illumination compared to the complete cell with h-BN and GA. (solid lines is Jsc and dashed lines is V_{oc}) b. Power conversion efficiency of the cells with h-BN and GA (red), cell w/h-BN and W/O GA (black), W/O h-BN and W/O GA (green). Complete cells show a very stable behavior under constant illumination. Even though a decrease was observed in the current density, there is a constant increase in open circuit voltage indicating that efficiency becomes stable with time.

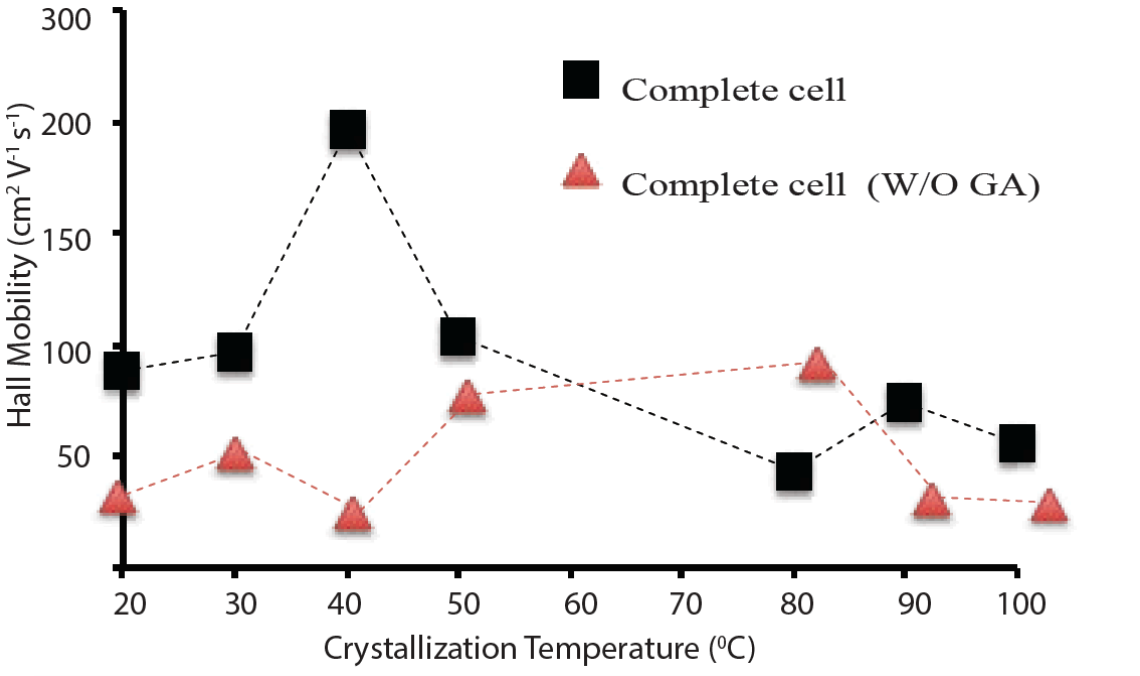

Figure A-S 7 The role of the graphene aerogels on mobility. Hall effect measurement. The mobility plotted against the annealing temperature of double layered perovskite cells (re-crystallization temperatures).

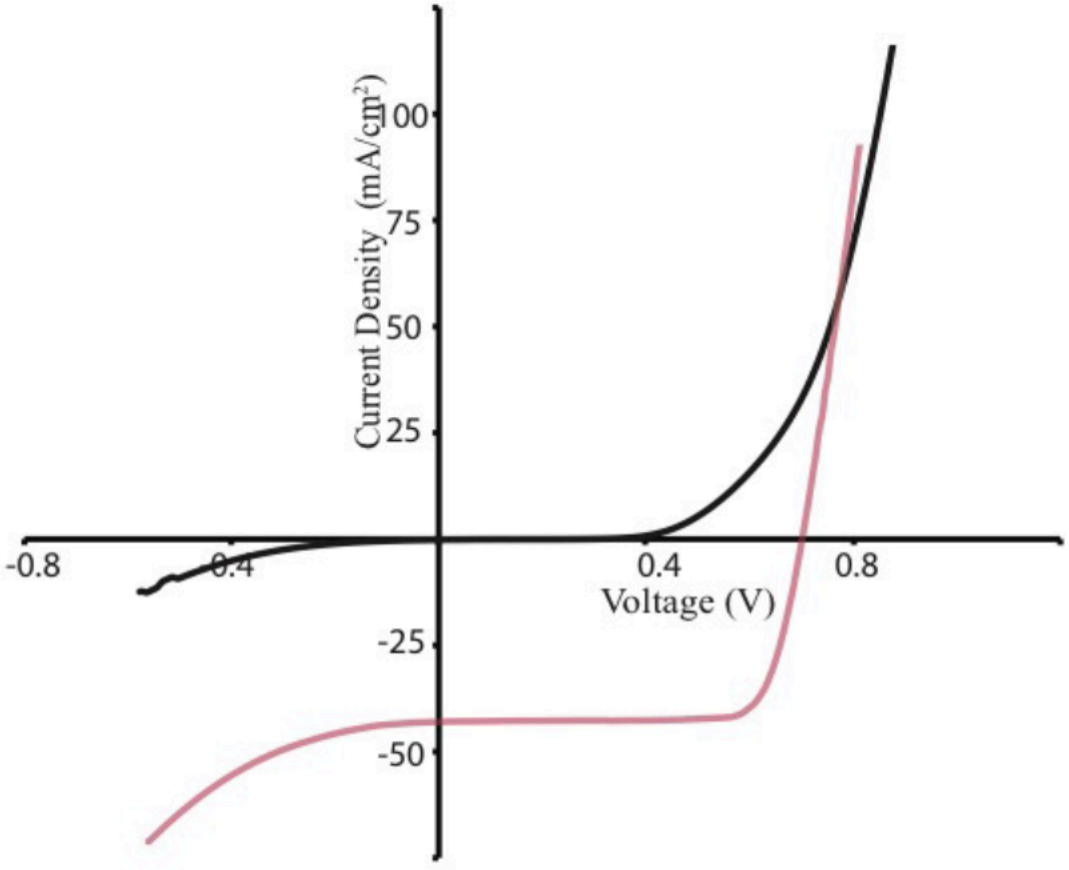

Figure A-S 8 J-V curves for 21.7% PCE graded band gap perovskite cell with (red) and without (blue) light illumination.

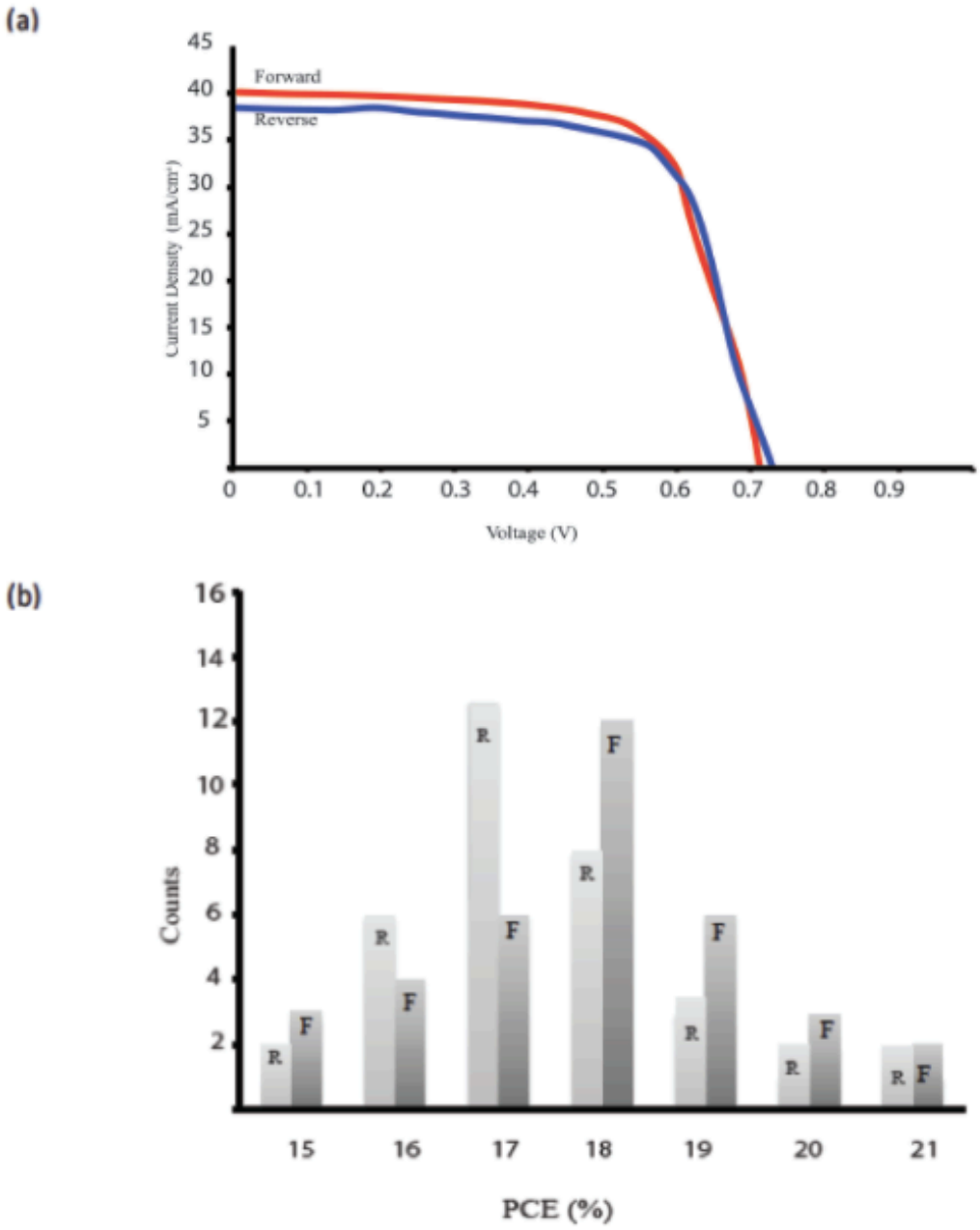

Figure A-S 9 (a) Reverse and forward sweep (<0.01V/s) J-V for a typical graded band gap perovskite device. (b) Histogram of solar cell efficiencies with reverse and forward sweep, after 1h illumination in air.

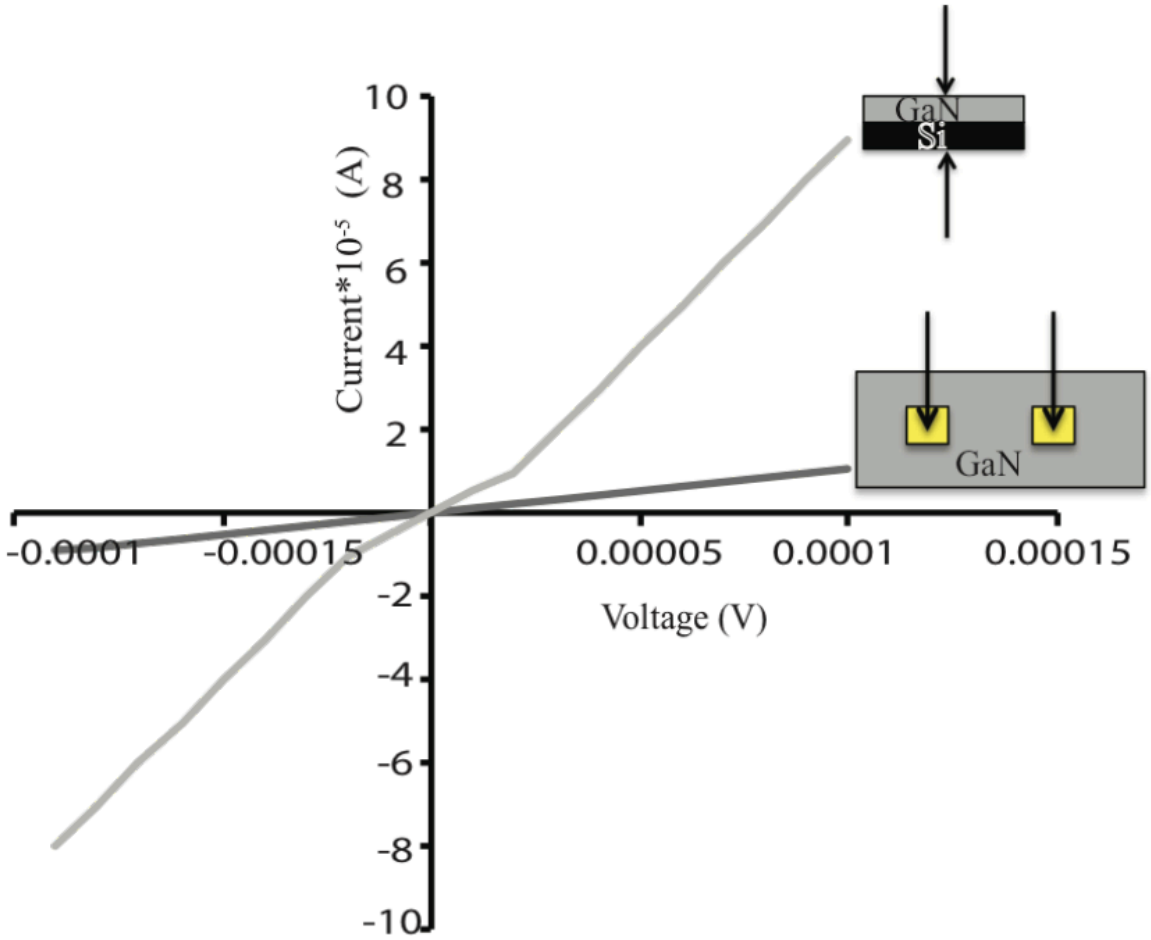

Figure A-S 10 Ohmic contact behavior illustrated by current-voltage (I-V) plots. The GaN contact paths are made from Ti/Al/Ni/Au (30/100/20/150 nm).

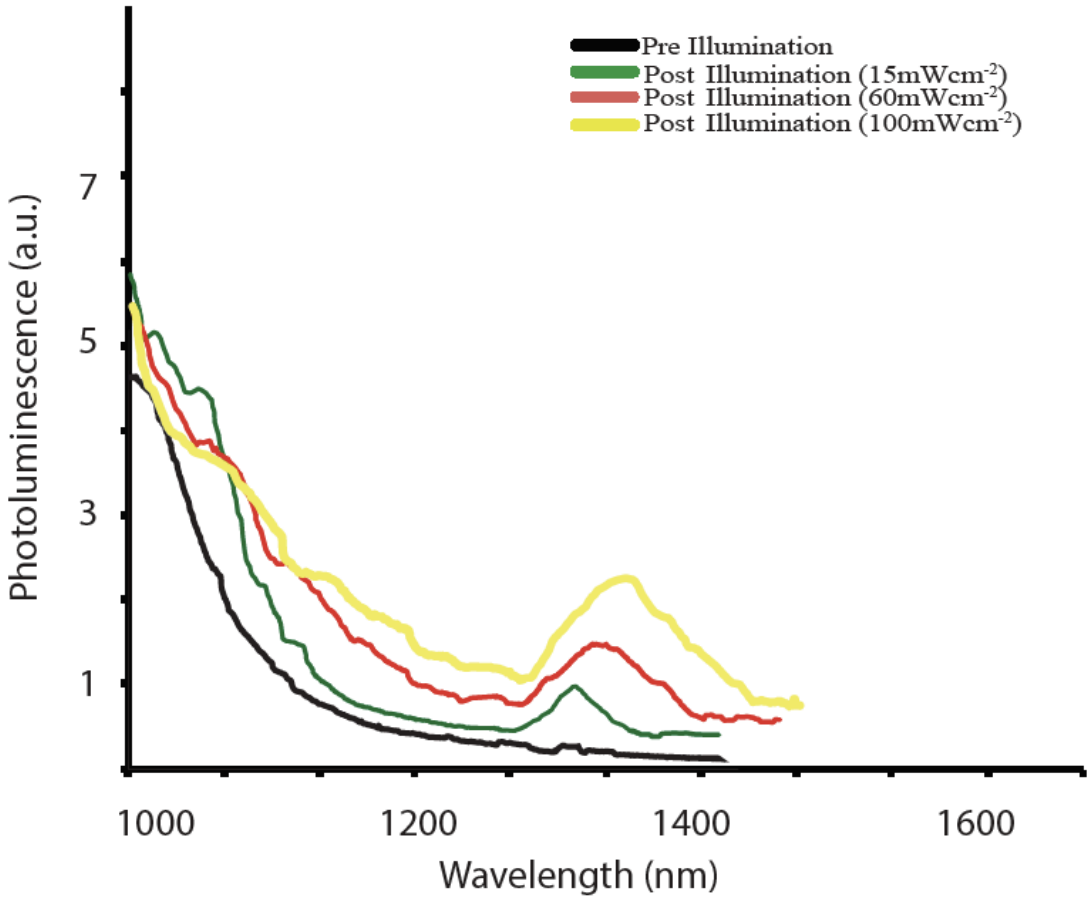

Figure A-S 11 Near infrared photoluminescence (NIR-PL) spectra of graded band gap perovskite solar cells, with both h-BN and GA modifications. Under constant illumination an additional PL peak forms near 1300nm and grows with increasing light intensity.

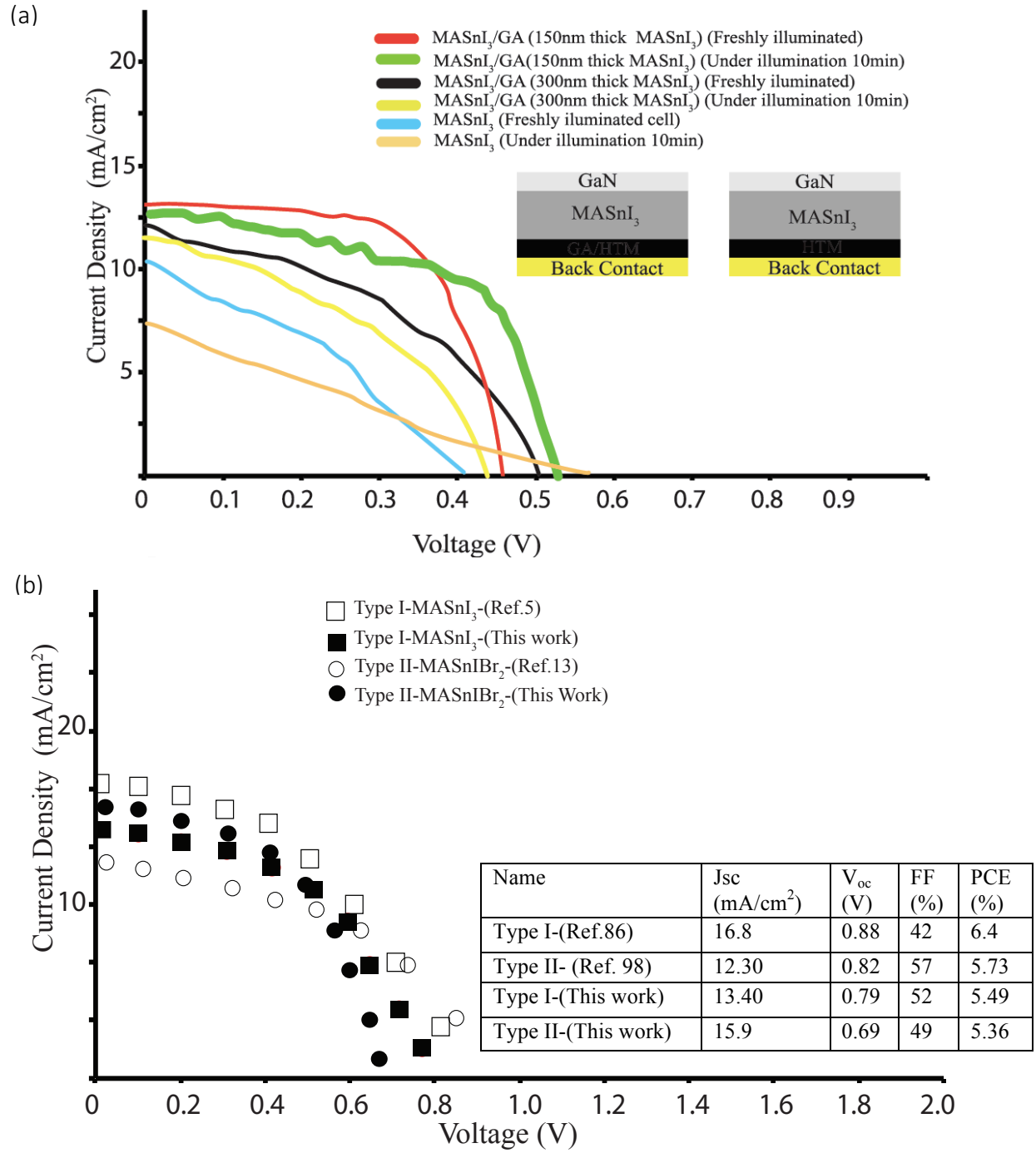

Name	Jsc (mA/cm^2)	V_{oc} (V)	FF (%)	PCE (%)
Type I-(Ref.86)	16.8	0.88	42	6.4
Type II- (Ref. 98)	12.30	0.82	57	5.73
Type I-(This work)	13.40	0.79	52	5.49
Type II-(This work)	15.9	0.69	49	5.36

Figure A-S 12 a. J-V measurement of $MASnI_3$ based solar cells with and without GA. Devices prepared with GA show better stability in air. (All devices prepared in air). b. J-V measurement of $MASnI_3$ based devices which are fabricated by following the same procedures as shown in refs. 86 and 98, Type I and Type II respectively. Type I and Type II cells have the similar architecture (FTO/d-TiO_2/mp-TiO_2/$MASnI_3$/spiro-OMETAD/Au), but different ETL, HTL and Au thicknesses. The table shows the detailed comparison of our cells prepared and cells reported in the literature.

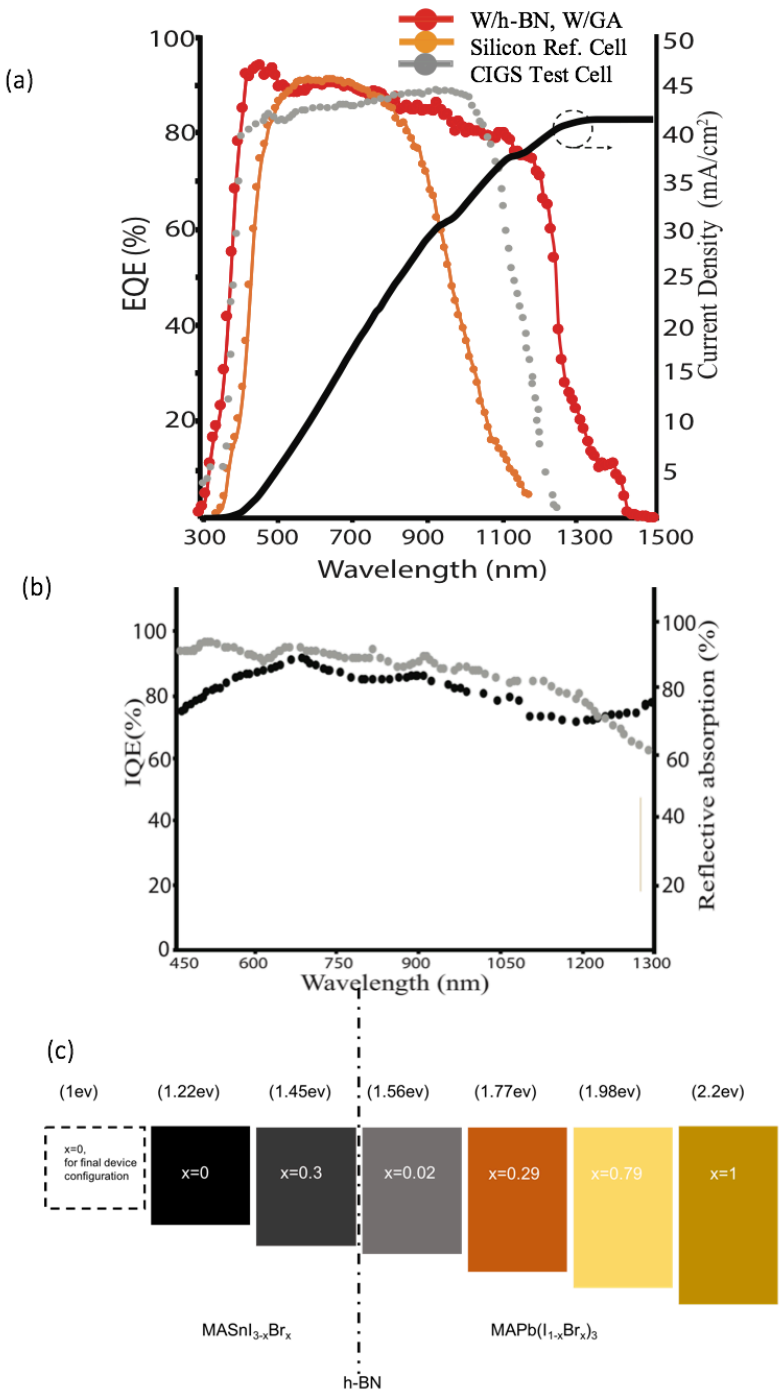

Figure A-S 13 a. External quantum efficiency of the champion cell with integrated photocurrent (thick black line). Maximum possible J_{sc}, if the QE is 100% over the spectrum, is 49.4mA/cm^2 and the expected J_{sc} is 42.32mA/cm^2. The EQE spectrum for reference silicon cells is also shown under A.M 1.5. b. The plot of reflective absorbtion and internal quantum efficiency (IQE) versus wavelength. c. The composition profile and approximate band diagram of the cells. The dashed box shows the approximate band gap of the final device configuration. For the final device, the band gap energies lower to 1 eV range.

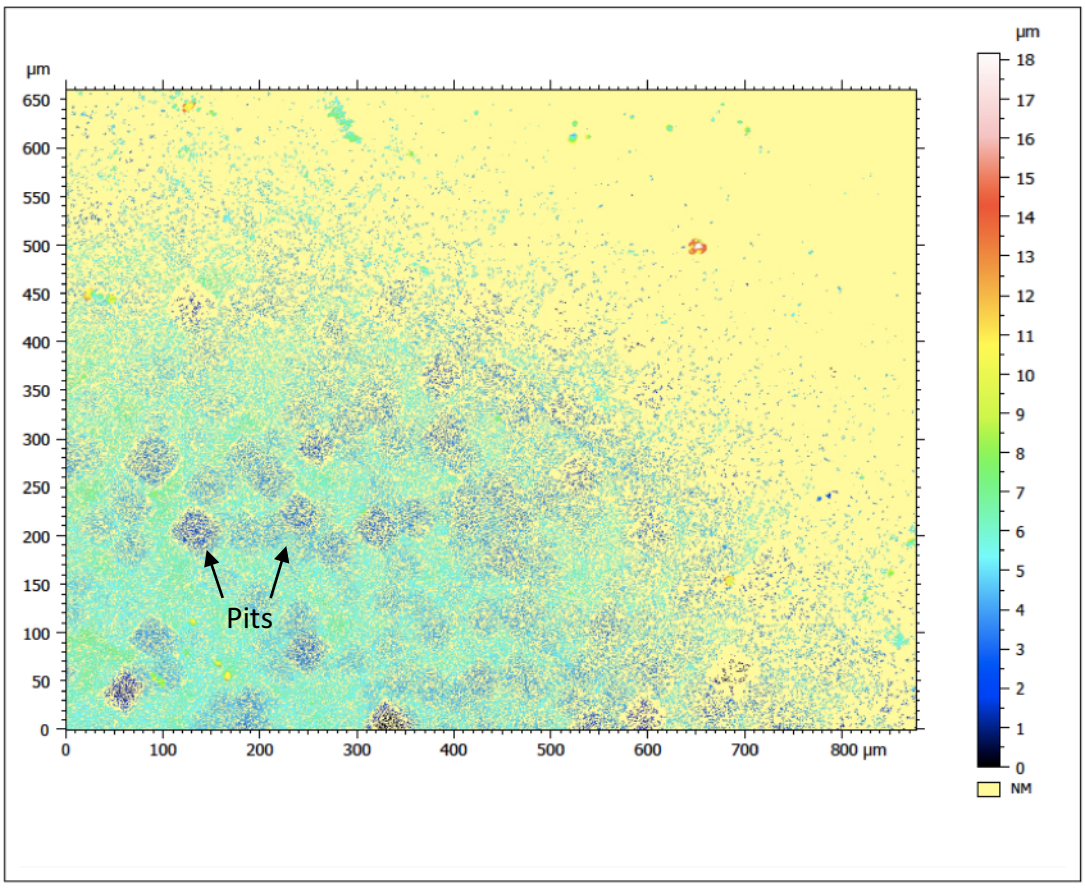

Figure A-S 14 Back surface pits on the GaN surface after etching. The cells display excellent light trapping properties due to these textured surface properties.

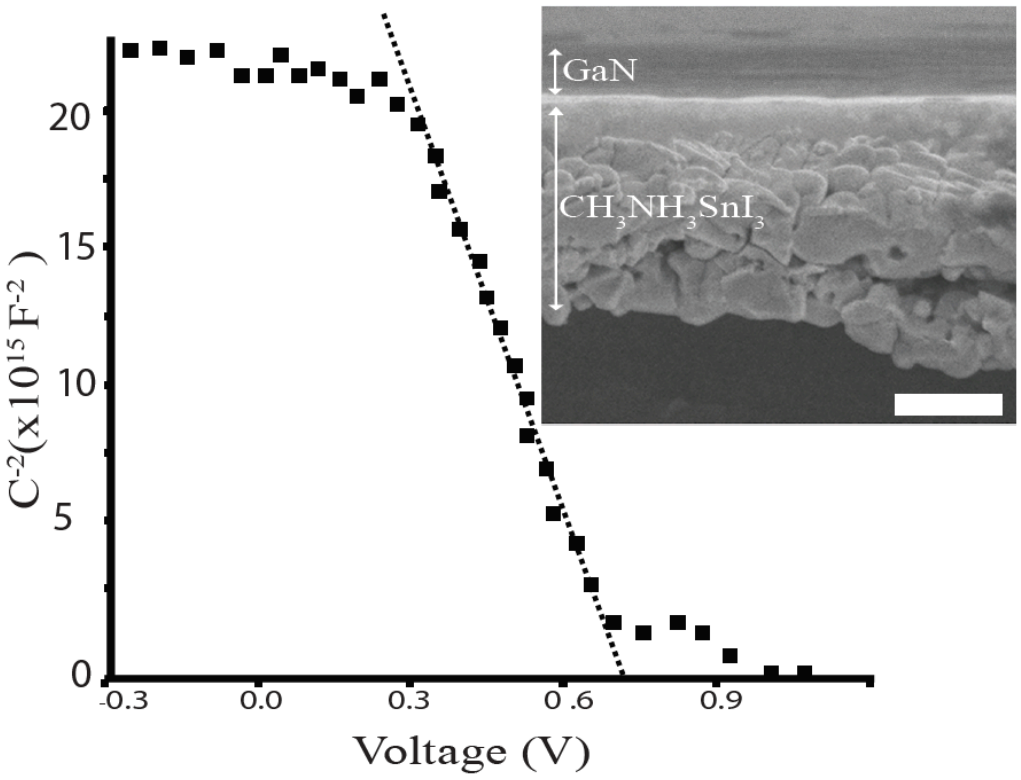

Figure A-S 15 Mott-Schottky analysis for the GaN/$CH_3NH_3SnI_3$ interface. The dotted line is the linear fit to experimental data. The doping density of the perovskite film is found to be $1.4x10^{17}cm^{-3}$. The inset shows the cross sectional SEM image of the GaN/ $CH_3NH_3SnI_3$ device (scale bar is 50nm). The depletion width within the perovskite is calculated to be ~115nm.

A.3 Independent Laboratory Measurements

We received a confirmation of photovoltaic performance from an independent certified laboratory, Newport Inc, 439 days after the device fabrication. Even after this significant period of time, our devices maintain very stable performance and one device is certified at an efficiency of 15.77%. To the best of our knowledge, this is the longest time a perovskite solar cell has survived and still maintains a high performance. However, our cells have evolved during this time span, as expected in Fig.S6a. The certified cell, now, exhibits a very high open circuit voltage (~2eV), fill factor (~80%), and almost no hysteresis. It is clear that a recombination center is formed in the h-BN, as an efficient extracting layer. However, at this point it is very difficult to explain why or how the perovskite forms this interface.

Table A.1 Independent Laboratory Measurements (Newport Corp.) of set of devices ~439 days after the fabrication.

Device Name	Voc[V]	Efficiency[%]	FF[%]	Pmax[mW]	Vmax[V]	Imax[A]	Isc[A]	Area[cm^2]	EQE-Measurement Performed	
#27 [Reverse]	2.054±0.0285	15.77±0.35	81.5±1.7	0.596±0.013	1.7417±0.0204	0.000342±0.000007	0.000356±0.000007	0.0378±0.0002	YES	Certified by Newport
#27 [Forward]	2.0532±0.0285	15.76±0.35	81.4±1.7	0.596±0.013	1.7398±0.0204	0.000342±0.000007	0.000356±0.000007	0.0378±0.0002	---	Certified by Newport
#24 [Reverse]	2.2686±0.0315	14.46±0.32	81±1.7	0.386±0.008	1.9441±0.0227	0.000199±0.000004	0.00021±0.000004	0.0267±0.0001	---	Pre-Cals (Measurement carried by Newport)
#24 [Forward]	2.2667±0.0315	14.44±0.32	80.9±1.7	0.386±0.008	1.9426±0.0227	0.000199±0.000004	0.00021±0.000004	0.0267±0.0001	---	Pre-Cals (Measurement carried by Newport)
#23 [Reverse]	2.2878±0.0318	14.42±0.32	80.9±1.7	0.426±0.009	1.9589±0.0229	0.000218±0.000004	0.00023±0.0000005	0.0296±0.0001	---	Pre-Cals (Measurement carried by Newport)
#23 [Forward]	2.2708±0.0316	14.28±0.31	80.5±1.7	0.422±0.009	1.9411±0.0227	0.000218±0.000004	0.000231±0.000005	0.0296±0.0001	---	Pre-Cals (Measurement carried by Newport)
#29 [Reverse]	2.353±0.0327	------	81.5±1.7	0.879±0.019	2.0083±0.0235	0.000438±0.000009	0.000458±0.000009	------	---	Pre-Cals (Measurement carried by Newport)
#29 [Forward]	2.3464±0.0326	------	81.8±1.7	0.881±0.019	2.0045±0.0235	0.00044±0.000009	0.000459±0.000009	------	---	Pre-Cals (Measurement carried by Newport)
#25 [Cell Died]	------	------	------	------	------	------	------	------	YES	------

Newport		Technology and Application Center PV Lab Calibration Number 1688

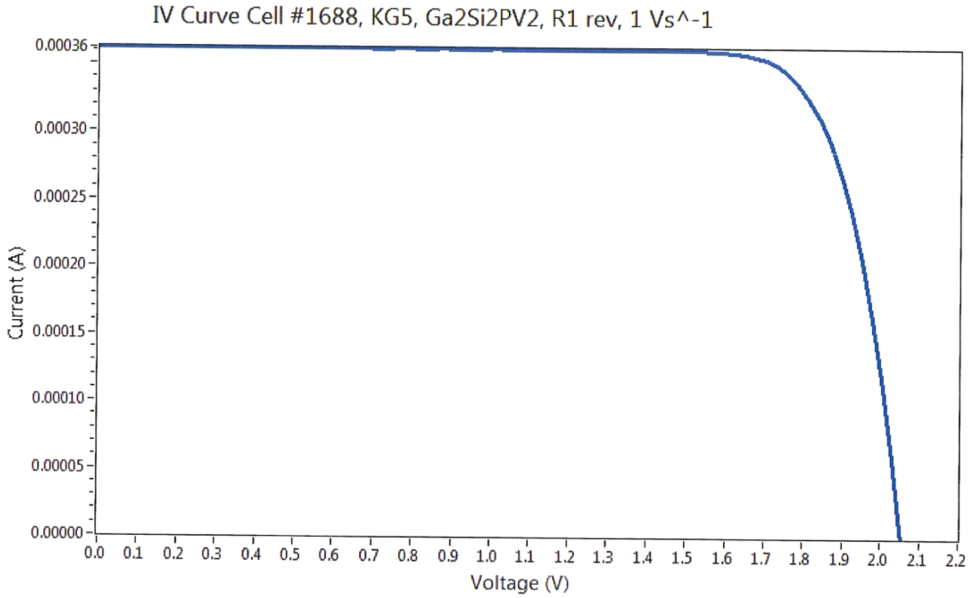

Cal Cert Data V1_2	Issue Date: May 22, 2017	Page 1of 5
	Reviewed and Approved by: Geoffrey Wicks	

A.4 Device Look-up List

Please note the data from the figures are not from the same device. We evaluated similarly constructed (but not absolutely identical) devices; one showed the best PL and the other the best EQE. Because of inevitable variations in starting materials (e.g. porosity of the aerogel, texture of the BN layer, etc.) and construction methods/conditions, devices of similar architecture and construction method do not always have identical response characteristics. Consequently we have a range of performance metrics for a given device type. We acknowledged this in our introduction and presented an average value for the steady-state conversion efficiency, in addition to the best value. As stated in section 3.1, we only reported data from steady state regimes to provide valuable insight to the readers. As it is well known, many of the reported measurements are time consuming; the EQE measurement alone takes more than an hour. When considering degradation of perovskite materials by time and under light, reporting from similarly constructed devices is a reasonable approach to evaluate true potential of our devices.

Here I will provide an extensive sample look-up table describing precisely which measurements correspond to which samples to help the reader make meaningful comparisons between data sets.

Table A.2 Extensive sample look-up table

Figure	Data Set	Device ID	Age of Device When Tested	Notes
2	W/h-BN, W/GA (black trace)	#23*	Few minutes	
	W/h-BN, W/GA (magenta trace)	#23*	1 hour	Measurement following 1 hour light soaking
	W/h-BN, W/O GA (light gray trace)	#7		
	W/h-BN, W/O GA (green trace)	#7	1 hour	Measurement following 1 hour light soaking
	W/O h-BN, W/GA (blue trace)	#9		
	W/O h-BN, W/GA (orange trace)	#9	1 hour	Measurement following 1 hour light soaking
	W/O h-BN, W/O GA (purple trace)	#8		
	W/O h-BN, W/O GA (dark gray trace)	#8	1 hour	Measurement following 1 hour light soaking
3a	W/h-BN, W/GA (black trace)	#26	Few minutes	

	W/h-BN, W/GA (green trace)	#26	1 hour	Measurement following 1 hour light soaking
	W/h-BN, W/O GA (purple trace)	#19*	Few minutes	
	W/h-BN, W/O GA (blue trace)	#19*	1 hour	Measurement following 1 hour light soaking
	W/O h-BN, W/O GA (magenta trace)	#22	Few minutes	
	W/O h-BN, W/O GA (orange trace)	#22	1 hour	Measurement following 1 hour light soaking
3b	W/h-BN, W/GA (Red)	#14	Few minutes	
	W/h-BN, W/O GA (Blue)	#20*	Few minutes	
	W/O h-BN, W/GA (Light Blue)	#17	Few minutes	
	W/O h-BN, W/O GA (Light Blue)	#12*	Few minutes	
4a	W/h-BN, W/GA (Red)	#27*	Few minutes	
4c	W/h-BN, W/GA (Black)	#32	Few minutes	
S1a	$CH_3NH_3Sn(I_{3-x})Br_x$,x=0 (Blue, accen1 light)	#3	Few minutes	Special Cell
	$CH_3NH_3Sn(I_{3-x})Br_x$,x=0 (Green)	#5	Few minutes	Special Cell
	$CH_3NH_3Pb(I_{1-x}Br_x)_x$,x=0 (Red)	#6	Few minutes	Special Cell
	$CH_3NH_3Pb(I_{1-x}Br_x)_x$,x=0.0045 (Blue, accent 1 dark)	#2	Few minutes	Special Cell
	$CH_3NH_3Pb(I_{1-x}Br_x)_x$,x=0.5 (Blue, accent 5 light-green)	#10	Few minutes	Special Cell
	$CH_3NH_3Pb(I_{1-x}Br_x)_x$,x=0.65 (Orange)	#16	Few minutes	Special Cell
	$CH_3NH_3Pb(I_{1-x}Br_x)_x$,x=1 (Purple)	#4	Few minutes	Special Cell

S1b	$CH_3NH_3Sn(I_{3-x})Br_x$,x=0 (Blue, accen1 light)	#3[a]	Few minutes	Special Cell
	$CH_3NH_3Sn(I_{3-x})Br_x$,x=0 (Green)	#5[a]	Few minutes	Special Cell
	$CH_3NH_3Pb(I_{1-x}Br_x)_x$,x=0 (Red)	#6[a]	Few minutes	Special Cell
	$CH_3NH_3Pb(I_{1-x}Br_x)_x$,x=0.0045 (Blue, accent 1 dark)	#2[a]	Few minutes	Special Cell
	$CH_3NH_3Pb(I_{1-x}Br_x)_x$,x=0.5 (Blue, accent 5 light-green)	#10[a]	Few minutes	Special Cell
	$CH_3NH_3Pb(I_{1-x}Br_x)_x$,x=0.65 (Orange)	#16[a]	Few minutes	Special Cell
	$CH_3NH_3Pb(I_{1-x}Br_x)_x$,x=1 (Purple)	#4[a]	Few minutes	Special Cell
S2a	Perovskite on Glass (Black)	#1	Few minutes	Special Cell
	Perovskite on Glass (Orange)	#1	20 minutes	Special Cell
	Perovskite on Glass (Blue)	#1	30 minutes	Special Cell
	Perovskite on Glass (Red)	#1	60 minutes	Special Cell
S2b	GA/Perovskite/Glass (Black)	#1[a]	Few minutes	Special Cell
	GA/Perovskite/Glass (Orange)	#1[a]	20 minutes	Special Cell
	GA/Perovskite/Glass (Blue)	#1[a]	30 minutes	Special Cell
	GA/Perovskite/Glass (Red)	#1[a]	60 minutes	Special Cell
S2c	GA/Perovskite/Glass (Orange)	#1[a]	Continuous 0-1h	Special Cell
	Perovskite on Glass (Blue)	#1	Continuous 0-1h	Special Cell
S2d	GA/Perovskite/Glass	#11	Few minutes	Special Cell

	(Black solid)			
	GA/Perovskite/Glass (Black dashed)	#11	After 60 minutes	Special Cell
	Perovskite on Glass (Red)	#15	Few minutes	Special Cell
	Perovskite on Glass (Red dashed)	#15	After 60 minutes	Special Cell
S3a	GA/Perovskite	--	Few minutes	Special Cell
S3b	W/O GA/Perovskite	--	Few minutes	Special Cell
S4a	GA/Perovskite	--	Few minutes	Special Cell
S4b	W/O GA/Perovskite	--	Few minutes	Special Cell
S5a&b	W/ h-BN Perovskite double layer	#7	Few minutes	Special Cell
S5c	W/ O h-BN Perovskite double layer	#9[a]	Few minutes	Special Cell
S6	W/h-BN, W/GA (Red)	#21	Few minutes	Continuous time measurement
	W/h-BN, W/O GA (Black)	#7	After 60 minutes	Continuous time measurement
	W/O h-BN, W/O GA (Green)	#8	Few minutes	Continuous time measurement
S7	W/h-BN, W/GA (Red)	#18*	Few minutes	Continuous temperature measurement
	W/h-BN, W/O GA (Red)	#13	Few minutes	Continuous temperature measurement
S8	W/h-BN, W/GA	#32	Few minutes	Special Cell
S9a	W/h-BN, W/GA	#25	Few minutes	Special Cell
S11	W/h-BN, W/GA	#30	Few minutes	Special Cell
S12a	$MASnI_3$/GA (150nm thick $MASnI_3$)(Red)	#46	Few minutes	Special Cell
	$MASnI_3$/GA (150nm thick $MASnI_3$)(Green)	#46	10 minutes after light soaking	Special Cell
	$MASnI_3$/GA (300nm thick $MASnI_3$)(Black)	#47	Few minutes	Special Cell
	$MASnI_3$/GA (300nm thick $MASnI_3$)(Yellow)	#47	10 minutes after light soaking	Special Cell
	$MASnI_3$ (Blue)	#42	Few minutes	Special Cell
	$MASnI_3$ (Orange)	#42	10 minutes after light soaking	Special Cell
S12b	$MASnI_3$ W/ GA (Black Solid Square)	# 49	Few minutes	Special Cell

	$MASnI_3$ W/ GA (Black Solid Circle)	#43	Few minutes	Special Cell
	$MASnI_3$ W/ GA (Black Empty Square)	#43	Few minutes	Special Cell
	$MASnI_3$ W/ GA (Black Empty Circle)	#41	Few minutes	Special Cell
S13a	W/h-BN, W/GA	#26	Few minutes	
S13b	W/h-BN, W/GA	# 37	Few minutes	
S14	GaN surface	---	Few days	Special Cell
S15	GaN/ $MASnI_3$	#50	Few minutes	Special Cell

[a] (Multiple devices prepared for characterization from same solution batches. The superscript indicates the perovskite solution is the same but different identical receiver substrates are used)
*Small area device <0.07cm^2

Appendix B

Supplementary Information MIS Solar Cell Devices

B.1 Supplementary Figures

This section provides supporting figures and tables.

Supporting Information Content

- Material Characterization
- Photovoltaic Measurement
- Electrical Characterization
    - Contact Measurement
    - Capacitance Measurement
    - Quantum Efficiency Measurement
- AFM Study

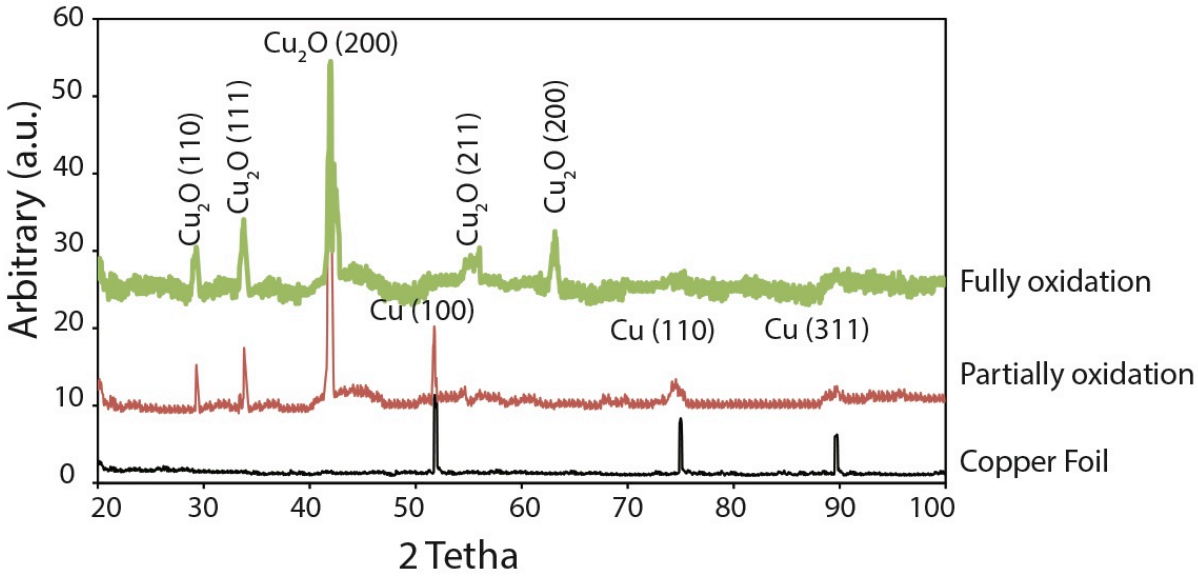

Figure B-S 1 X-ray diffraction pattern of copper foil partially oxidized and fully oxidized trends.

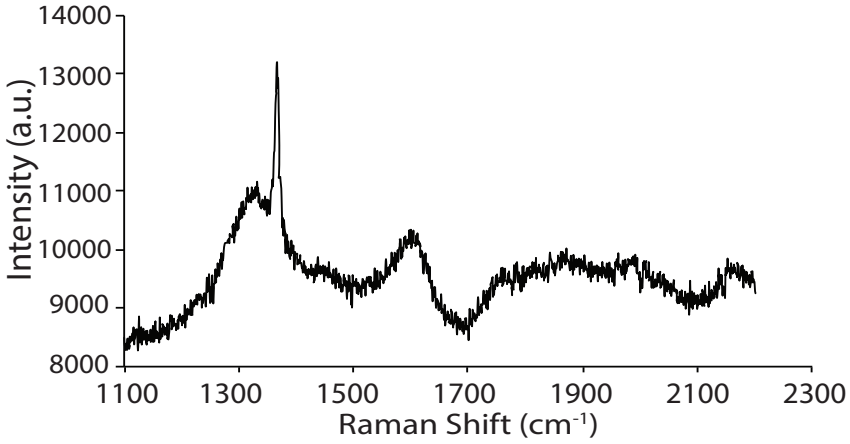

Figure B-S 2 Raman spectrum of exfoliated h-BN layer which was transferred to a Si/SiO_2 substrate after Cu_2O etching. The signature of B-N vibrational E_{2g} peak of h-BN was observed at 1366.7 cm^{-1}. It shows that h-BN remains intact after Cu_2O growth.

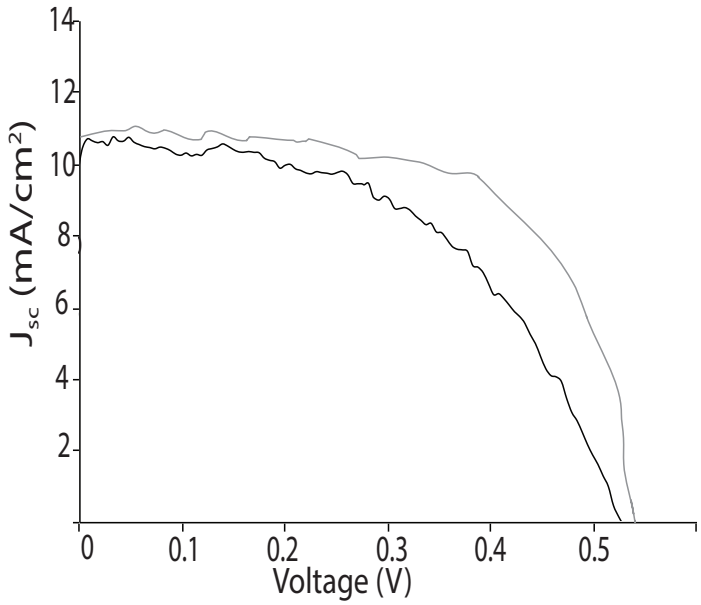

Figure B-S 3 Measurements of J-V curve of Cu/h-BN/Cu_2O/CuO/Au-Cr sample with slow and fast voltage sweeping rate of transient (gray curve) and steady state (black curve). Fast sweeping rate between data points improves FF and efficiency. Apparent efficiency calculated over 4% for transient state.

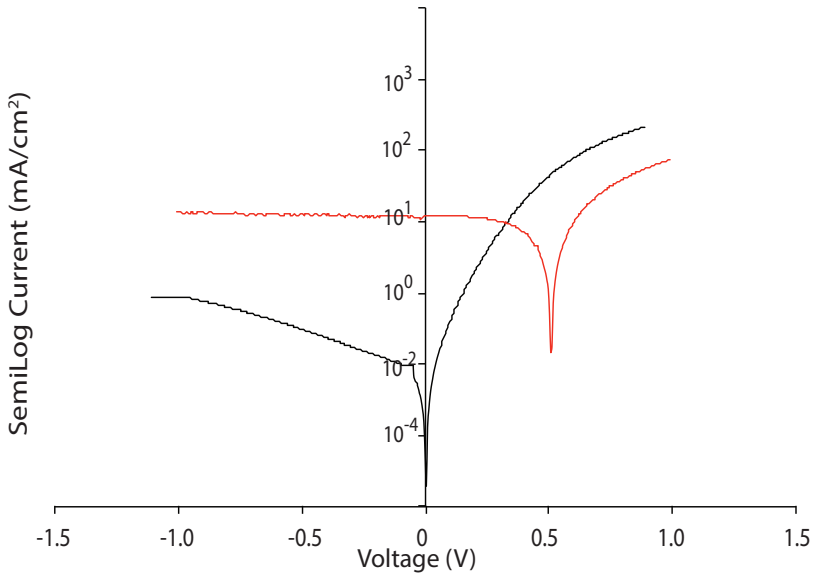

Figure B-S 4 Semi log plot of I-V curve of 3.44% efficient device structure. Voc 0.52V.

(a)	Carrier Concentration (/cm^3)	Mobility (cm^2/V·s)	Resistivity (Ω·cm)(300K)
No BN	5.75x10^{17}	15.78	160.257
O_2 Cooling	4.47x10^{18}	34.29	212.716
N_2 Cooling	3.45x10^{18}	68.66	102.827
H_2 Cooling	8.9x10^{17}	105.73	143.563

Parameters: B=0.6T D=2μm I=0.6mA t=arbitrary

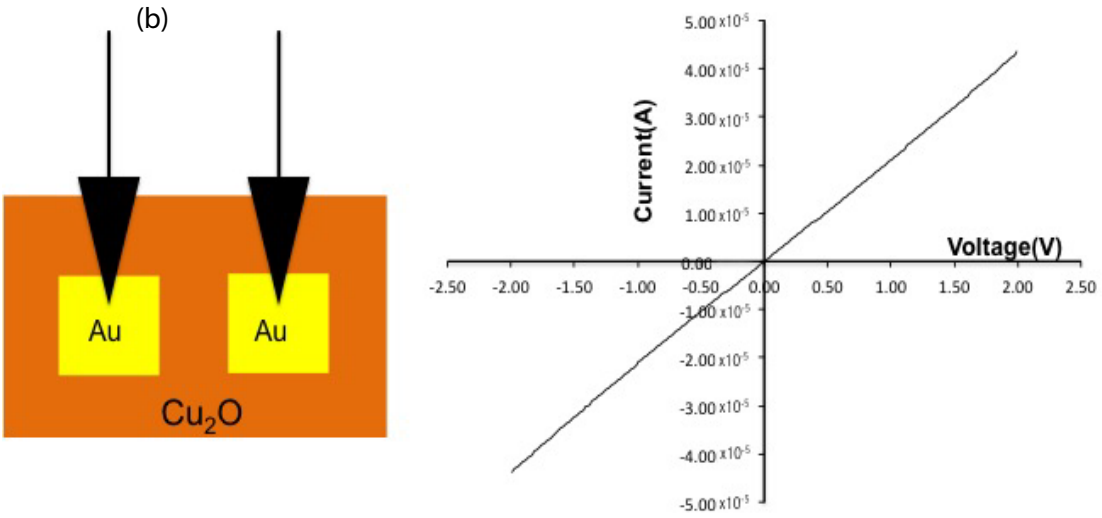

Figure B-S 5 a. Hall effect measurements on Cu_2O structure formed with introducing different cooling gases b. Ohmic contact behavior is shown on IV curve of Au/Cu_2O/Au Junction.

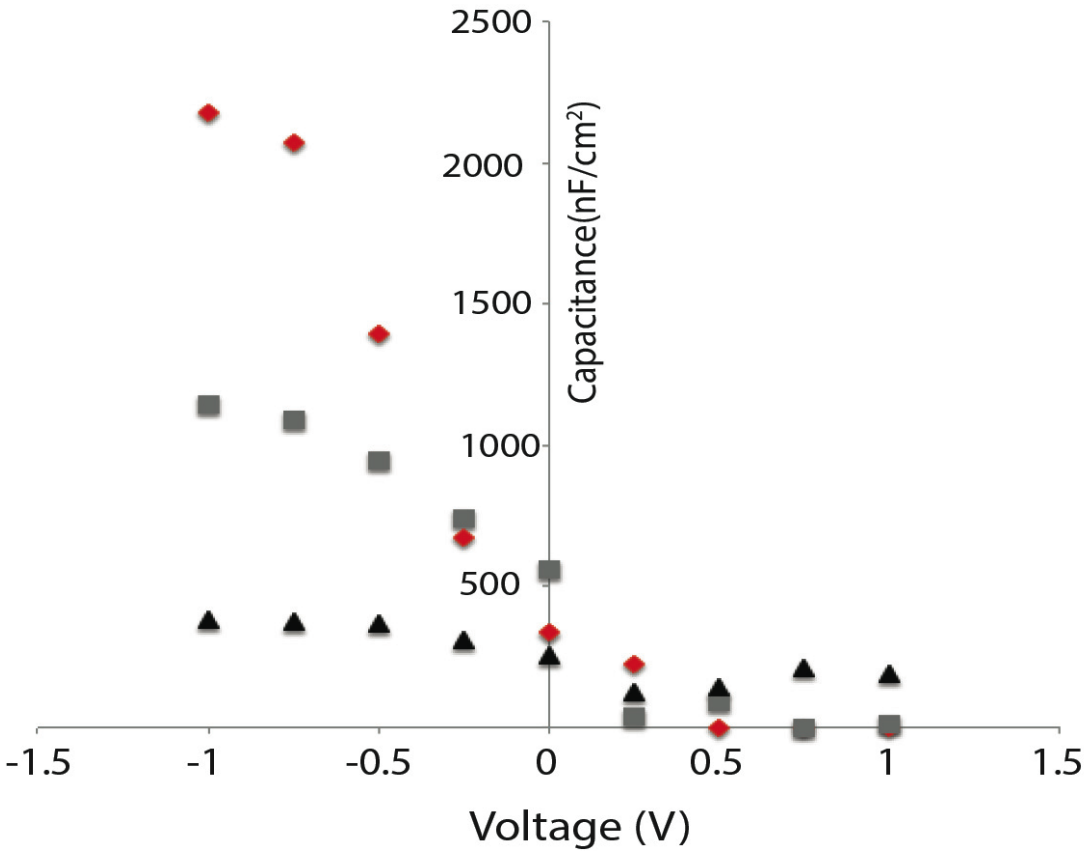

Figure B-S 6 High-frequency (1MHz) C-V curves for Cu_2O MIS-Schottky cells. Capacitance measurements indicate that h-BN thickness thins down up to 1-2nm by exfoliation process. (Capacitance calculation is made in accumulation state)

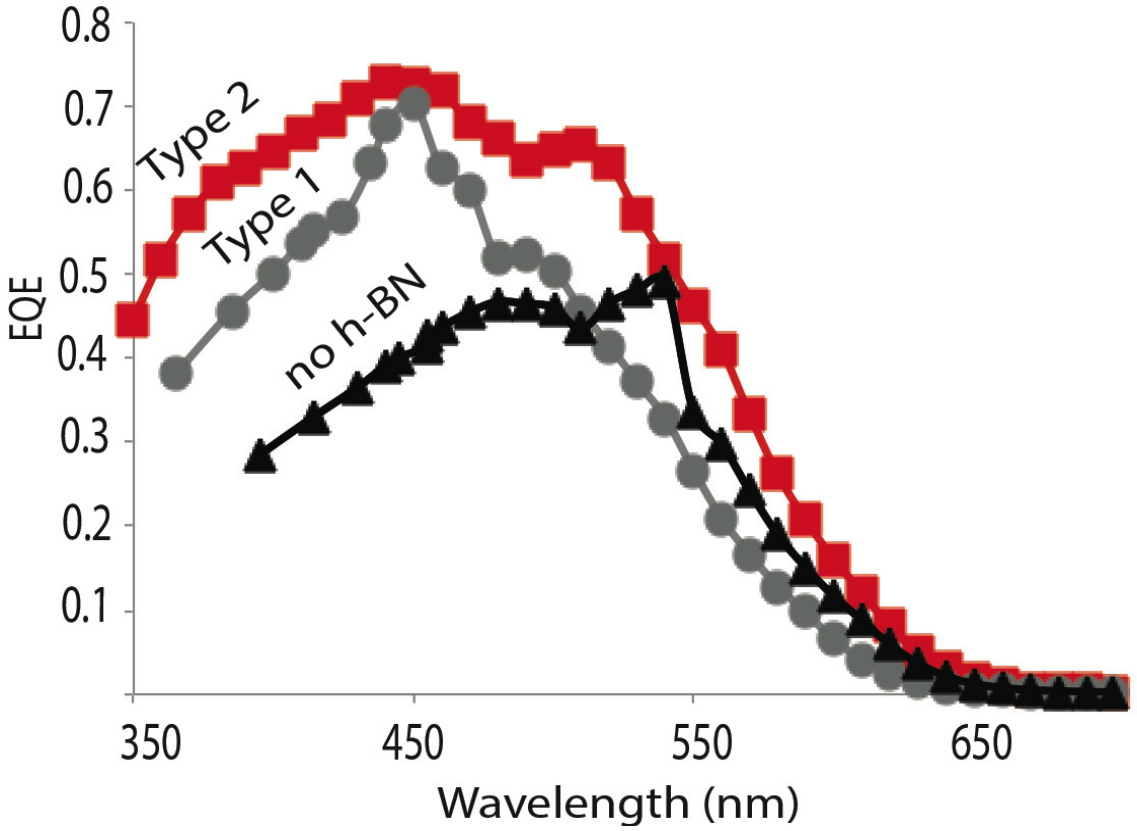

Figure B-S 7 External quantum efficiency (EQE) spectra of Type 1, Type 2 MIS Schottky solar cells, and Cu/Cu2O Schottky solar cell (no h-BN) is shown. The EQE measurements show improvement of incoming photon fraction contribution in the front and rear surfaces of the Type 2 device, while only improvement on the front surface was observed in the Type 1 device. These improvements are based on using the Cu/Cu2O Schottky solar cell (no h-BN) as the reference point.

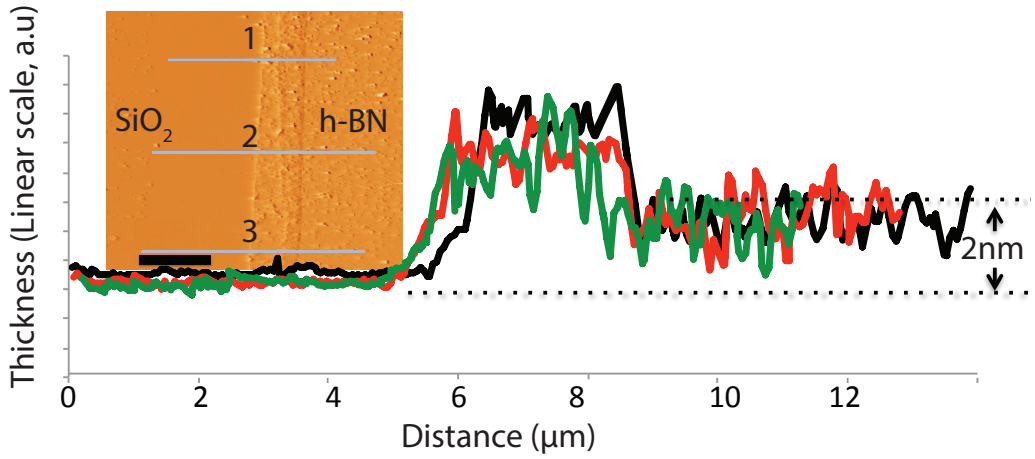

Figure B-S 8 AFM study of exfoliated h-BN layer which was transferred to a Si/SiO_2 substrate after Cu_2O etching. Different data sets from different line scans are shown marked as 1, 2, and 3(green, red, and black respectively), averaged over multiple lines. (Scale-bar: 4µm). h-BN folded at the edge resulting in an initial peak thickness but the AFM study confirms that h-BN thickness is around 1-2nm for the rest of the material.

Appendix C

Supplementary Information High-temperature explosion-resistant Li-ion battery cells

C.1 Supplementary Figures

Supporting Information Content

- Cyclic voltmmograms of Li-ion half cells
- Impedance Spectra of cells without filler
- Impedance Spectra of Li-ion cells with TiO_s
- Performance HTEC cells with TiO_2

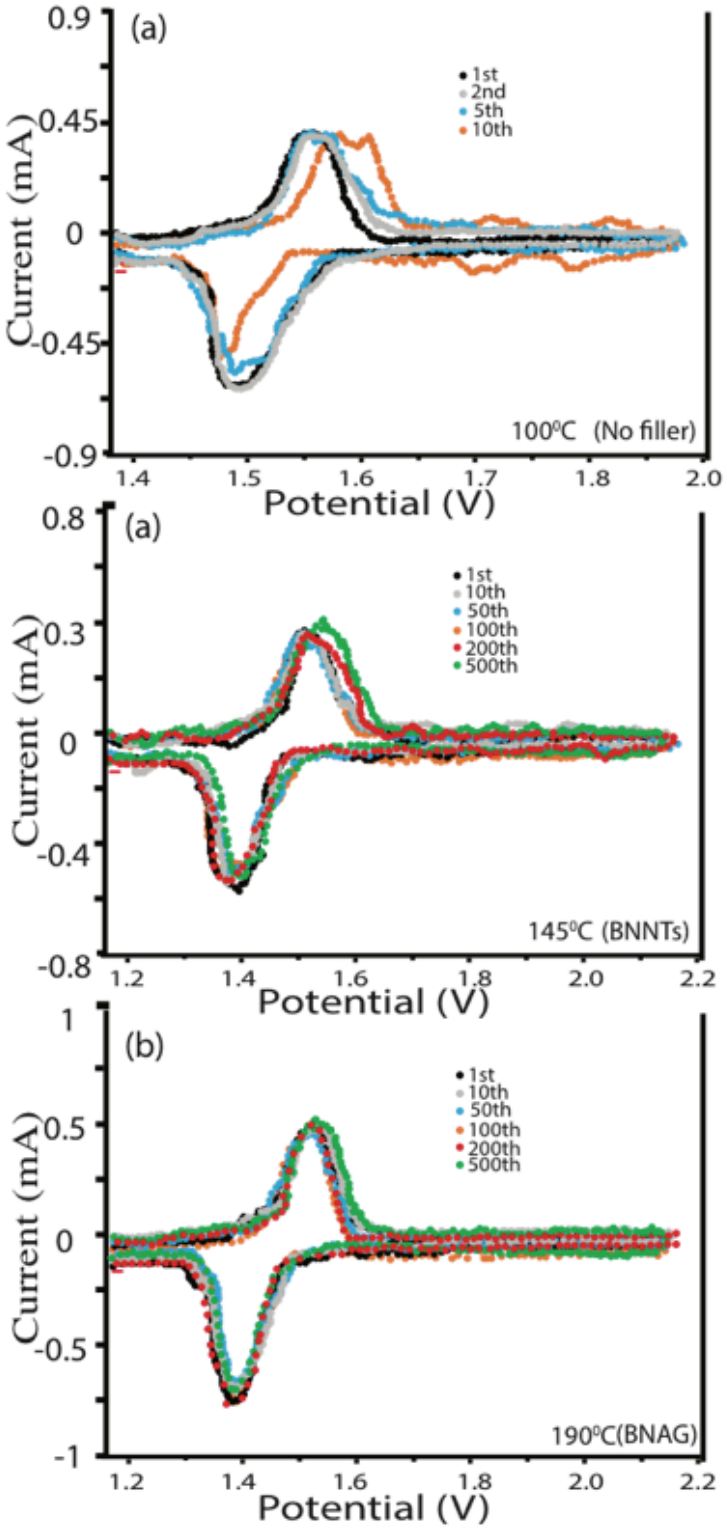

Figure C-S 1 Cyclic voltammograms of Li-ion half cells with $Li_4Ti_5O_{12}$ with scan rate $0.1mVs^{-1}$. The battery cells without filler suffer severe degradation after the 10^{th} cycle.

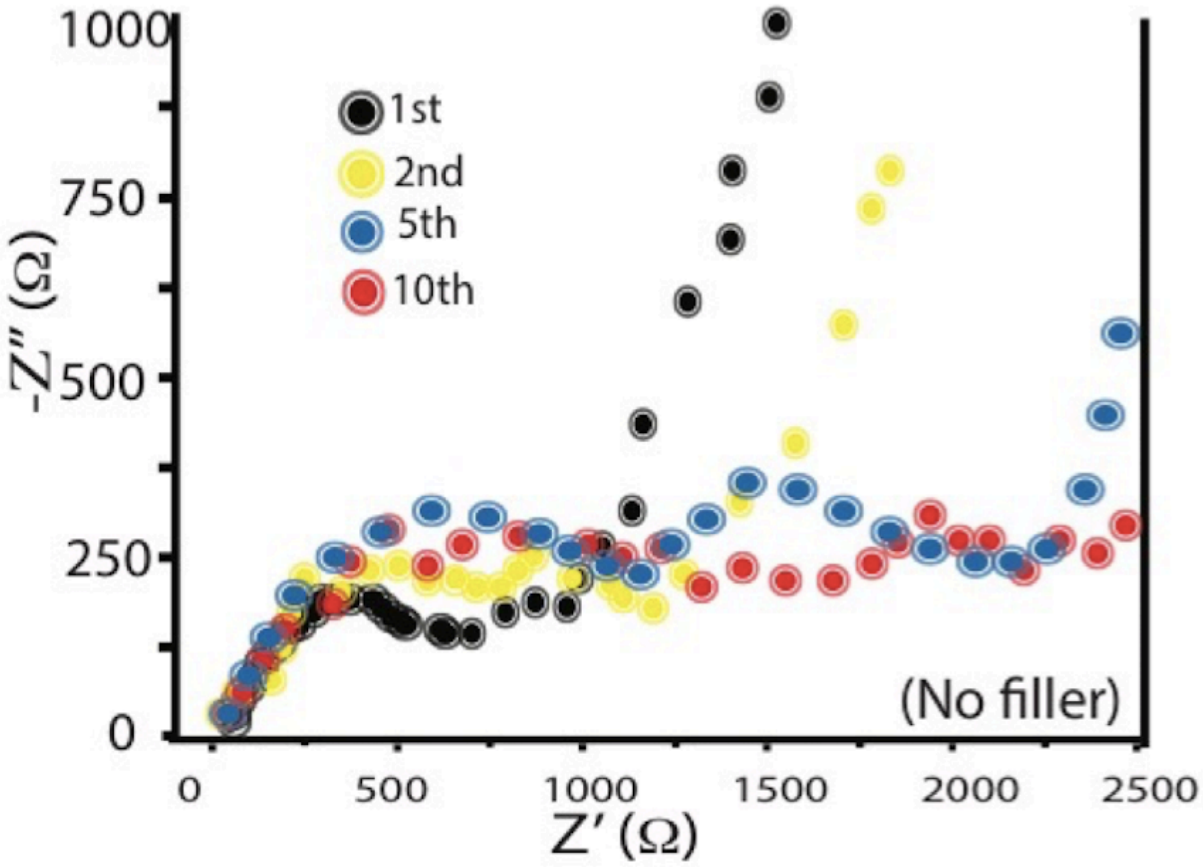

Figure C-S 2 Impedance spectra of the Li-ion cell without a filler.

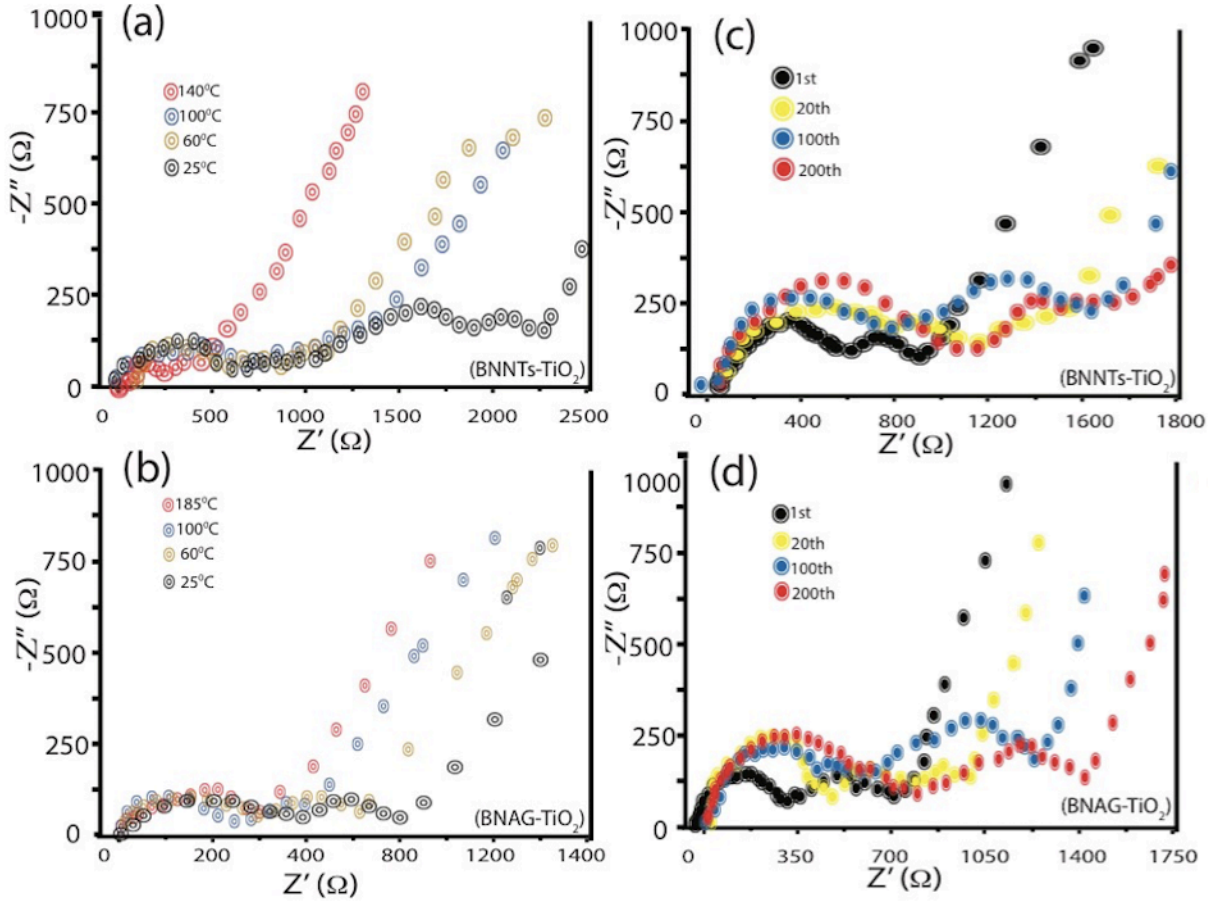

Figure C-S 3 Impedance spectra of the Li-ion cells with TiO2 nanoparticles.

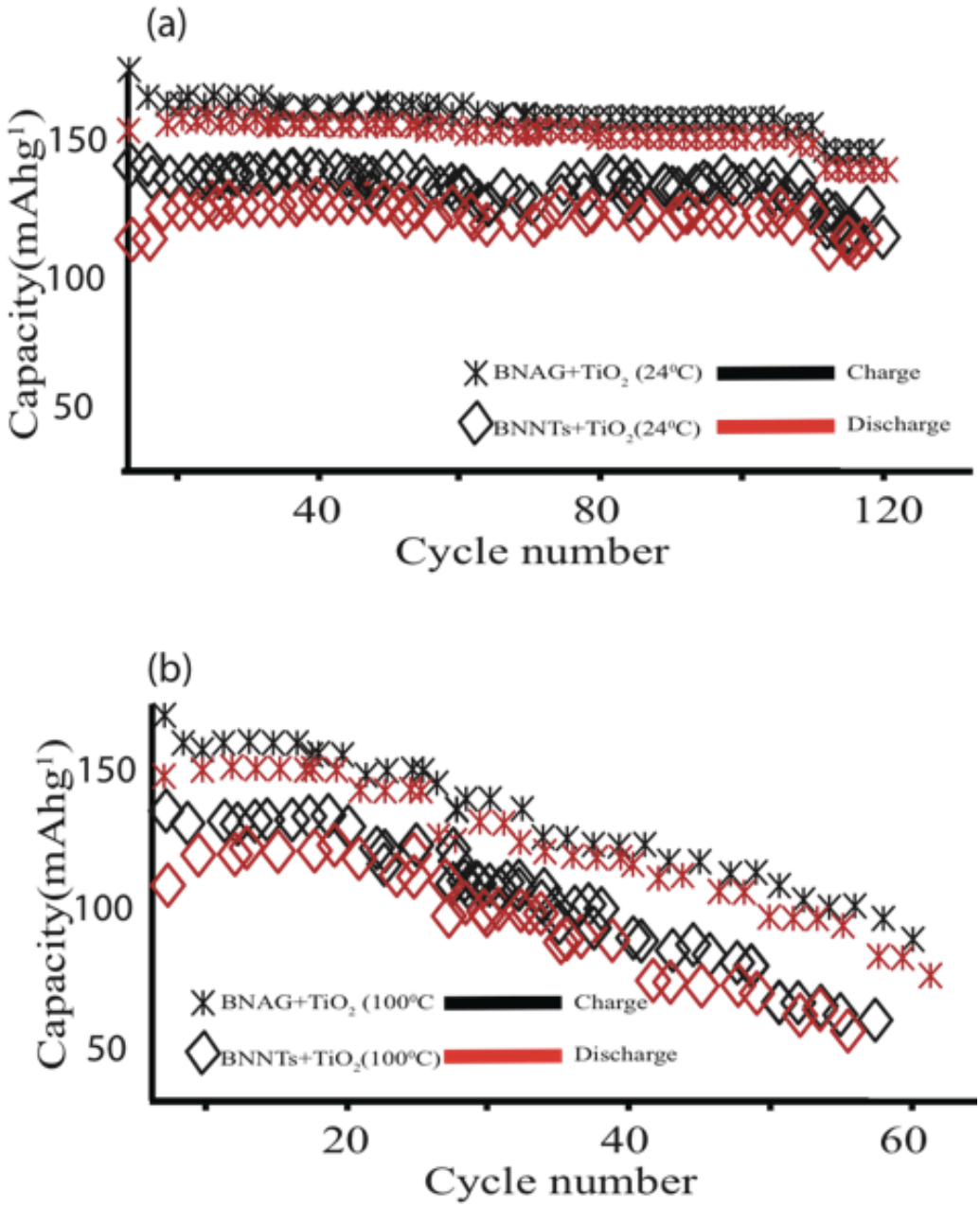

Figure C-S 4 Performance of HTEC cells with TiO_2 nanoparticles. The cells are studied at room temperature and 100^0C.